

# **Color Superconductivity: Phase Diagrams and Goldstone Bosons in the Color-Flavor Locked Phase**

Vom Fachbereich Physik  
der Technischen Universität Darmstadt

zur Erlangung des Grades  
eines Doktors der Naturwissenschaften  
(Dr. rer. nat.)

genehmigte Dissertation von  
Dipl.-Phys. Verena Kleinhaus  
aus Rüsselsheim

Darmstadt 2009  
D17

Referent: Priv. Doz. Dr. Michael Buballa  
Korreferent: Prof. Dr. Jochen Wambach  
Tag der Einreichung: 10.02.2009  
Tag der Prüfung: 29.04.2009

## Zusammenfassung

Die Untersuchung des Phasendiagramms stark-wechselwirkender Materie wird mit großem experimentellen und theoretischen Aufwand betrieben und ist eines der spannendsten Forschungsgebiete der modernen Teilchenphysik. Man geht davon aus, dass bei hohen Dichten und niedrigen Temperaturen farbsupraleitende Phasen auftreten, in denen sich Cooperpaare aus Quarks bilden. Aufgrund der hohen Temperaturen, die in Schwerionenkollisionen erreicht werden, scheint es nicht möglich, diesen Bereich experimentell zu untersuchen. Farbsupraleitung könnte jedoch im Inneren von Neutronensternen vorkommen. In der vorliegenden Arbeit untersuchen wir farbsupraleitende Phasen im Rahmen des Nambu–Jona-Lasinio-Modells.

Wir berechnen zunächst das Phasendiagramm für neutrale Materie im  $\beta$ -Gleichgewicht für zwei unterschiedliche Diquark-Kopplungsstärken. Wir bestimmen dazu die dynamischen Quarkmassen selbstkonsistent zusammen mit den Ordnungsparametern der Farbsupraleitung. Dabei beeinflussen die dynamisch erzeugten Massen die Phasenstruktur, die sich ihrerseits wieder auf die Massen auswirkt. So ergibt sich insbesondere für die kleinere Kopplungsstärke aufgrund des Wechselspiels von Neutralität und Quarkmassen eine interessante Phasenstruktur.

Im Anschluss berücksichtigen wir zusätzlich noch eine erhaltene Leptonenzahl, um die Situation in den ersten Sekunden eines Protoneutronensternes abzubilden, wenn die Neutrinos noch im Inneren „gefangen“ sind. Dies hat einen großen Einfluss auf die Phasenstruktur und bevorzugt deutlich die so genannte 2SC-Phase, in der es nur Paare von Up- und Downquarks gibt, und verschiebt die CFL-Phase, in der alle Quarks an der Bildung von Cooperpaaren beteiligt sind, zu sehr hohen Dichten.

In der zweiten Hälfte der Arbeit konzentrieren wir uns auf die CFL-Phase, die sich durch eine spezielle Symmetriebrechung auszeichnet. Die Brechung der chiralen Symmetrie führt zum Auftreten von acht pseudoskalaren Goldstonebosonen und die Brechung der  $U(1)_A$  Symmetrie resultiert in einem neunten. Die Eigenschaften dieser neun Goldstonebosonen werden untersucht, indem die Bethe-Salpeter-Gleichung für Quark-Quark-Streuung gelöst wird. Da die Goldstonebosonen die niedrigsten Anregungen in der CFL-Phase darstellen, sind sie von entscheidender Bedeutung für die thermodynamischen Eigenschaften des Systems.

Die Eigenschaften der Goldstonebosonen können auch von der Niederenergie Theorie der CFL-Phase beschrieben werden. Die entsprechenden Niederenergiekonstanten werden dabei im Grenzfall asymptotischer Dichten bestimmt, da die starke Wechselwirkung dort schwach ist (so genannte asymptotische Freiheit) und störungstheoretisch behandelt werden kann. Das Ziel unserer Rechnungen ist der Vergleich unserer Ergebnisse mit diesen Voraussagen, um so zum einen den schwach-gekoppelten Grenzfall unseres Modells zu testen, und zum anderen Aussagen über die Gültigkeit des schwach-gekoppelten Grenzfalls bei mittleren Dichten zu erlangen.

Wie erwartet sind die Goldstonebosonen im chiralen Limes masselos. Für endliche aber gleiche Quarkmassen steigen die Goldstonemassen linear mit der Quarkmasse.

Die acht Goldstonebosonen der chiralen Symmetriebrechung bleiben dabei entartet, während das neunte ein wenig schwerer ist. Für ungleiche Quarkmassen (gleiche Masse für Up- und Downquarks aber höhere Strangequarkmasse) sind die Goldstonebosonen der chiralen Symmetriebrechung nicht mehr entartet, sondern zeigen eine inverse Massenanordnung, bei der die Kaonen leichter sind als die Pionen. Sowohl für gleiche als auch für ungleiche Quarkmassen stimmen die Ergebnisse der Modellrechnungen qualitativ mit den Vorhersagen der Niederenergietheorie überein. Allerdings gibt es quantitative Unterschiede zum schwach-gekoppelten Grenzfall.

Des Weiteren berechnen wir die Zerfallskonstanten der Goldstonebosonen. Unsere Ergebnisse reproduzieren den Grenzfall schwacher Kopplung, zeigen aber wieder deutliche Abweichungen für stärkere Kopplungen.

# Contents

<b>1</b>	<b>Introduction</b>	<b>1</b>
<b>2</b>	<b>Color superconductivity</b>	<b>7</b>
2.1	Concept . . . . .	7
2.2	Symmetries . . . . .	9
2.3	Color-superconducting phases . . . . .	10
2.3.1	Two-flavor color superconductivity . . . . .	10
2.3.2	Color-flavor locked phase . . . . .	11
2.3.3	Further color-superconducting scenarios . . . . .	13
<b>3</b>	<b>Nambu–Jona-Lasinio model</b>	<b>17</b>
3.1	Lagrangian . . . . .	17
3.2	Thermodynamic potential . . . . .	19
3.3	Gap equations and neutrality conditions . . . . .	23
<b>4</b>	<b>Phase diagrams of neutral quark matter</b>	<b>27</b>
4.1	Intermediate coupling . . . . .	27
4.2	Strong coupling . . . . .	33
<b>5</b>	<b>The effect of neutrino trapping</b>	<b>37</b>
5.1	Neutrino trapping . . . . .	37
5.2	Influence on the phase structure . . . . .	38
5.2.1	$T$ - $\mu$ phase diagrams . . . . .	39
5.2.2	$T$ - $\mu_{L_e}$ phase diagrams . . . . .	44
5.2.3	Lepton fraction . . . . .	49
<b>6</b>	<b>Pseudoscalar bosons in the color-flavor locked phase</b>	<b>51</b>
6.1	Summary of effective theory results . . . . .	52
6.2	Nambu–Jona-Lasinio model . . . . .	54
6.2.1	Lagrangian . . . . .	54
6.2.2	Ground state . . . . .	55
6.3	Mesonic excitations . . . . .	59
6.3.1	Axial transformations . . . . .	59
6.3.2	Bethe-Salpeter equation . . . . .	60
6.4	Masses of the Goldstone bosons . . . . .	64

---

6.4.1	Equal quark masses . . . . .	64
6.4.2	Unequal quark masses . . . . .	66
6.5	Masses of the higher-lying excitations . . . . .	71
6.5.1	Equal quark masses . . . . .	71
6.5.2	Unequal quark masses . . . . .	73
<b>7</b>	<b>Meson decay constants</b>	<b>77</b>
7.1	Derivation of the meson decay constants . . . . .	77
7.1.1	Numerical calculation of the decay constant . . . . .	78
7.1.2	Semianalytical derivation of the pion decay constant in the chiral limit . . . . .	79
7.2	Decay constants in the chiral limit . . . . .	84
7.2.1	Goldstone bosons . . . . .	84
7.2.2	Higher-lying excitations . . . . .	86
7.3	Low-energy constant $A$ . . . . .	87
<b>8</b>	<b>Summary</b>	<b>91</b>
<b>A</b>	<b>Conventions</b>	<b>95</b>
<b>B</b>	<b>Dressed quark propagator</b>	<b>97</b>
B.1	Diagonalization of the (inverse) dressed propagator . . . . .	97
B.2	Dressed propagator for equal quark masses . . . . .	98
<b>C</b>	<b>Numerical calculation of some loops</b>	<b>99</b>
C.1	Polarization function or similar loop . . . . .	99
C.2	Derivative of the polarization function . . . . .	101

# 1 Introduction

People have always been curious about the nature of matter. Already around 400 B.C. Democritus formulated the idea of atoms (greek: atomos = uncuttable) as the smallest indivisible constituents of matter. At that time, it competed with the idea of matter consisting of the four elements fire, air, water, and earth. It took over two thousand years until Democritus' idea got revived by John Dalton in 1803 who used the concept of atoms to explain why elements always react in ratios of small integer numbers. He proposed that different types of atoms exist and that each element consists of atoms of one single type. The notion of the atoms as the smallest units of matter was dropped in 1903 with Joseph J. Thomson's plum pudding model of the atom, in which electrons are surrounded by a soup of positive charge. Already eight years later Rutherford proved the existence of the small positively charged atomic nucleus. Today, we know that the nucleus consists of nucleons, i.e., protons and neutrons, which have a substructure of quarks and gluons of their own.

Quarks have been proposed independently by Murray Gell-Mann [1] and George Zweig<sup>1</sup> [2] in 1964. Today we know six types (called flavors) of quarks: up, down, strange, charm, bottom, and top. They are subject to the strong interaction which is described by the theory of quantum chromodynamics (QCD). This name reflects the fact that each quark carries one of three color charges, red, green, and blue. These three colors together add up to a colorless state. The strong interaction between quarks is mediated by gluons which carry color charges themselves and can therefore interact with other gluons as well.

QCD has three prominent features: confinement, asymptotic freedom, and spontaneous chiral symmetry breaking. The first two are connected to the strength of the strong interaction. Confinement describes the absence of free quarks and gluons in the physical spectrum, or in other words, the non-existence of free colored objects. Quarks are confined in hadrons, i.e., baryons and mesons. Baryons consist of three quarks with different color charges and are therefore color neutral. The best-known baryons are the proton and the neutron. Mesons, on the other hand, are built of one quark and one antiquark which carries the corresponding anticolor.

Asymptotic freedom means that the strong interaction becomes weak at small distances, i.e., the coupling constant of the strong interaction decreases with increasing momentum ("running coupling"). The smallness of the strong coupling constant for high momenta ( $\alpha_s \ll 1$ ) is very important for theoretical purposes, since it allows a

---

<sup>1</sup>Zweig originally called these particles "aces".

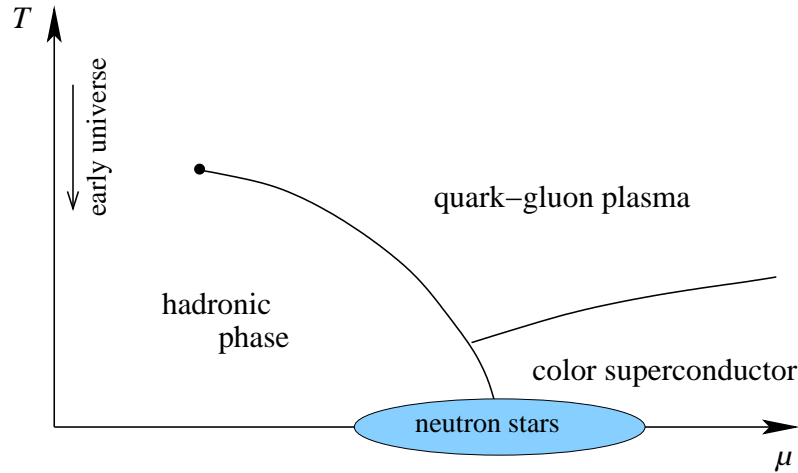


Figure 1.1: Schematic QCD phase diagram.

perturbative treatment. David J. Gross, H. David Politzer, and Frank Wilczek have been awarded the 2004 nobel prize for the discovery of asymptotic freedom [3, 4].

The third important feature of QCD is spontaneous chiral symmetry breaking. Chiral symmetry states that left- and right-handed quarks transform independently. It is an exact symmetry of QCD in the chiral limit, i. e., for massless quarks. In reality, chiral symmetry is broken explicitly by the finite quark masses, but for the light quarks it still has merit as an approximate symmetry. Chiral symmetry is spontaneously broken in the QCD vacuum by a condensate of left-handed quarks and right-handed antiquarks and vice versa.<sup>2</sup>

It is not only interesting what the constituents of matter are, but also how matter is built up of these constituents and how this depends on the external conditions. Usually, this is depicted in a phase diagram. A schematic picture of the QCD phase diagram is shown in Fig. 1.1. The phase diagram is spanned by temperature  $T$  and (baryon or quark) chemical potential  $\mu$  which is related to the density.

The region of moderate densities and temperatures is governed by the hadronic phase where quarks and gluons are confined in hadrons, and chiral symmetry is spontaneously broken. Already in 1975 it was proposed that matter is deconfined for high temperatures and densities [6, 7], meaning that hadrons overlap and lose their individuality. This so called quark-gluon plasma (QGP) is of cosmological interest because matter was certainly created in the QGP phase at very high temperatures after the big bang. Microseconds later, matter had cooled sufficiently to form hadrons and thus must have undergone a phase transition.

The systematics of the deconfinement transition from hadronic matter to the quark-

<sup>2</sup>Yoichiro Nambu [5] received the 2008 nobel prize “for the discovery of the mechanism of spontaneous broken symmetry in subatomic physics”.



---

gluon plasma is the subject of huge experimental and theoretical effort. For vanishing chemical potential there is presumably no real transition (in the thermodynamic sense) between the hadronic phase and the QGP, but only a smooth crossover. Theoretically, this region is accessible by calculations in which the QCD Lagrangian is formulated on a discrete space-time lattice. These calculations are very involved and need a lot of computing power. Moreover, most calculations are performed with unphysically high quark masses and, at present, the extension to finite chemical potentials poses a lot of problems. Whether this transition is connected to the chiral phase transition is not yet certain. For small chemical potentials and high temperature the transition to the QGP is probed by heavy-ion experiments. These are, for example, RHIC at BNL and SPS and LHC at CERN. The future FAIR facility in Darmstadt will examine this phase transition for higher chemical potentials. Hopefully, it will then be possible to discern whether the transition is of first order for larger chemical potentials and ends in a critical end-point, which is currently under debate [8].

Another interesting region of the phase diagram is situated at small temperatures and high chemical potentials. Already in 1975 the possibility of color superconductivity at very high densities was suggested [6]. In a color superconductor, Cooper pairs of quarks are formed in analogy to the Cooper pairs of electrons in ordinary metallic superconductors. The description of color superconductivity will be the topic of this thesis.

Besides the mere theoretical interest in color superconductivity, the phenomenon could be important for the physics of compact stars. In terms of the nuclear saturation density  $\rho_0 \approx 0.17 \text{ fm}^{-3}$ , the density inside the cores of neutron stars could reach up to  $10\rho_0$ , corresponding to chemical potentials around 500 MeV. At these densities color superconductivity might occur. It is very unlikely that color superconductivity can be accessed in heavy-ion experiments, since they probe matter at much larger temperatures and much smaller chemical potentials. Furthermore, large chemical potentials are not accessible to lattice calculations.

If one wants to describe matter in the central region of a star, one is naturally confronted with constraints on the properties of such matter. To form a stable neutron star, matter has to be neutral with respect to electrical and color charges and it has to be in weak equilibrium, i. e.,  $\beta$  equilibrium. Of course these conditions affect the phase structure. The scale of 500 MeV for the quark chemical potential justifies a restriction to the three lightest quark flavors, up, down, and strange. The three remaining flavors have masses larger than 1 GeV and do not have to be taken into account.

Due to asymptotic freedom, it is possible to treat the limiting case of asymptotically high densities perturbatively in the weak-coupling limit. However, this is not possible for the “moderate densities” relevant for compact star physics which are orders of magnitude too small to be treated in the weak-coupling limit. The strong coupling constant is of order 1 for the considered densities, prohibiting an expansion in orders of the coupling. In this strongly coupled regime one mainly uses effective models which capture the most important features of QCD, leaving others aside. One of

these models is the Nambu–Jona-Lasinio (NJL) model which is often used to describe color superconductivity. While model calculations suffer from the drawback that the model parameters are largely undetermined and are usually adjusted to reproduce vacuum values, they provide the opportunity to tackle complex problems which are not accessible via other approaches.

The strange quark plays a special role at moderate densities because its mass, while being smaller than the chemical potential, is considerably larger than the masses of up and down quarks. The strange quark mass lies somewhere between its vacuum constituent mass of more than 500 MeV and its current quark mass of around 100 MeV. The first attempt to study the phase diagram of dense, locally neutral, three-flavor quark matter as a function of the strange quark mass, the quark chemical potential, and the temperature was made in Ref. [9], where the effect of the strange quark mass has been incorporated only approximately through a shift in the strange quark chemical potential. The phase diagram was further developed in Refs. [10, 11] where the strange quark mass has been taken into account properly, but still has been treated as a free parameter. In contrast to these approaches, we will only treat the bare quark masses as parameters and derive the constituent quark masses dynamically for all three quark flavors together with the order parameters of color superconductivity in a Nambu–Jona-Lasinio type model.

One of the phases encountered in the phase diagram is the color-flavor locked (CFL) phase in which all quark species (up, down, and strange quarks of all three colors) participate in the diquark pairing in a particularly symmetric way [12]. The most interesting property of the CFL phase is its special symmetry breaking pattern which leads to the emergence of Goldstone bosons. For explicitly broken chiral symmetry due to finite quark masses, the Goldstone bosons acquire a mass.<sup>3</sup> The Goldstone bosons are the lowest lying excitations in the CFL phase and therefore play an important role for the thermodynamics [13, 14]. On the basis of the symmetry-breaking pattern a low-energy effective theory (LEET) has been constructed for the CFL phase which describes the Goldstone boson dynamics for energies much smaller than the superconducting gap. At very high densities, the interaction is weak, and masses and decay constants of the Goldstone bosons have been calculated in the weak-coupling limit. Furthermore, it was shown that the stress imposed by a massive strange quark could lead to kaon condensation. At moderate densities the weak-coupling assumption is not justified. However, the leading order predictions do not depend on the details of the interaction and should hold in any model exhibiting the same symmetry-breaking pattern. The NJL model possesses the required symmetry-breaking pattern and has already been applied to study kaon condensation in the CFL phase at nonzero strange quark mass, but without explicitly constructing the Goldstone bosons [15, 16, 17]. The properties of the Goldstone bosons have only been studied by explicit construc-

---

<sup>3</sup>Strictly speaking they should be called pseudo Goldstone bosons then. For simplicity, we will just call them Goldstone bosons throughout this work also for explicitly broken chiral symmetry.

---

tion in the chiral limit [18, 19]. In this thesis we will present a detailed analysis of the properties of the Goldstone bosons for finite quark masses, including a heavier strange quark. We will compare our results with the leading-order LEET predictions. This comparison might provide an indication of the range of validity of the LEET results derived in the weak-coupling limit.

This thesis is organized as follows: In Chapter 2 we will introduce the concept of color superconductivity and briefly describe the main phases and possible theoretical approaches to the subject. Afterwards, the NJL model and its application to color superconductivity are described in Chapter 3. In Chapter 4 we present phase diagrams and properties (masses, gap parameters, and charge chemical potentials) for neutral quark matter with self-consistently derived quark masses. These results have been published in [20]. Subsequently, we will include neutrinos and lepton number conservation into our analysis in Chapter 5. This is necessary to calculate phase diagrams under the conditions for proto-neutron stars where neutrinos are trapped for the first few seconds of the stellar evolution. The results of Chapter 5 have been published in [21].

We will then leave the topic of phase diagrams and consider the properties of bosons in the CFL phase for the remainder of this work. In Chapter 6 we will present the extensions that are needed to calculate the properties of the bosonic excitations in the CFL phase and discuss the numerical results for the masses of the Goldstone bosons as well as for the higher-lying excitations. The decay constants will then be presented in Chapter 7. The results of these two chapters have been published in [22, 23]. We will conclude with a summary and an outlook in Chapter 8.



## 2 Color superconductivity

After the first suggestion of color superconductivity in 1975 [6] only little attention had been paid to the subject and its relevance for the phase diagram of strongly interacting quark matter [24, 25, 26]. This attitude changed at the end of the 1990s when gaps of the order of 100 MeV in the fermionic spectrum were found in model calculations for chemical potentials of around 500 MeV [27, 28]. In standard weak-coupling BCS theory, the critical temperature for superconductivity  $T_c$  is connected to the zero temperature gap  $\Delta_0$  via  $T_c \approx 0.57\Delta_0$  [29] and therefore gaps of this size extend the region of color superconductivity widely in temperature direction, up to temperatures around 50 MeV.

We start our work with a description of the concept of color superconductivity and the two most prominent phases, followed by a short overview of possible theoretical approaches to the subject. Additional details can be found in the review literature on the subject, e. g. [30, 31, 32, 33, 34, 35].

### 2.1 Concept

At sufficiently low temperatures, any system of fermions with an arbitrarily weak attractive interaction develops a Cooper instability. At  $T = 0$ , the fermions fill all states up to the Fermi momentum  $p_F$ . At the highly degenerate Fermi surface the creation of a pair of fermions costs no free energy, hence any present attraction would lead to a gain in free energy via pairing, causing an instability of the Fermi surface. The formation of these Cooper pairs leads to a new ground state with a non-zero energy gap  $\Delta$  in the quasiparticle spectrum  $\omega_p$ , typically

$$\omega_p = \sqrt{(E_p - \mu)^2 + \Delta^2}, \quad (2.1)$$

where  $\mu$  is the chemical potential and  $E_p = \sqrt{m^2 + \vec{p}^2}$  is the energy of a free fermion with mass  $m$  and momentum  $\vec{p}$ .

For conventional metallic superconductors the Bardeen-Cooper-Schrieffer (BCS) theory [36] describes the formation of Cooper pairs consisting of electrons with opposite momenta and spin. In the case of QCD, the Cooper pairs are made up of two quarks, and since any formation of two quarks is colored, the phenomenon is referred to as *color* superconductivity. In contrast to electrons which feel the repulsive Coulomb interaction, the interaction between quarks of different color is attractive.

In this sense the mechanism of color superconductivity is more direct than that of conventional superconductivity where the repulsion between two electrons has to be overcome by an attraction provided by the interaction between electrons and lattice vibrations of the conducting solid. On the other hand, the situation is more involved because quarks carry the additional quantum numbers of color and flavor which allows for different pairing scenarios.

A diquark condensate is defined as the expectation value

$$\langle q^T \mathcal{O} q \rangle \quad (2.2)$$

where the quark field  $q$  carries spin, flavor, and color degrees of freedom. Therefore, the operator  $\mathcal{O}$  acts in Dirac, flavor, and color space

$$\mathcal{O} = \mathcal{O}_{\text{Dirac}} \otimes \mathcal{O}_{\text{flavor}} \otimes \mathcal{O}_{\text{color}} . \quad (2.3)$$

Due to the Pauli principle, the condensate has to be antisymmetric under the exchange of the two quarks. This can be achieved by an operator which is antisymmetric in all three spaces or antisymmetric in one space and symmetric in the two others. The symmetry properties of the operators in Dirac, color, and flavor space are summarized in Tab. 2.1.

space	antisymmetric operators	symmetric operators
Dirac	$C\gamma_5, C, C\gamma^\mu\gamma_5$	$C\gamma^\mu, C\sigma^{\mu\nu}$
color, flavor (three-flavor case)	$\lambda_2, \lambda_5, \lambda_7$	$\mathbb{1}, \lambda_1, \lambda_3, \lambda_4, \lambda_6, \lambda_8$
flavor (two-flavor case)	$\tau_2$	$\mathbb{1}, \tau_1, \tau_3$

Table 2.1: Symmetries under transposition for operators in Dirac, color, and flavor space.  $\tau_i$  denote the Pauli matrices,  $\lambda_i$  the Gell-Mann matrices, and  $C = i\gamma^2\gamma^0$  is the charge conjugation matrix.

The Pauli principle alone is not sufficient to determine the pairing pattern. The structure of the condensate depends on the details of the interaction. At very large densities quark matter is weakly interacting. In this region the one-gluon exchange is the dominant interaction between quarks. It is attractive in the antisymmetric color antitriplet channel and repulsive in the symmetric sextet channel. The instanton induced interactions that are likely to play a role at moderate densities are attractive in the color antitriplet channel as well. The color antitriplet channel corresponds to the operators  $\lambda_2, \lambda_5$ , and  $\lambda_7$  in color space (see Tab. 2.1).

## 2.2 Symmetries

When talking about color superconductivity, one has to take into account the symmetries of QCD. In Table 2.2 these are summarized together with the corresponding symmetry transformations.

symmetry	transformation	corresponds to
$SU(N_f)_V$	$q \rightarrow \exp[i\theta_a^V \tau_a/2] q$	vector flavor symmetry, isospin symmetry ( $N_f = 2$ )
$SU(N_f)_A$	$q \rightarrow \exp[i\theta_a^A \gamma_5 \tau_a/2] q$	axial flavor symmetry
$U(1)_V$	$q \rightarrow \exp[i\alpha] q$	baryon number conservation
$U(1)_A$	$q \rightarrow \exp[i\phi \gamma_5] q$	the breaking of $U(1)_A$ is known as the axial anomaly
$SU(3)_c$	$q \rightarrow \exp[i\eta_a(x) \lambda_a/2] q$	color gauge symmetry

Table 2.2: Symmetries of QCD.  $\tau_a/2$  are the generators of flavor  $SU(N_f)$  and  $\lambda_a$  are the Gell-Mann matrices in color space.

One prominent feature of QCD is its spontaneous chiral symmetry breaking. Chiral symmetry manifests itself in the invariance of the QCD Lagrangian under independent transformations of left- and right-handed quarks and is described by the group  $U(N_f)_L \times U(N_f)_R$ . This is equivalent to invariance under  $SU(N_f)_V \times SU(N_f)_A \times U(1)_V \times U(1)_A$  transformations (see Tab. 2.2). For the  $SU(N_f)_V$  symmetry it is sufficient to have  $N_f$  degenerate quark masses, whereas the  $SU(N_f)_A$  chiral symmetry requires  $N_f$  massless quarks. This implies that chiral symmetry is only exact in the chiral limit, but it is still a useful approximate symmetry for small quark masses. While chiral symmetry is a symmetry of the QCD Lagrangian, it is spontaneously broken in the vacuum ground state by a condensate of left-handed quarks and right-handed antiquarks and vice versa. The Goldstone theorem [37] states that the theory must then contain one massless particle for each generator of the spontaneously broken continuous symmetry. As chiral symmetry is explicitly broken by finite quark masses, one expects light rather than massless Goldstone bosons. In two-flavor QCD these are the three pions, and for three-flavor QCD it is the pseudoscalar octet consisting of  $\pi^+$ ,  $\pi^-$ ,  $\pi^0$ ,  $K^+$ ,  $K^-$ ,  $K^0$ ,  $\bar{K}^0$ , and  $\eta$ .

The symmetry corresponding to baryon number conservation is  $U(1)_V$ . This symmetry is also valid for massive quarks.

The  $U(1)_A$  symmetry is special. It is a symmetry of the classical QCD Lagrangian for massless quarks, but it is broken anomalously on the quantum level by instantons.

In nature, this is reflected by the relatively heavy  $\eta'$  which should otherwise be a light Goldstone boson.

Apart from these global symmetries, QCD exhibits the local  $SU(3)_c$  gauge symmetry. While this is a good symmetry in the QCD vacuum, it is broken in the color superconducting phases. Breaking the color gauge symmetry gives masses to the gluons through the Anderson-Higgs mechanism [38, 39].

## 2.3 Color-superconducting phases

In contrast to electrons which carry electric charge only, quarks carry color charges as well and come in different flavors. This opens room for various pairing scenarios.

We will be interested in physics for quark chemical potentials not much larger than 500 MeV, which is realistic for the situation inside the core of a neutron star. Therefore, it is reasonable to include only the three lightest quark flavors (up, down, and strange) into our considerations. The three other flavors are too heavy to play a role: the charm quark, as the lightest of them, has a mass larger than 1 GeV.

The two most famous and most discussed color superconducting phases are the two-flavor color superconductor (2SC) and the color-flavor locked (CFL) phase. These are two opposite limiting cases. In the 2SC phase only the two light quark flavors participate in the pairing. The strange quark is taken as infinitely heavy and is therefore not present. The CFL phase, on the other hand, arises from a scenario involving three light quark flavors.

Of course, the real world lies between the extremes of an infinitely heavy and a massless strange quark. It is exactly this complexity arising through the interplay of a middle-weight strange quark with the neutrality conditions necessary to describe realistic scenarios, which will be the subject of our calculations of the phase diagrams in Chapter 4.

### 2.3.1 Two-flavor color superconductivity

We begin with the description of the two-flavor color superconductor because it is the simplest color superconducting phase. The 2SC phase occurs for the up and down quark mass being much smaller than the strange quark mass. For simplicity the considerations are performed for a two-flavor system consisting of degenerate up and down quarks only.

In the two-flavor case a scalar spin-0 condensate is of the form

$$s_{2A} = \langle q^T C \gamma_5 \tau_2 \lambda_A q \rangle, \quad A = 2, 5, 7 \quad (2.4)$$

with the antisymmetric Gell-Mann matrices  $\lambda_A$  acting in color space and the antisymmetric Pauli matrix  $\tau_2$  acting in flavor space.  $C = i\gamma^2\gamma^0$  is the charge conjugation matrix. This condensate is totally antisymmetric (see Tab. 2.1). In principle, Eq. (2.4)



describes three condensates which form a vector in color space. This vector can be rotated into the  $A' = 2$ -direction by a global  $SU(3)$ -color transformation without loss of generality. This leads to the 2SC condensate

$$s_{22} = \langle q^T C \gamma_5 \tau_2 \lambda_2 q \rangle . \quad (2.5)$$

Using red, green, and blue for the order of the colors, Eq. (2.5) describes the formation of condensates of red and green up and down quarks:  $(u_r, d_g)$ ,  $(u_g, d_r)$ . The blue up and down quarks do not participate in the pairing. As a consequence, they give rise to gapless quasiparticles in the low-energy excitation spectrum. These have important phenomenological consequences for the physics of compact stars. The gapless quasiparticles contribute to the specific heat and to the electrical and heat conductivities, and also lead to a large neutrino emissivity through the  $\beta$  processes  $d_b \rightarrow u_b + e^- + \bar{\nu}_e$  and  $u_b + e^- \rightarrow d_b + \nu_e$  [40].

Since the blue quarks do not appear in the condensate, color  $SU(3)_c$  symmetry is broken down to  $SU(2)_c$ . This implies that five gluons (eight generators of  $SU(3)_c$  minus three remaining generators of the unbroken  $SU(2)$  subgroup) acquire a mass through the Anderson-Higgs mechanism. At first sight, one could expect that the non-vanishing charge of the condensate leads to a breaking of the electromagnetic  $U(1)_{em}$  symmetry as well. However, it is possible to identify a modified charge  $\tilde{Q}$  which is a linear combination of electric and color charge with a corresponding unbroken  $\tilde{U}(1)_{em}$ . The same is possible for the baryon number, see e.g. [30, 34, 33] for details on these modified symmetries. In addition, the condensate  $s_{22}$  preserves the  $SU(2)_L \times SU(2)_R$  chiral symmetry if up and down quarks are massless, hence, no Goldstone bosons emerge in the 2SC phase.

The 2SC phase can also exist in a three-flavor scenario with a heavy strange quark. For this purpose one only has to replace the Pauli matrix  $\tau_2$  in Eq. (2.5) by the Gell-Mann matrix  $\lambda_2$  in three-dimensional flavor space, which only connects the first two flavors.

### 2.3.2 Color-flavor locked phase

The color-flavor locked phase is the ground state of quark matter at asymptotically high densities. In this introductory section, the CFL phase is considered in the chiral limit of three-flavor quark matter.

The CFL phase is characterized by the scalar diquark condensates

$$s_{AA} = \langle q^T C \gamma_5 \tau_A \lambda_A q \rangle , \quad A = 2, 5, 7 \quad (2.6)$$

with  $\tau_A$  and  $\lambda_A$  denoting the antisymmetric Gell-Mann matrices acting in flavor space and color space, respectively. We will always use  $\lambda_i$  for matrices acting in color space and  $\tau_i$  for matrices acting in flavor space, irrespective of whether these matrices are Pauli matrices (for two-flavor quark matter) or Gell-Mann matrices (for three-flavor

quark matter). The ideal CFL phase with three degenerate quark flavors is further characterized by

$$s_{22} = s_{55} = s_{77}. \quad (2.7)$$

Eq. (2.6) can be seen as a generalization of the 2SC pairing pattern to the three-flavor case. In the CFL phase all nine quarks participate in the pairing and the following pairs are present:  $(u_r, d_g)$ ,  $(u_g, d_r)$ ,  $(u_r, s_b)$ ,  $(u_b, s_r)$ ,  $(d_g, s_b)$ ,  $(d_b, s_g)$ .

The most noticeable feature of the CFL phase is its special symmetry breaking pattern: while it is neither invariant under color transformations nor flavor transformations alone, the condensate is invariant under the combined color and flavor rotations

$$q \rightarrow \exp \left[ i\theta_a \frac{\tau_a - \lambda_a^T}{2} \right] q, \quad a = 1, \dots, 8. \quad (2.8)$$

This ‘‘locking’’ of color and flavor gave the phase its name. The locking of two properties is not a new phenomenon. Spontaneous chiral symmetry breaking in the QCD vacuum is based on the locking of two previously unrelated symmetries as well. In that case the  $SU(N_f)_L$  and  $SU(N_f)_R$  transformations of left and right-handed quarks are locked to  $SU(N_f)_{L+R} = SU(N_f)_V$ .

Just as for 2SC, there exists a modified  $\tilde{Q}$  charge with unbroken  $\tilde{U}(1)_{em}$ , but in contrast to the 2SC case, it is not possible to construct a modified conserved baryon number  $\tilde{B}$ . In the CFL phase the baryon number symmetry  $U(1)_V$  is broken down to  $Z_2$  [33, 12].

In summary the symmetry breaking pattern in the CFL phase reads

$$SU(3)_c \times SU(3)_L \times SU(3)_R \times U(1)_V \longrightarrow SU(3)_{c+L+R} \times Z_2. \quad (2.9)$$

Due to the breaking of color symmetry all eight gluons acquire a mass, whereas chiral symmetry breaking results in a pseudoscalar octet of Goldstone bosons. The breaking of baryon number symmetry leads to a scalar Goldstone boson [12].

We should stress that the mechanism of chiral symmetry breaking in the CFL phase is different from chiral symmetry breaking in the QCD vacuum. In vacuum, chiral symmetry is broken by a condensate of left-handed quarks with right-handed antiquarks and vice versa, which directly locks  $SU(N_f)_L$  and  $SU(N_f)_R$ . In the CFL phase, however, the diquark condensates consist of two left-handed or two right-handed quarks only.  $SU(3)_L$  and  $SU(3)_R$  are only indirectly connected by locking each separately to  $SU(3)_c$ .

In contrast to the 2SC phase, all quark species participate in the pairing and no gapless quasiparticles appear in the low-energy fermionic excitation spectrum. The lowest-lying excitations are then the Goldstone bosons originating from the symmetry-breaking [13].

For completeness, it should be added that the CFL condensates  $s_{AA}$  which are formed by combining a color antitriplet with a flavor antitriplet, are accompanied by color sextet, flavor sextet condensates (see Sec. 2.1). There is always a small

admixture of these symmetric condensates [12, 41]. Since it has been shown that the sextet condensates are small compared to the antitriplet ones [42, 43], we will neglect them in all our calculations.

### 2.3.3 Further color-superconducting scenarios

The previous sections described idealized scenarios involving two or three light degenerate quark flavors. Eventually, the goal is to describe real world physics. The realistic situation lies between the extreme cases of an infinitely heavy strange quark and a massless strange quark. In the density range relevant for the physics of neutron stars (up to  $10\rho_0$ , corresponding to  $\mu \approx 500$  MeV) the strange quark has to be included with a mass considerably larger than that of up and down quarks.

In the case of the 2SC phase, this could lead to the presence of strange quarks in the system. These can possibly form a spin-1 diquark condensate [44]. The gaps of such condensates, however, would be two to three orders of magnitude smaller than typical spin-0 gaps [34]. Several possible color-superconducting spin-1 phases have been studied [45].

So far, the considerations were restricted to pairing between quarks with equal Fermi momenta. At zero temperature, the Fermi momentum  $p_F$  is defined as

$$p_F = \sqrt{\mu^2 - m^2}, \quad (2.10)$$

hence different Fermi momenta can arise due to different particle masses  $m$  or different chemical potentials  $\mu$ . Condensates of strange and non-strange quarks in a scenario with heavy strange quarks obviously require the pairing between quarks with different Fermi momenta. The situation gets even more involved if one additionally includes the  $\beta$ -equilibrium and electric- and color-charge neutrality conditions which lead to unequal chemical potentials for different quarks. The interplay between unequal quark masses and neutrality enables the formation of various phases.

Imposing charge neutrality disfavors the formation of the 2SC phase [46]. A diquark pair consisting of one up and one down quark has a net electric charge of  $+\frac{1}{3}e$ . The charge chemical potential needed to ensure neutrality at the same time separates the Fermi momenta of up and down quarks, impeding the pairing. However, the formation of a gapless 2SC (g2SC) phase was discussed in [47, 48]. In that phase, the superconducting quark matter only possesses two instead of four gapped fermionic quasiparticles in contrast to the regular 2SC phase. For three-flavor quark matter a similar phase, the gapless CFL (gCFL) phase, has been described [49, 50]. The presence of gapless quasiparticles would have interesting astrophysical consequences [51]. However, it has been shown that the Meissner masses of some gluons become imaginary in the gapless phases at least at zero temperature, signaling that these phases cannot be the true ground state. This is known as the chromomagnetic instability [52, 53, 54].

Apart from these gapless versions of the already discussed phases, other states which only contain one or two out of the three CFL condensates  $s_{AA}$ , Eq. (2.6), have been found at finite temperature [55, 9, 10]. Table 2.3 gives a systematic overview of all possible combinations of the condensates. The  $2\text{SC}_{us}$  phase contains only a condensate of up and strange quarks and the  $2\text{SC}_{ds}$  a condensate of down and strange quarks. The xSC phases each consist of the two condensates which contain quark x.

phase	$s_{22}$	$s_{55}$	$s_{77}$
2SC	✓		
$2\text{SC}_{us}$		✓	
$2\text{SC}_{ds}$			✓
uSC	✓	✓	
dSC	✓		✓
sSC		✓	✓
CFL	✓	✓	✓

Table 2.3: Classification of different color superconducting phases by the corresponding condensates. ✓: non-vanishing.

Another assumption up to this point was that the phase is locally neutral and homogeneous. Abandoning this restriction, various possibilities for the formation of neutral mixed phases, consisting of charged components, arise [56, 57]. The advantage of mixed phases is that not each phase has to satisfy the charge-neutrality conditions by itself, just the combination has to be neutral altogether. To this end, the charge chemical potentials do not have to be as large as in a single neutral phase, and the Fermi surfaces of the pairing quarks are therefore less separated. In the calculation of mixed phases, however, one has to take into account the surface tension and the electric- and color-charge contributions. Unfortunately, the surface tension is only very poorly known. Mixed phases of 2SC matter with non-superconducting quark matter have, for instance, been discussed in [58] including the surface tension. We will not consider mixed phases in this work, but restrict our considerations to locally neutral, homogeneous phases.

A possible outcome of the pairing between quarks with different Fermi momenta is the formation of crystalline superconductors in the so-called LOFF phase which has been named after Larkin and Ovchinnikov [59] and Fulde and Ferrell [60] who explored this phase in the context of electron superconductivity. In connection with QCD, the LOFF phase has first been discussed in [61]. In this state, diquark pairs with non-vanishing total momentum are formed. This possibly leads to a window for the LOFF state in the region where the Fermi surfaces of the pairing quarks are

separated that much that the typical BCS pairing with vanishing total momentum is no longer possible.

As already described in Sec. 2.3.2, chiral symmetry is broken in the CFL phase and thus Goldstone bosons should emerge. Including these into the studies might lead to CFL phases in which Goldstone bosons condense. CFL phases with pion or kaon condensation are discussed in [62, 63]. We will deal with the Goldstone bosons emerging in the CFL phase in Chapters 6 and 7.



## 3 Nambu–Jona-Lasinio model

We will now leave the simplified scenario of two or three flavors of massless quarks and develop a formalism to compute neutral color superconducting phases for three quark flavors with unequal quark masses at moderate densities.

The aim of our calculations is the determination of the phase diagram of dense, strongly-interacting quark matter under compact star conditions, i.e.,  $\beta$ -equilibrated, neutral matter. The first attempt to study the phase diagram of locally neutral three-flavor quark matter as a function of the strange quark mass, the quark chemical potential and the temperature was made in Ref. [9]. The authors found that for small temperatures and not too large strange quark masses, the ground state of matter at high densities is the color-flavor locked (CFL) phase. At some critical strange quark mass, the CFL phase is replaced by a gapless CFL phase. Furthermore, several other color superconducting phases have been found at finite temperature: the 2SC phase, the gapless 2SC phase, and the uSC phase. In Ref. [9], the effect of the strange quark mass was incorporated only approximately through a shift in the strange quark chemical potential,  $\mu_s \rightarrow \mu_s - m_s^2/(2\mu)$  with the quark chemical potential  $\mu = \mu_{\text{baryon}}/3$ . The phase diagram was further developed in Refs. [10, 11] where the strange quark mass was taken into account properly, but still treated as a free parameter.

In this work, we will calculate dynamically generated constituent quark masses self-consistently together with the diquark condensates (see Sec. 3.3). This allows us to study the interplay of quark-antiquark and quark-quark condensates.

Similar approaches have already been applied at zero temperature [64, 65].

### 3.1 Lagrangian

The Nambu–Jona-Lasinio (NJL) model was originally developed by Nambu and Jona-Lasinio in 1961 to describe an effective nucleon-nucleon interaction [66, 67]. The new idea of Nambu and Jona-Lasinio was to describe the mass gap in the nucleon spectrum in analogy to the gap of a superconductor in BCS theory, which had been developed a few years earlier by Bardeen, Cooper, and Schrieffer [36].

The NJL model has later been reinterpreted as an effective model with quark degrees of freedom. For reviews on the NJL model as an effective quark model see, e.g., Refs. [68, 69].

While the NJL model does not contain a confinement mechanism due to its origin in the nucleon-nucleon interaction, it does exhibit spontaneous chiral symmetry breaking

which generates the large constituent fermion masses. Thus, the NJL model is suitable for situations in which chiral symmetry is the relevant feature of QCD and the lack of confinement is less important. This should be the case for deconfined matter at large densities.

We use the generalized NJL Lagrangian

$$\mathcal{L}_{\text{NJL}} = \bar{q}(i\cancel{\partial} - \hat{m})q + \mathcal{L}_{\bar{q}q} \quad (3.1)$$

with a free part and the quark-antiquark interaction part

$$\begin{aligned} \mathcal{L}_{\bar{q}q} = & G \sum_{a=0}^8 [(\bar{q}\tau_a q)^2 + (\bar{q}i\gamma_5\tau_a q)^2] \\ & - K \left[ \det_f (\bar{q}(\mathbf{1} + \gamma_5)q) + \det_f (\bar{q}(\mathbf{1} - \gamma_5)q) \right] , \end{aligned} \quad (3.2)$$

where  $q$  is a quark field with three flavor and three color dimensions and the mass matrix  $\hat{m}$  is a diagonal matrix in flavor space with the bare quark masses as entries:  $\hat{m} = \text{diag}_f(m_u, m_d, m_s)$ .  $\tau_a$  are the Gell-Mann matrices in flavor space extended by  $\tau_0 = \sqrt{2/3}\mathbf{1}$  and  $\det_f$  is the determinant in flavor space.

The NJL model shares the symmetries of QCD which are observed in nature. In the chiral limit, the Lagrangian is symmetric under  $SU(3)_c \times SU(3)_L \times SU(3)_R \times U(1)_V$ . The NJL Lagrangian has a global  $SU(3)$  color symmetry, while in QCD this is a local gauge symmetry. The first term in Eq. (3.2) (with the coupling  $G$ ) is a four-point function and the second term, the 't Hooft term, is a flavor mixing six-point function. It is required to explicitly break the  $U(1)_A$  symmetry in the model because this symmetry is broken anomalously in nature.

For studying color superconductivity a quark-quark interaction  $\mathcal{L}_{qq}$  is added to the Lagrangian in Eq. (3.1):

$$\mathcal{L}_{qq} = H \sum_{A,A'=2,5,7} [(\bar{q}i\gamma_5\tau_A\lambda_{A'}C\bar{q}^T)(q^T Ci\gamma_5\tau_A\lambda_{A'}q) + (\bar{q}\tau_A\lambda_{A'}C\bar{q}^T)(q^T C\tau_A\lambda_{A'}q)] , \quad (3.3)$$

with  $\tau_A$  and  $\lambda_{A'}$  denoting the antisymmetric Gell-Mann matrices in flavor and color space, respectively. The first term in Eq. (3.3) describes a scalar diquark interaction in the color antitriplet, flavor antitriplet channel which gives rise to the diquark condensates  $s_{AA}$  defined in Eq. (2.6). The second term in Eq. (3.3) is the corresponding pseudoscalar diquark interaction which is required to respect chiral symmetry. This term is important to describe the Goldstone bosons in the CFL phase, which will be the topic of Chapters 6 and 7 of this thesis. However, it will not contribute to the mean field.

In order to perform calculations, it is necessary to fix the parameters of the model.



We use the parameter set derived in Ref. [70]:

$$\begin{aligned}
 m_u &= m_d = 5.5 \text{ MeV} , \\
 m_s &= 140.7 \text{ MeV} , \\
 G\Lambda^2 &= 1.835 , \\
 K\Lambda^5 &= 12.36 , \\
 \Lambda &= 602.3 \text{ MeV} .
 \end{aligned}
 \tag{3.4}$$

While  $m_u$  and  $m_d$  are fixed at 5.5 MeV, the other parameters were chosen to reproduce the following observables of vacuum QCD:  $m_\pi = 135.0$  MeV,  $m_K = 497.9$  MeV,  $m_{\eta'} = 957.8$  MeV, and  $f_\pi = 92.4$  MeV.

As the NJL model is non-renormalizable, it is necessary to introduce a cutoff  $\Lambda$ . It is sometimes argued that this cutoff can be seen as a crude implementation of asymptotic freedom, as it cuts off large momenta [69].

Unfortunately, it is not possible to fix the diquark coupling  $H$  in a similar way because there is no diquark spectrum in nature to which it could be fitted. Since the diquark coupling is expected to be of the same order as the quark-antiquark coupling  $G$ , this uncertainty will be accounted for by choosing two different couplings: one “intermediate” coupling scenario with  $H = \frac{3}{4}G$ , and one “strong” coupling case with  $H = G$ .

## 3.2 Thermodynamic potential

The calculation of the thermodynamic potential  $\Omega$  is the main task for the determination of the phase structure. We will see that the gap equations which describe the system in the various phases are given by derivatives of the thermodynamic potential. The same holds for the densities which have to be adjusted to satisfy neutrality conditions. In the end, we will find different solutions for the set of equations. The ground state is simply given by the phase with the highest pressure,  $p = -\Omega$ .

Since the system we want to describe consists of quarks and (in most cases) leptons, the thermodynamic potential is given by the sum of these two contributions

$$\Omega = \Omega_{\text{quark}} + \Omega_{\text{lepton}} .
 \tag{3.5}$$

We will start with the calculation of the quark part.

### Thermodynamic potential of the quarks

To calculate the thermodynamic potential in mean-field approximation, one first has to define the condensates which should be considered in the calculation and then linearize the Lagrangian in the presence of these condensates.

Considering the quark-antiquark interaction, we need the chiral condensates

$$\phi_f = \langle \bar{q}_f q_f \rangle \neq 0, \quad q_f = u, d, s, \quad (3.6)$$

which are responsible for dynamical mass generation. The corresponding cross-flavor condensates

$$\langle \bar{a} b \rangle = 0 \quad \text{for } a \neq b \quad (3.7)$$

are neglected. Furthermore, the pseudoscalar quark-antiquark condensates are not considered:

$$\langle \bar{a} i \gamma_5 b \rangle = 0 \quad \forall a, b. \quad (3.8)$$

For the quark-quark interaction part only the condensates defined in Eq. (2.6) are retained

$$s_{AA} = \langle q^T C \gamma_5 \tau_A \lambda_A q \rangle, \quad A = 2, 5, 7, \quad (3.9)$$

while all others are set to zero:

$$\langle \bar{q} C \gamma_5 \tau_A \lambda_{A'} q \rangle = 0 \quad \text{for } A \neq A', \quad (3.10)$$

$$\langle \bar{q} C \tau_A \lambda_{A'} q \rangle = 0 \quad \forall A, A'. \quad (3.11)$$

Having defined all non-vanishing condensates, we treat all interaction terms analogously to

$$\bar{q} q = \langle \bar{q} q \rangle + \delta(\bar{q} q). \quad (3.12)$$

Rewriting and omitting terms of  $\mathcal{O}(\delta^2)$  finally leads to the linearized Lagrangians

$$\begin{aligned} \mathcal{L}_{qq}^{\text{MF}} = & \bar{u}(4G\phi_u - 2K\phi_d\phi_s)u + \bar{d}(4G\phi_d - 2K\phi_u\phi_s)d \\ & + \bar{s}(4G\phi_s - 2K\phi_u\phi_d)s - 2G(\phi_u^2 + \phi_d^2 + \phi_s^2) + 4K\phi_u\phi_d\phi_s \end{aligned} \quad (3.13)$$

and

$$\mathcal{L}_{qq}^{\text{MF}} = H \sum_{A=2,5,7} (s_{AA}^* (q^T C \gamma_5 \tau_A \lambda_A q) - s_{AA} (\bar{q} \gamma_5 \tau_A \lambda_A C \bar{q}^T) - |s_{AA}|^2). \quad (3.14)$$

Comparing  $\mathcal{L}_{qq}^{\text{MF}}$  with the free part of  $\mathcal{L}_{\text{NJL}}$  reveals how the chiral condensates  $\phi_f$  contribute to the constituent quark masses. Combining the bare quark masses with the corresponding terms of  $\mathcal{L}_{qq}^{\text{MF}}$  leads to the definition of the effective quark masses

$$M_u = m_u - 4G\phi_u + 2K\phi_d\phi_s, \quad (3.15)$$

$$M_d = m_d - 4G\phi_d + 2K\phi_u\phi_s, \quad (3.16)$$

$$M_s = m_s - 4G\phi_s + 2K\phi_u\phi_d. \quad (3.17)$$

Before combining all terms, it is common practice to introduce the gap parameter

$$\Delta_A = -2H s_{AA} \quad (3.18)$$

instead of  $s_{AA}$ .

We arrive at the following expression for the linearized Lagrangian:

$$\mathcal{L}^{MF} = \bar{q}(i\cancel{\partial} - M + \gamma_0\hat{\mu})q + \sum_{A=2,5,7} \left( \frac{1}{2}\bar{q}(\Delta_A\gamma_5\tau_A\lambda_A)C\bar{q}^T - \frac{1}{2}q^T C(\Delta_A^*\gamma_5\tau_A\lambda_A)q \right) - \mathcal{V}, \quad (3.19)$$

where we have additionally added a chemical potential term  $q^\dagger\hat{\mu}q = \bar{q}\gamma_0\hat{\mu}q$ . The matrix  $\hat{\mu}$  is diagonal in color and flavor space and contains the chemical potentials of each quark species as entries. The chemical potentials are combinations of the quark number chemical potential  $\mu$  and electric and color charge chemical potentials (see Sec. 3.3). The Potential  $\mathcal{V}$  contains all terms which are independent of the quark fields,

$$\mathcal{V} = -4K\phi_u\phi_d\phi_s + 2G(\phi_u^2 + \phi_d^2 + \phi_s^2) + \frac{1}{4H}(\Delta_2^2 + \Delta_5^2 + \Delta_7^2). \quad (3.20)$$

At this point it is convenient to apply the Nambu-Gorkov formalism. One introduces the charge-conjugate fields

$$q^C = C\bar{q}^T, \quad \bar{q}^C = q^T C. \quad (3.21)$$

Treating  $q$  and  $q^C$  as independent variables, the bispinor fields

$$\psi = \frac{1}{\sqrt{2}} \begin{pmatrix} q \\ q^C \end{pmatrix}, \quad \bar{\psi} = \frac{1}{\sqrt{2}} (\bar{q}, \bar{q}^C) \quad (3.22)$$

are defined. Using these fields, the Lagrangian adopts the compact form

$$\mathcal{L}^{MF} = \bar{\psi} \begin{pmatrix} i\cancel{\partial} - M + \gamma_0\hat{\mu} & \sum_{A=2,5,7} \Delta_A\gamma_5\tau_A\lambda_A \\ -\sum_{A=2,5,7} \Delta_A^*\gamma_5\tau_A\lambda_A & -i\cancel{\partial} - M - \gamma_0\hat{\mu} \end{pmatrix} \psi - \mathcal{V}. \quad (3.23)$$

Switching to momentum space leads to

$$\tilde{\mathcal{L}}^{MF} = \tilde{\bar{\psi}} S^{-1} \tilde{\psi} - \tilde{\mathcal{V}}, \quad (3.24)$$

with the inverse dressed propagator

$$S^{-1} = \begin{pmatrix} \cancel{\not{p}} - M + \hat{\mu}\gamma_0 & \sum_{A=2,5,7} \Delta_A\gamma_5\tau_A\lambda_A \\ -\sum_{A=2,5,7} \Delta_A^*\gamma_5\tau_A\lambda_A & \cancel{\not{p}} - M - \hat{\mu}\gamma_0 \end{pmatrix}. \quad (3.25)$$

After these transformations we are ready to calculate the quark thermodynamic potential (per volume) at temperature  $T$ :

$$\Omega = -T \sum_n \int \frac{d^3p}{(2\pi)^3} \frac{1}{2} \text{Tr} \ln \left( \frac{1}{T} S^{-1}(i\omega_n, \vec{p}) \right) + \mathcal{V}, \quad (3.26)$$

with the fermionic Matsubara frequencies  $i\omega_n = (2n + 1)\pi T$ . The factor  $\frac{1}{2}$  balances the formal doubling of the degrees of freedom.

Using  $\text{Tr} \ln M = \ln \det M$ , we get

$$\text{Tr} \ln \left( \frac{1}{T} S^{-1} \right) = \ln \det \frac{S^{-1}}{T}. \quad (3.27)$$

The determinant of the inverse propagator can be calculated by first diagonalizing  $S^{-1}$  numerically. The procedure is described in Appendix B.1. We obtain

$$\det \frac{S^{-1}}{T} = \prod_{j=1}^{72} \frac{i\omega_n - \varepsilon_j}{T} = \prod_{j=1}^{18} \frac{(\omega_n^2 + \varepsilon_j^2)^2}{T^4}, \quad (3.28)$$

with  $\varepsilon_j$  being the eigenvalues of  $A(\vec{p}) = p^0 \mathbb{1} - \gamma_0 S^{-1}$  (see Appendix B.1). Each eigenvalue is twofold degenerate and for each positive eigenvalue  $\varepsilon_j$  a negative one of the same magnitude exists. Using the relation [71]

$$\sum_{n=-\infty}^{\infty} \ln \left[ \frac{1}{T^2} (\omega_n^2 + \varepsilon^2) \right] = \frac{|\varepsilon|}{T} + \ln \left[ 1 + \exp \left( -\frac{|\varepsilon|}{T} \right) \right], \quad (3.29)$$

the Matsubara sum can be evaluated, yielding

$$\Omega_{\text{quark}} = \frac{T}{2\pi^2} \sum_{i=1}^{18} \int dp p^2 \left\{ \frac{|\varepsilon_i|}{T} + 2 \ln \left( 1 + \exp \left[ -\frac{|\varepsilon_i|}{T} \right] \right) \right\} \quad (3.30)$$

for the thermodynamic potential of the quarks. The momentum integral has to be regularized by the three-momentum cutoff defined in Eq. (3.4).

### Thermodynamic potential of the leptons

The leptonic thermodynamic potential is the sum of the thermodynamic potentials of all leptons. For the moment, we only consider the charged leptons and neglect the neutrinos, which need only be included for calculations concerning the first seconds of the protoneutron star evolution when they are trapped. We will defer this issue to Chapter 5. Regarding the charged leptons, only electrons and muons have to be included in the calculation, because the  $\tau$  has a mass of  $\sim 1.8 \text{ GeV}$  and will therefore not be present in any significant abundance. For the masses of the lighter leptons we use [72]

$$\begin{aligned} m_e &= 0.511 \text{ MeV}, \\ m_\mu &= 105.658 \text{ MeV}. \end{aligned} \quad (3.31)$$

The leptons are not affected by the strong interaction and can be treated as a gas of free fermions. For the thermodynamic potential of the leptons (and their respective antiparticles) one then finds

$$\Omega_l = -gT \int \frac{d^3p}{(2\pi)^3} \left\{ \ln \left( 1 + \exp \left[ -\frac{1}{T}(E_l - \mu_l) \right] \right) + \ln \left( 1 + \exp \left[ -\frac{1}{T}(E_l + \mu_l) \right] \right) \right\} \quad (3.32)$$

with  $E_l = \sqrt{\vec{p}^2 + m_l^2}$  and the degeneracy factor  $g$  which is 2 for electrons and muons to account for the two possible spin directions. In the  $T \rightarrow 0$  limit, the logarithms turn into step functions.

### 3.3 Gap equations and neutrality conditions

The ground state of any system has to be the minimum of the thermodynamic potential. Therefore,  $\phi_f$  and  $\Delta_A$  must satisfy the conditions

$$\frac{\partial \Omega}{\partial \phi_f} = 0 \quad \text{and} \quad \frac{\partial \Omega}{\partial \Delta_A} = 0. \quad (3.33)$$

These so-called gap equations have to be solved simultaneously.

Several constraints have to be taken into account while solving Eq. (3.33) under neutron star conditions. There,  $\beta$  equilibrium is maintained by the processes

$$d_c \rightleftharpoons u_c + e^- + \bar{\nu}_e, \quad (3.34)$$

$$s_c \rightleftharpoons u_c + e^- + \bar{\nu}_e, \quad (3.35)$$

where the conserved charges are baryon number, color and electric charge. Since the neutrinos leave the neutron star, the lepton number is not conserved. Additional constraints arise from the requirement of local electric and color neutrality. Color neutrality is defined as the equality of the number densities of red, green, and blue color charges. Strictly speaking, a system of finite size should be a color singlet. However, it has been shown that the difference is small [73]. For each conserved charge we have one chemical potential. In our case, these are the electric charge chemical potential  $\mu_Q$  and three color charge chemical potentials,  $\mu_r$ ,  $\mu_g$ , and  $\mu_b$ . Usually  $\mu_r$ ,  $\mu_g$ , and  $\mu_b$  are not used directly, but in the linear combinations

$$\mu = \frac{1}{3}\mu_r + \frac{1}{3}\mu_g + \frac{1}{3}\mu_b, \quad (3.36)$$

$$\mu_3 = \frac{1}{2}\mu_r - \frac{1}{2}\mu_g, \quad (3.37)$$

$$\mu_8 = \frac{1}{2\sqrt{3}}\mu_r + \frac{1}{2\sqrt{3}}\mu_g - \frac{1}{\sqrt{3}}\mu_b. \quad (3.38)$$

The chemical potential of each quark is then given by a linear combination of  $\mu$ ,  $\mu_3$ ,  $\mu_8$ , and  $\mu_Q$  corresponding to its charge content, e.g., for a red up quark this is

$$\mu_{u,r} = \underbrace{\mu + \mu_3 + \frac{1}{\sqrt{3}}\mu_8}_{\text{color content}} + \underbrace{\frac{2}{3}\mu_Q}_{\text{electric content}}. \quad (3.39)$$

It will prove to be useful to have the chemical potentials of the individual quark species at hand for the discussion of the phase diagrams:

$$\begin{aligned} \mu_{ur} &= \mu + \mu_3 + \frac{1}{\sqrt{3}}\mu_8 + \frac{2}{3}\mu_Q, \\ \mu_{ug} &= \mu - \mu_3 + \frac{1}{\sqrt{3}}\mu_8 + \frac{2}{3}\mu_Q, \\ \mu_{ub} &= \mu - \frac{2}{\sqrt{3}}\mu_8 + \frac{2}{3}\mu_Q, \\ \mu_{dr} &= \mu + \mu_3 + \frac{1}{\sqrt{3}}\mu_8 - \frac{1}{3}\mu_Q, \\ \mu_{dg} &= \mu - \mu_3 + \frac{1}{\sqrt{3}}\mu_8 - \frac{1}{3}\mu_Q, \\ \mu_{db} &= \mu - \frac{2}{\sqrt{3}}\mu_8 - \frac{1}{3}\mu_Q, \\ \mu_{sr} &= \mu + \mu_3 + \frac{1}{\sqrt{3}}\mu_8 - \frac{1}{3}\mu_Q, \\ \mu_{sg} &= \mu - \mu_3 + \frac{1}{\sqrt{3}}\mu_8 - \frac{1}{3}\mu_Q, \\ \mu_{sb} &= \mu - \frac{2}{\sqrt{3}}\mu_8 - \frac{1}{3}\mu_Q. \end{aligned} \quad (3.40)$$

As long as we do not need to include lepton-number conservation, the chemical potentials of electrons and muons are just given by their electric charge content:

$$\mu_{e/\mu} = -\mu_Q. \quad (3.41)$$

The neutrality conditions in terms of number densities  $n_i$  are then given by

$$n_3 = n_r - n_g = -\frac{\partial\Omega}{\partial\mu_3} = 0, \quad (3.42)$$

$$n_8 = \frac{1}{\sqrt{3}}n_r + \frac{1}{\sqrt{3}}n_g - \frac{2}{\sqrt{3}}n_b = -\frac{\partial\Omega}{\partial\mu_8} = 0, \quad (3.43)$$

for color neutrality and

$$n_Q = \frac{2}{3}n_u - \frac{1}{3}(n_d + n_s) - n_e - n_\mu = -\frac{\partial\Omega_{\text{quark}}}{\partial\mu_Q} - \frac{\partial\Omega_{\text{lepton}}}{\partial\mu_Q} = 0 \quad (3.44)$$

for electric neutrality. The lepton density can be obtained by directly taking the derivative of Eq. (3.32) with respect to  $\mu_Q$ :

$$\begin{aligned}
 n_l &= -\frac{\partial\Omega_l}{\partial\mu_Q} \\
 &= g \int \frac{d^3p}{(2\pi)^3} \left( \frac{1}{\exp\left[\frac{1}{T}(E_p - \mu_l)\right] + 1} - \frac{1}{\exp\left[\frac{1}{T}(E_p + \mu_l)\right] + 1} \right). \tag{3.45}
 \end{aligned}$$

In the  $T \rightarrow 0$  limit Eq. (3.45) turns into an integration over step functions.

The quark densities and the gap equations are calculated by numerical differentiation.<sup>1</sup> The quark chemical potential  $\mu$  and the temperature  $T$  are the free parameters of our calculations. When the gap equations are solved simultaneously with the neutrality conditions for each combination of the quark chemical potential  $\mu$  and temperature  $T$ , these nine coupled equations fix the chiral order parameters  $\phi_f$ , the color superconducting order parameters  $\Delta_A$ , and the electric ( $\mu_Q$ ) and color charge ( $\mu_3$  and  $\mu_8$ ) chemical potentials.

---

<sup>1</sup>Another possibility for computing the densities and gap equations will be presented in Chapter 6.





# 4 Phase diagrams of neutral quark matter

In this section we present phase diagrams for dense, locally neutral three-flavor quark matter calculated within the approach presented in the previous chapter. To that end, we solve the gap equations and neutrality conditions for a range of temperatures and chemical potentials. For most combinations of  $T$  and  $\mu$  more than one solution of the set of equations exists. These solutions correspond to different phases and can be classified according to Tab. 2.3. In addition, we find at least one solution for unpaired quark matter, i. e., with  $\Delta_2 = \Delta_5 = \Delta_7 = 0$ .

In the definition of the phases in Tab. 2.3, only the gap parameters  $\Delta_A$  were used as order parameters, while the quark-antiquark condensates  $\phi_f$  were ignored. In the chiral limit, the  $\phi_f$  would be good order parameters, but in our case, chiral symmetry is explicitly broken by nonzero current quark masses. Therefore, the quark-antiquark condensates never vanish completely. The fact that we cannot define new phases in terms of  $\phi_f$  does not exclude discontinuous changes in these condensates at some line in the phase diagram. It is expected that this “chiral” phase transition is of first order at low temperatures, even for finite quark masses. At higher temperatures, the phase transition line could end in a critical end point beyond which there is only a smooth crossover. Since such behavior has been found in NJL-model studies before, see e. g., Refs. [74, 75, 76], we expect similar results.

Finally, we check the low-energy quasiparticle spectrum for gapless modes. As the gapless phases are known to be unstable at least at zero temperature, this allows us to identify these critical regions of the phase diagram where the ground state has to be characterized by some unconventional pairing which is not considered in this work.

## 4.1 Intermediate coupling

The phase diagram for intermediate coupling strength,  $H = \frac{3}{4}G$ , is shown in Fig. 4.1. For a better understanding of the phase structure and the properties therein, the quark masses, gap parameters and charge chemical potentials,  $\mu_3$ ,  $\mu_8$ , and  $\mu_Q$ , are illustrated in Fig. 4.2 for three different temperatures ( $T = 0, 20$ , and  $40$  MeV).

In the region of small quark chemical potentials ( $\mu < 367$  MeV at  $T = 0$ ) we find a phase in which chiral symmetry is broken (labeled  $\chi$ SB in Fig. 4.1). In this phase, the quarks have large constituent masses of  $M_u = M_d = 367.6$  MeV,  $M_s = 549.5$  MeV

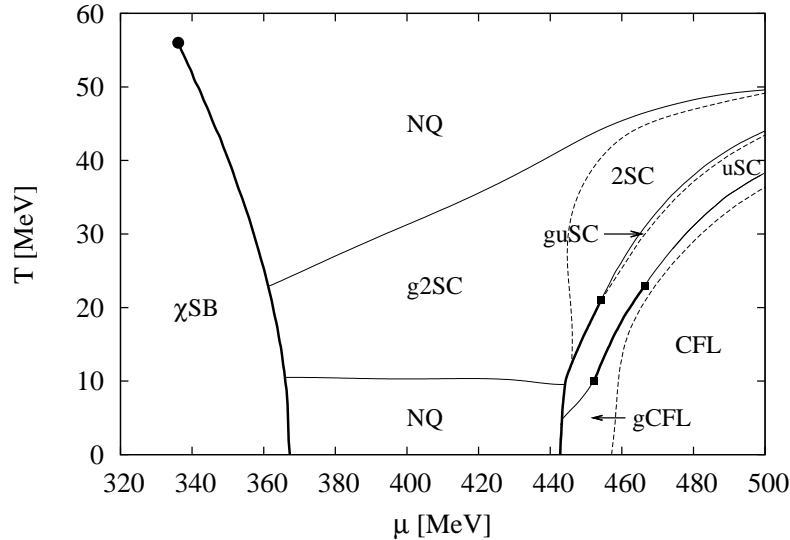


Figure 4.1: Phase diagram of neutral quark matter for an intermediate coupling strength of  $H = \frac{3}{4}G$ . Thick lines indicate first-order phase transitions and thin lines second-order transitions. The dashed lines indicate the (dis)appearance of gapless modes in different phases, and they do not correspond to phase transitions.

at  $T = 0$  (see Fig. 4.2). With increasing temperature, this phase converts to a phase of unpaired quark matter with relatively small constituent quark masses (labeled NQ in Fig. 4.1). In the following, we will simply refer to this phase as the normal phase. As explained before, there is no need for a chiral phase transition because chiral symmetry is broken explicitly in our model. Nevertheless, we find a line of a first-order chiral phase transition for quark chemical potentials between 336 and 367 MeV, which are of the order of the up and down constituent quark masses. The phase boundary starts at  $\mu \approx 367$  MeV for zero temperature. At this point the light quark masses drop considerably. The values in the normal phase are  $M_u = 82.1$  MeV and  $M_d = 62.6$  MeV at the phase transition. The strange quark drops by a smaller amount to  $M_s = 465.8$  MeV at  $T = 0$ . The drop in the strange quark mass is induced by the flavor mixing 't Hooft interaction.

For larger temperatures, the drop in the quark masses decreases as the critical end point of the chiral phase transition line at  $(T_c, \mu_c) \approx (56, 336)$  MeV is approached. The location of the critical end point is consistent with other mean-field studies of NJL models which use similar parameter sets [74, 76]. Since the condition of charge neutrality was not imposed in these studies, one cannot expect perfect agreement.

Turning our attention to intermediate chemical potentials of around 370 to 450 MeV, we find the (gapless) 2SC phase sandwiched between two regions of normal quark mat-

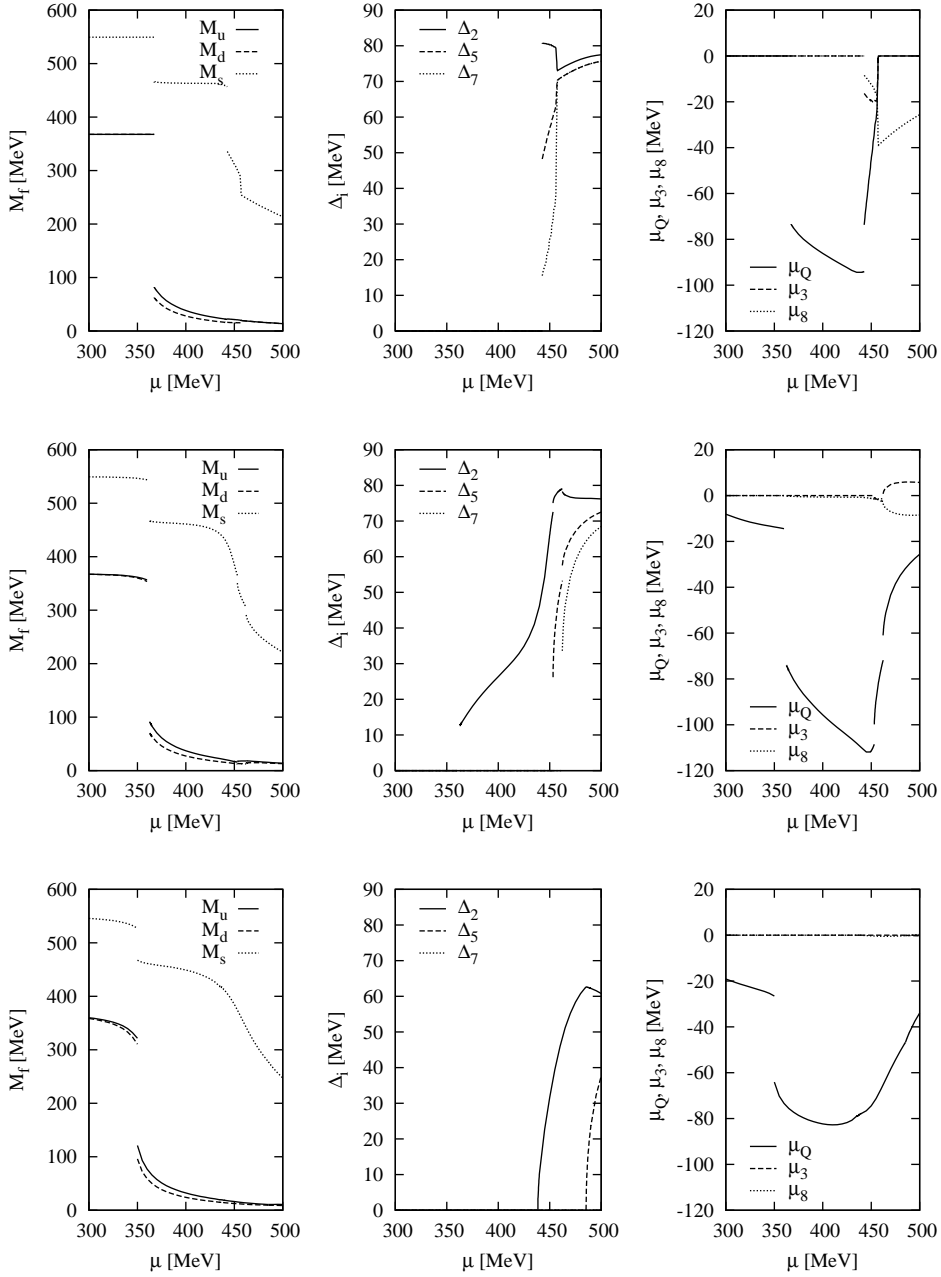


Figure 4.2: Quark masses, gap parameters, and electric and color charge chemical potentials as functions of the quark chemical potential  $\mu$  for  $T = 0$  (upper panels),  $T = 20$  MeV (middle panels), and  $T = 40$  MeV (lower panels). The diquark coupling strength is  $H = \frac{3}{4}G$ .

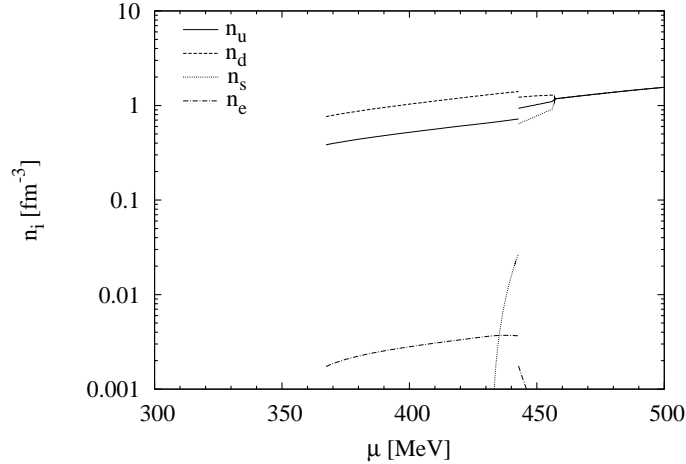


Figure 4.3: Number densities of quarks and electrons as functions of the quark chemical potential  $\mu$  at  $T = 0$  MeV for  $H = \frac{3}{4}G$ . Muons are not present under these conditions.

ter. To explain this behavior, we have to examine the masses and charge chemical potentials shown in Fig. 4.2. As explained above, the light quark masses drop dramatically at the chiral phase transition, whereas the strange quark mass drops only moderately. Thus, there are no strange quarks in the system at  $T = 0$  for the given range of chemical potentials, and the system merely consists of up and down quarks together with a small fraction of electrons, see Fig. 4.3. With this small amount of electrons nearly twice as many down quarks as up quarks are needed to ensure neutrality, leading to an electric charge chemical potential  $\mu_Q$  of  $-73$  to  $-94$  MeV, see Fig. 4.2. At the same time this charge chemical potential produces a splitting of the up and down quark Fermi momenta of  $\delta p_F = \mu_Q$  which is large enough to prevent diquark pairing. Thus, we find a normal quark matter phase at low temperatures. The amount of electrons which is induced by the electric charge chemical potential is rather small and makes nearly no contribution to charge neutrality (cf. Fig. 4.3).

For higher temperatures ( $\gtrsim 10$  MeV) thermal smearing of the Fermi surfaces allows the formation of diquark condensates consisting of an up and a down quark, and the normal quark matter phase is replaced by the g2SC phase. At larger temperatures ( $T = 23$  MeV at  $\mu = 362$  MeV) the diquark condensates are destroyed. For bigger quark chemical potential this happens at still higher temperatures ( $T = 49.6$  MeV at  $\mu = 500$  MeV).

In Fig. 4.3, we find the first strange quarks at  $\mu \approx 432$  MeV. This is the point where the strange-quark chemical potential  $\mu_s = \mu - \frac{1}{3}\mu_Q$  ( $\mu_Q = -94$  MeV,  $\mu_3 = \mu_8 = 0$ ) reaches the strange-quark mass of  $\sim 463$  MeV. The amount of strange quarks increases with the quark chemical potential. At  $\mu \approx 443$  MeV, the system undergoes a first-order

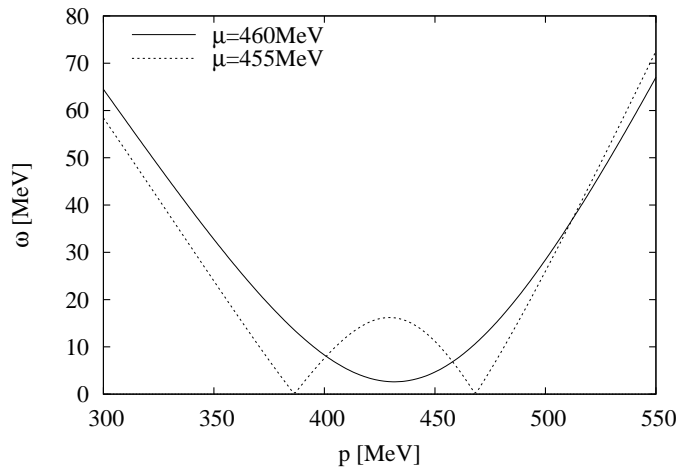


Figure 4.4: Quasiparticle spectrum  $\omega(p)$  of a mode in the down-strange sector which becomes gapless for  $\mu < 457$  MeV as a function of the absolute value of the three-momentum  $\vec{p}$ .

phase transition to the gapless CFL (gCFL) phase and the strange quark mass drops by 121 MeV to  $\sim 335$  MeV. In the gCFL phase, we have diquark pairing between all three quark flavors. Since the strange quarks are still rather heavy, a regular CFL pairing with equal number densities of the three quark flavors is still not possible. Therefore, a small amount of electrons is necessary to satisfy the neutrality constraint. With increasing quark chemical potential, the strange quark mass decreases further and the strange-nonstrange Cooper pairing gets stronger until the system enters the regular CFL phase at  $\mu \approx 457$  MeV.

At the transition to the CFL phase, the charge chemical potential  $\mu_Q$  and the electron density go to zero. At  $T = 0$ , the regular CFL phase is electrically neutral without any electrons because the pairing mechanism enforces equal number densities for all three quark flavors,  $n_u = n_d = n_s$ . This even holds for unequal quark masses as long as the regular CFL phase is stable [77]. Due to the neutrality, the electron density can serve as an order parameter to distinguish the CFL phase from the gCFL phase at  $T = 0$ . Furthermore, the up-strange and down-strange diquark condensates are equal, while the diquark condensate of the two light quarks is slightly bigger (see Fig. 4.2). In the regular CFL phase only the color chemical potential  $\mu_8$  is needed to ensure color neutrality at zero temperature and  $\mu_3$  vanishes. Since all three characteristics which distinguish the CFL and gCFL phases are only present at  $T = 0$ , we have to resort to the dispersion relations  $\omega(p)$  of the quasiparticles to detect the gapless CFL phase at finite temperature. Fig. 4.4 visualizes the appearance of the gapless mode at  $T = 0$ .

To obtain the correct phase structure, it is important to consider the gapless version of the CFL phase and allow for non-vanishing  $\mu_3$  and  $\mu_Q$  at  $T = 0$ . Fig. 4.5 shows the

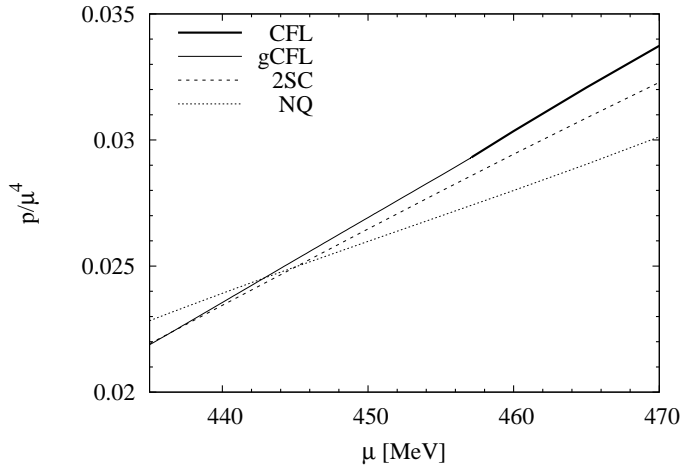


Figure 4.5: Pressure divided by  $\mu^4$  for different phases at  $T = 0$  and  $H = \frac{3}{4}G$ .

pressure (divided by  $\mu^4$ ) of the different solutions of the gap equations and neutrality conditions corresponding to the (g)CFL, 2SC and NQ phases. Without the gapless CFL phase there would be an interval from  $\mu \approx 445$  MeV to  $\mu \approx 457$  MeV where the 2SC phase would be the phase with the highest pressure and was therefore incorrectly identified as the ground state in Ref. [64] where gapless phases have not been taken into account.

In the finite temperature, high density ( $\mu \gtrsim 450$  MeV) part of the phase diagram, we find a band of the (g)uSC phase. The uSC phase contains up-down and up-strange diquark pairs, but no down-strange pairs. The appearance of the uSC phase can be explained by the simultaneous occurrence of a relatively large negative electric charge chemical potential with a large strange quark mass (see Fig. 4.2, middle row). This results in a splitting of the up and down Fermi momenta only through the charge chemical potential. The negative  $\mu_Q$  enhances the pairing between up and strange quarks because it reduces the stress induced by the strange quark mass. This enhancement does not occur for down-strange pairs since they both feel the same charge chemical potential.

The combination of first and second-order phase transitions from the CFL to the uSC phase is likely to be an accidental property in the model for the given set of parameters.

For completeness, we show the quark and lepton densities for  $T = 20$  and 40 MeV in Fig. 4.6. Due to the finite temperature, we have a finite particle density for all quarks and leptons in all phases. Since the electron density never vanishes, it cannot be used to distinguish the CFL and gCFL phase as in the zero temperature case. Furthermore, we observe that the densities of the three quark flavors are no longer equal in the CFL phase because this would not be compatible with the neutrality condition due to the

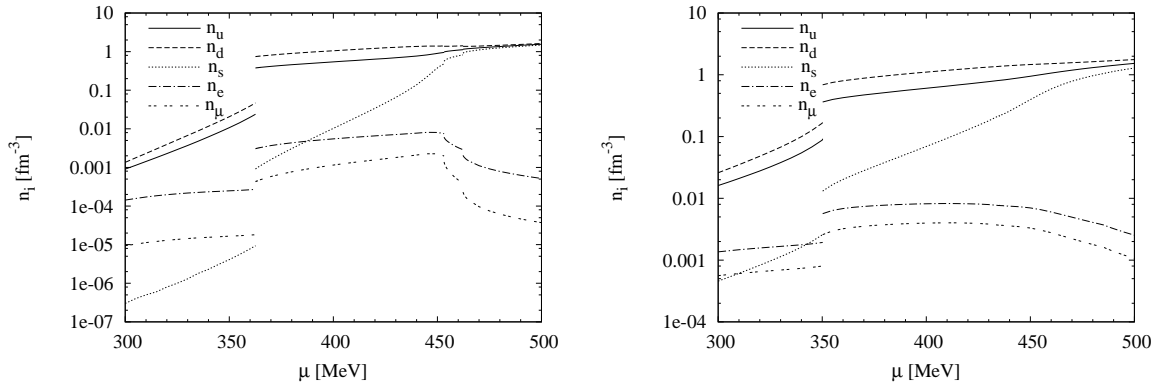


Figure 4.6: Number densities of quarks and leptons as functions of the quark chemical potential  $\mu$  at  $T = 20$  MeV (left panel) and  $T = 40$  MeV (right panel) for  $H = \frac{3}{4}G$ .

presence of negatively charged leptons in the system.

## 4.2 Strong coupling

Naturally, the structure of the phase diagram depends on the parameters of the model. To check the influence of the diquark-coupling strength, we now present the phase diagram for a larger coupling constant  $H = G$  in Fig. 4.7 and compare it with Fig. 4.1. The quark masses, gap parameters, and charge chemical potentials for three different temperatures ( $T = 0, 40,$  and  $60$  MeV) are shown in Fig. 4.8.

The most striking difference between this phase diagram and the one for intermediate coupling appears for intermediate chemical potentials and low temperatures: for strong coupling there is no normal quark matter phase for small temperatures. Even for zero temperature, the system directly enters the color-superconducting 2SC phase after the chiral phase transition. This can be explained by the higher diquark coupling strength which leads to a higher gain in energy for the formation of a Cooper pair and enables pairing even for larger differences between the Fermi momenta of up and down quarks. The  $\chi$ SB phase itself is not affected by the change in the diquark coupling strength, but the stronger 2SC phase shifts the chiral phase boundary to slightly smaller chemical potentials (to  $\mu = 358.6$  MeV for  $T = 0$ ).

The 2SC phase also spans a larger region in the temperature direction. For  $\mu = 336$  MeV it does not undergo a second-order phase transition to the NQ phase up to a temperature of more than 59 MeV. For higher chemical potentials this happens for temperatures of nearly 78 MeV, compared to 50 MeV for intermediate coupling scenario.

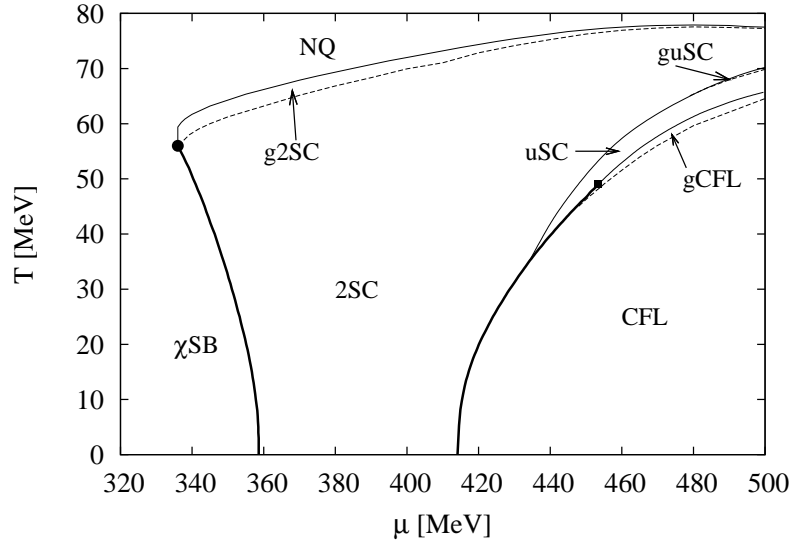


Figure 4.7: Phase diagram of neutral quark matter for strong coupling,  $H = G$ . Thick lines indicate first-order phase transitions and thin lines second-order transitions. The dashed lines indicate the (dis)appearance of gapless modes in different phases, and they do not correspond to phase transitions.

The stronger diquark coupling leads to bigger gap parameters. For example,  $\Delta_2 = 123.2$  MeV for  $T = 0$  and  $\mu = 500$  MeV, compared to 77.5 MeV in the intermediate coupling case. It also results in a considerable reduction of the size of the gapless phases.

In the 2SC phase, an electric charge chemical potential of around  $-200$  MeV is necessary to ensure neutrality at  $T = 0$  (see Fig. 4.8). This large negative  $\mu_Q$  leads to the presence of muons in the whole 2SC region even at zero temperature. Furthermore, a small amount of (blue) strange quarks is already present at  $\mu = 388$  MeV for  $T = 0$  (the amount is too small to be visible in Fig. 4.9), compared to  $\mu = 432$  MeV in the intermediate coupling case. At  $\mu = 388$  MeV the electric charge chemical potential  $\mu_Q = -210.9$  MeV and the color charge chemical potential  $\mu_8 = -5$  MeV lead to  $\mu_{sb} = \mu - \frac{2}{\sqrt{3}}\mu_8 - \frac{1}{3}\mu_Q = 464$  MeV for the blue strange quarks, which is larger than the strange quark mass  $M_s = 463.6$  MeV. The chemical potentials of the red and green strange quarks are smaller by 8.7 MeV ( $= \sqrt{3}\mu_8$ , cf. Eq. (3.40)). Already at  $\mu \approx 414$  MeV a first-order phase transition to the CFL phase occurs. The CFL phase profits most of the increased coupling strength, because all quarks form diquark pairs resulting in a larger energy gain compared to phases where only part of the quarks form diquark pairs. This explains the enormous growth of the CFL phase. For temperatures between 35 and 70 MeV we again find a thin slice of uSC quark matter between CFL and 2SC phase.



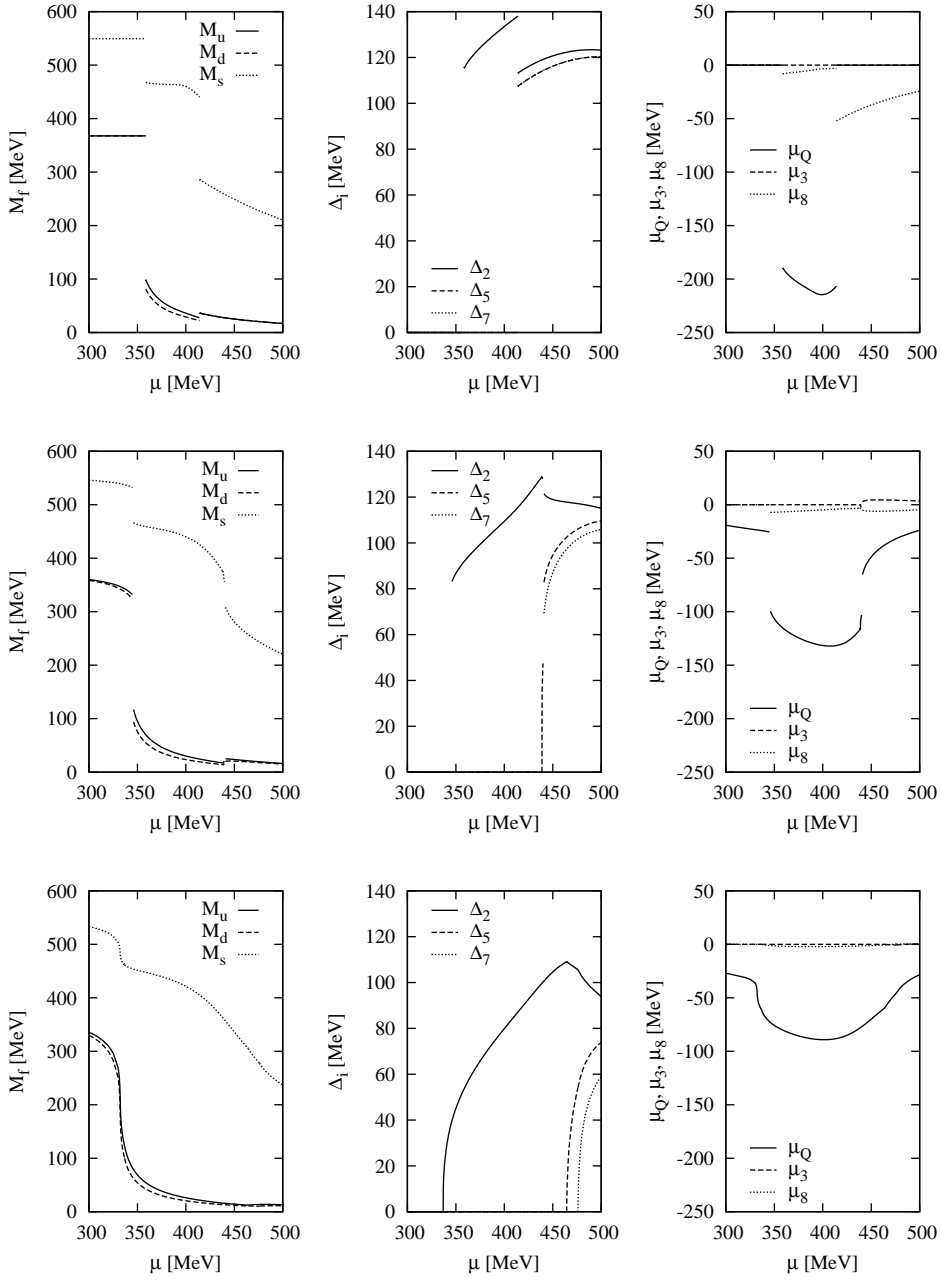


Figure 4.8: Quark masses, gap parameters, and electric and color charge chemical potentials as functions of the quark chemical potential  $\mu$  for  $T = 0$  (three upper panels),  $T = 40$  MeV (three middle panels), and  $T = 60$  MeV (three lower panels). The diquark coupling strength is  $H = G$ .

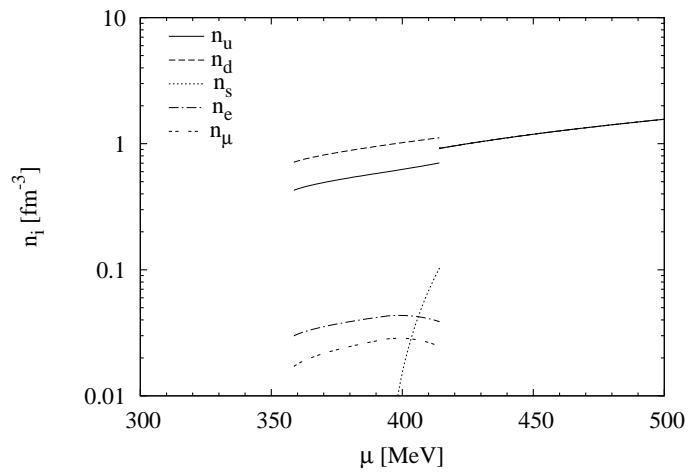


Figure 4.9: Number densities of quarks and leptons as functions of the quark chemical potential  $\mu$  at  $T = 0$  MeV for  $H = G$ .

## 5 The effect of neutrino trapping

A protoneutron star is the primary remnant of a supernova explosion. It is the preliminary stage of a neutron star and has a temperature of tens of MeV. In the first few seconds after the explosion, neutrinos are trapped inside the protoneutron star [78]. After some seconds they leave the star, which cools down to temperatures below 1 MeV to form a neutron star.

Neutrino trapping can be included into the considerations presented here by introducing a finite neutrino (or, more precisely lepton-number) chemical potential. This is expected to have a considerable effect on the phase diagram. It has been found that a finite neutrino chemical potential favors the 2SC phase and disfavors the CFL phase [64]. We will extend the analysis of Ref. [64] and perform a systematic survey of the phase diagram in the space of temperature, quark chemical potential, and neutrino chemical potential.

### 5.1 Neutrino trapping

The inclusion of neutrino trapping adds lepton numbers as additional conserved quantities to the system. In Chapter 3 we excluded the charged  $\tau$  from the model computations due to its high mass. Neglecting neutrino oscillations, we can therefore also exclude the  $\tau$  neutrinos. For the conserved lepton numbers, the electron-lepton number and muon-lepton number chemical potentials,  $\mu_{L_e}$  and  $\mu_{L_\mu}$ , have to be implemented. For the neutrinos, whose only “charge” is lepton number, this implies

$$\mu_{\nu_e} = \mu_{L_e}, \quad \mu_{\nu_\mu} = \mu_{L_\mu}. \quad (5.1)$$

As electrons and the muons carry lepton number and electric charge, their chemical potentials are linear combinations of the corresponding quantities

$$\mu_e = \mu_{L_e} - \mu_Q, \quad \mu_\mu = \mu_{L_\mu} - \mu_Q. \quad (5.2)$$

The contribution of the neutrinos to the thermodynamic potential has already been defined in Eq. (3.32). For massless neutrinos the energy is  $E_{\nu_{e/\mu}} = |\vec{p}_{\nu_{e/\mu}}|$ , and we have to use the degeneracy factor  $g = 1$  because they have only one spin direction. In the limit  $T \rightarrow 0$ , the logarithms become step functions and the thermodynamic potential is just given by

$$\Omega_{\nu_{e/\mu}} = -\frac{1}{24\pi^2} \mu_{\nu_{e/\mu}}^4. \quad (5.3)$$

The neutrino density has been defined in Eq. (3.45) and has a simple zero temperature limit as well:

$$n_{\nu_{e/\mu}} = \frac{1}{6\pi^2} \mu_{\nu_{e/\mu}}^3. \quad (5.4)$$

In the following, we will use  $\mu_{L_e}$  and  $\mu_{L_\mu}$  as free parameters together with the quark chemical potential  $\mu$  and the temperature  $T$ .

Another possibility would be to treat the lepton fractions  $Y_{L_e}$  and  $Y_{L_\mu}$  as free parameters. These are defined as

$$Y_{L_e} \equiv \frac{n_{L_e}}{n_{\text{baryon}}} \quad \text{and} \quad Y_{L_\mu} \equiv \frac{n_{L_\mu}}{n_{\text{baryon}}} \quad (5.5)$$

with the baryon density

$$n_{\text{baryon}} \equiv \frac{n_{\text{quark}}}{3} = -\frac{1}{3} \frac{\partial \Omega_{\text{quark}}}{\partial \mu}. \quad (5.6)$$

Fixing the lepton fractions is useful if one wants to map the initial state of matter inside a protoneutron star at very early times, when the fractions are approximately the same as in the progenitor star (i. e.,  $Y_{L_e} \approx 0.4$  and  $Y_{L_\mu} = 0$  [79]). However, this procedure becomes ambiguous in the vicinity of first-order phase transitions, where the baryon number density and the lepton fractions are discontinuous in general. For this reason, we study the phase structure at fixed values of  $\mu$ ,  $\mu_{L_e}$ , and  $\mu_{L_\mu}$ , as these chemical potentials change continuously at the boundaries of first-order phase transitions.

In the following we will assume  $\mu_{L_\mu} = 0$ . This is expected to be a good approximation inside a protoneutron star with the initial condition  $Y_{L_\mu} = 0$ . We can therefore, for simplicity, call the electron lepton-number chemical potential simply neutrino chemical potential, since no confusion is possible.

Before beginning our calculations, it is helpful to consider the qualitative effects of a finite neutrino chemical potential on the phase structure: So far, the 2SC phase suffered from the charge neutrality condition because it requires nearly twice as many down quarks in the system as up quarks. This demands different Fermi momenta for up and down quarks and naturally impedes the diquark pairing between these quarks. Switching on a finite neutrino chemical potential does not only feed neutrinos into the system but electrons as well (see Eq. (5.2)). These electrons help to achieve charge neutrality without requiring a large negative charge chemical potential  $\mu_Q$  which separates the Fermi surfaces of up and down quarks. In the CFL phase the situation is reversed. The CFL phase is electrically neutral without any electrons at  $T = 0$ . Therefore, a finite neutrino chemical potential can only spoil CFL-type pairing. This has previously been discussed in [64].

## 5.2 Influence on the phase structure

The following calculations of the phase structure under the influence of a finite neutrino chemical potential will be performed with the diquark coupling strength  $H = \frac{3}{4}G$ .

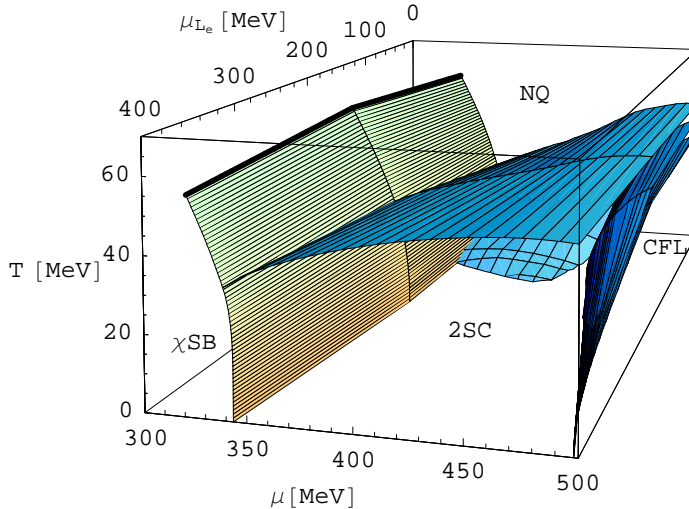


Figure 5.1: General structure of the phase diagram of neutral dense quark matter in the three-dimensional space spanned by the quark chemical potential  $\mu$ , the electron lepton-number chemical potential  $\mu_{Le}$ , and the temperature  $T$ . Taken from [21].

This intermediate-coupling scenario exhibits a more interesting phase structure than the strong-coupling scenario in the previous chapter.

The inclusion of  $\mu_{Le}$  as an additional free parameter extends the previously studied  $T$ - $\mu$  phase diagram to a third dimension. The corresponding three-dimensional phase diagram is shown in Fig. 5.1 providing an overview of the phase structure. For the sake of clarity, only the four main phases ( $\chi$ SB, NQ, 2SC, and CFL) are labeled. There is an unlabeled thin slice of the uSC phase squeezed between the CFL and 2SC phase. The CFL phase shrinks and finally gets replaced by the 2SC phase with increasing  $\mu_{Le}$  (moving to the foreground of the phase diagram). The normal quark matter phase at low temperature vanishes in that direction as well, giving room to the 2SC phase.

For a detailed discussion, we will now present two-dimensional slices of the phase diagram in Fig. 5.1. Note, that the backmost plane is identical with the phase diagram presented in Fig. 4.1.

### 5.2.1 $T$ - $\mu$ phase diagrams

We start with the presentation of phase diagrams in the  $T$ - $\mu$  plane for fixed neutrino chemical potential. In Fig. 5.2 such phase diagrams are shown for two different neutrino chemical potentials ( $\mu_{Le} = 200$  and  $400$  MeV). These neutrino chemical potentials are expected to cover the range relevant for protoneutron stars. These phase diagrams should be compared with the one without neutrino trapping (corresponding

to  $\mu_{L_e} = 0$ ), Fig. 4.1.

The structure of the phase diagrams in Fig. 5.2 is similar to the structure of those presented in Chap. 4. The  $\chi$ SB phase at low chemical potentials is only little affected by a finite neutrino chemical potential. In both phase diagrams it is followed first by the 2SC phase and then by the (g)CFL phase. For  $\mu_{L_e} = 200$  MeV, we again find a slice of the uSC phase between the latter phases. The high temperature region is governed by the normal phase as before.

For a thorough examination of the influence of a finite neutrino chemical potential it is most instructive to inspect properties like charge chemical potentials and particle densities at  $T = 0$  more closely. The constituent quark masses, gap parameters, and charge chemical potentials are shown in Fig. 5.3 for  $\mu_{L_e} = 200$  MeV and in Fig. 5.4 for  $\mu_{L_e} = 400$  MeV. The quark and lepton densities are displayed in Fig. 5.5.

Starting with the influence of a neutrino chemical potential of 200 MeV, the first (starting from small chemical potentials) new feature compared to the findings of Chap. 4 is a nonzero positive  $\mu_Q$  ( $\mu_Q = 128$  MeV at  $\mu = 0$ ) in the  $\chi$ SB phase which is necessary because the finite neutrino chemical potential causes a finite electron density which has to be compensated by positively charged particles. For quark chemical potentials below 283 MeV there are no quarks in the system and the charge chemical potential is solely determined by the balance of negatively charged electrons with  $\mu_e = \mu_{L_e} - \mu_Q$  and positively charged anti-muons with  $\mu_{\mu^+} = -\mu_{\mu^-} = \mu_Q$  ( $\mu_{L_\mu} = 0$ ). At  $\mu = 0$  there is a small density of electrons and anti-muons of  $0.0016 \text{ fm}^{-3}$ . The amount of anti-muons equals the amount of electrons up to  $\mu = 283$  MeV. At this point, the chemical potential of the up quarks  $\mu_u = \mu + \frac{2}{3}\mu_Q$  with  $\mu_3 = \mu_8 = 0$  and  $\mu_Q = 127.6$  MeV reaches the up quark mass of  $M_u = 367.6$  MeV and leads to a small abundance of up quarks in the system which facilitates the neutrality of matter, and the electric charge chemical potential decreases with increasing  $\mu$ . For  $\mu > 303$  MeV, it drops below the muon mass and there are no anti-muons left in the  $\chi$ SB phase.

At  $\mu = 361.6$  MeV, the system undergoes a first-order phase transition to the 2SC phase. The chiral phase transition happens for a quark chemical potential which is approximately 6 MeV smaller than for vanishing neutrino chemical potential (cf. Sec. 4.1), and the system directly enters the 2SC phase even for small temperatures. This is a sign of the strengthened 2SC phase due to finite neutrino chemical potential, as discussed at the beginning of this chapter.

Fig. 5.5 shows the presence of a small amount of muons in most part of the 2SC phase which is correlated to the large negative charge chemical potential  $\mu_Q$ . The density of the muons follows the shape of  $\mu_Q$  (compare left panel of Fig. 5.5 with upper right panel of Fig. 5.3). At  $\mu = 415$  MeV the first strange quarks appear. Their fraction rises steeply until a first-order transition to the gCFL phase takes place at  $\mu = 464.2$  MeV. As a further sign of the strengthened 2SC phase, this transition happens at larger chemical potentials compared to the case with vanishing neutrino chemical potential.

For  $\mu_{L_e} = 400$  MeV (lower panel in Fig. 5.2), the 2SC phase occupies a much bigger

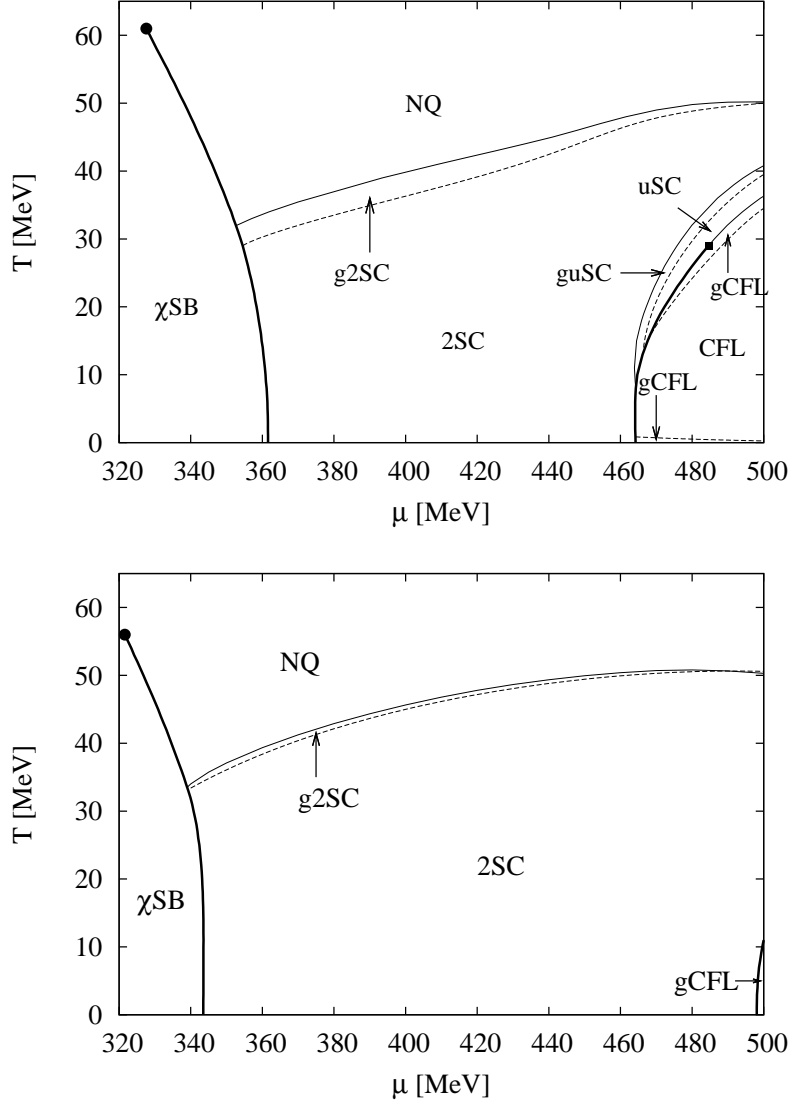


Figure 5.2: Phase diagrams of neutral quark matter at fixed lepton-number chemical potentials  $\mu_{L_e} = 200$  MeV (upper panel) and  $\mu_{L_e} = 400$  MeV (lower panel). Thick lines indicate first-order phase transitions and thin lines second-order transitions. The dashed lines indicate the (dis)appearance of gapless modes. (It is instructive to compare these phase diagrams with the one for  $\mu_{L_e} = 0$  shown in Fig. 4.1).

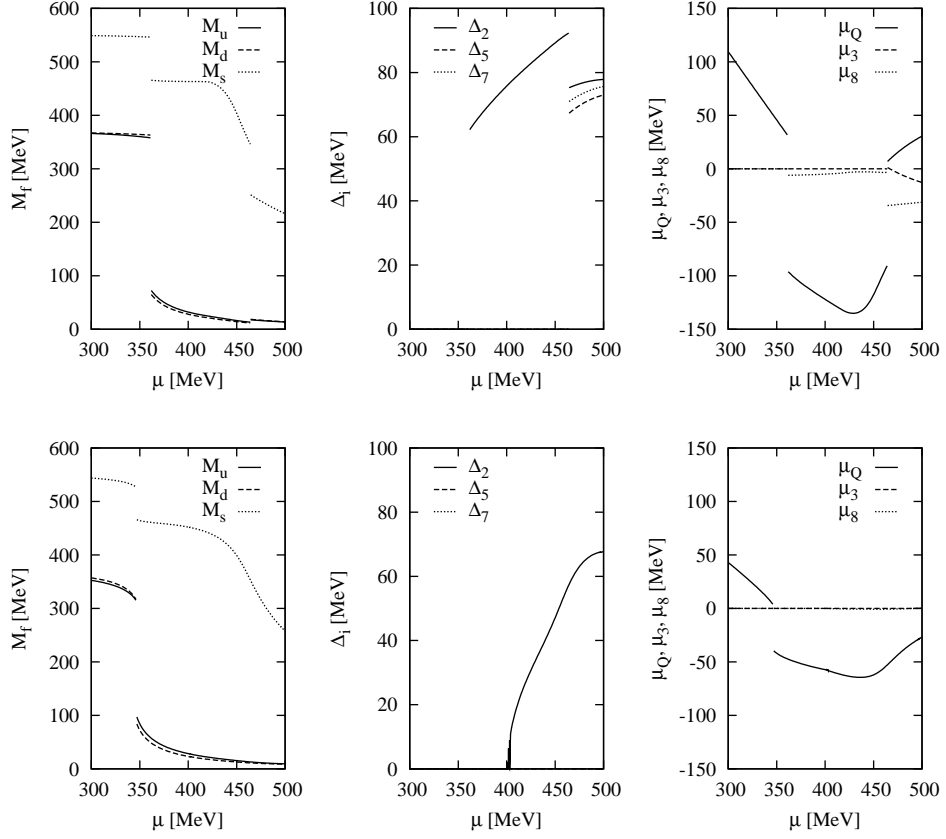


Figure 5.3: Quark masses, gap parameters, and electric and color charge chemical potentials as functions of the quark chemical potential for  $T = 0$  (upper panels) and  $T = 40$  MeV (lower panels) for  $\mu_{L_e} = 200$  MeV.

part of the phase diagram compared to the previously discussed case. It shifts the chiral phase transition by nearly 20 MeV to smaller chemical potentials and pushes the (g)CFL phase aside by more than 30 MeV in the  $\mu$ -direction.

Comparing the masses, gap parameters, charge chemical potentials, and particle densities at  $\mu_{L_e} = 400$  MeV (see Fig. 5.4 and right panel of Fig. 5.5) with those at  $\mu_{L_e} = 200$  MeV, the up and down-quark masses and densities exhibit a stronger splitting in the  $\chi$ SB phase for  $\mu_{L_e} = 400$  MeV which can again be explained by the large value of  $\mu_Q$ . As in the  $\mu_{L_e} = 200$  MeV case, we observe a balance of electrons and anti-muons in the  $\chi$ SB phase for chemical potentials below 226 MeV where the first up quarks are present in the system (compared to 283 MeV for  $\mu_{L_e} = 200$  MeV). Below  $\mu = 226$  MeV the electric charge chemical potential is  $\mu_Q = 214$  MeV (which is considerably higher than for the case with the lower neutrino chemical potential) and the electrons and anti-muons have particle densities of  $0.028 \text{ fm}^{-3}$  which is one order



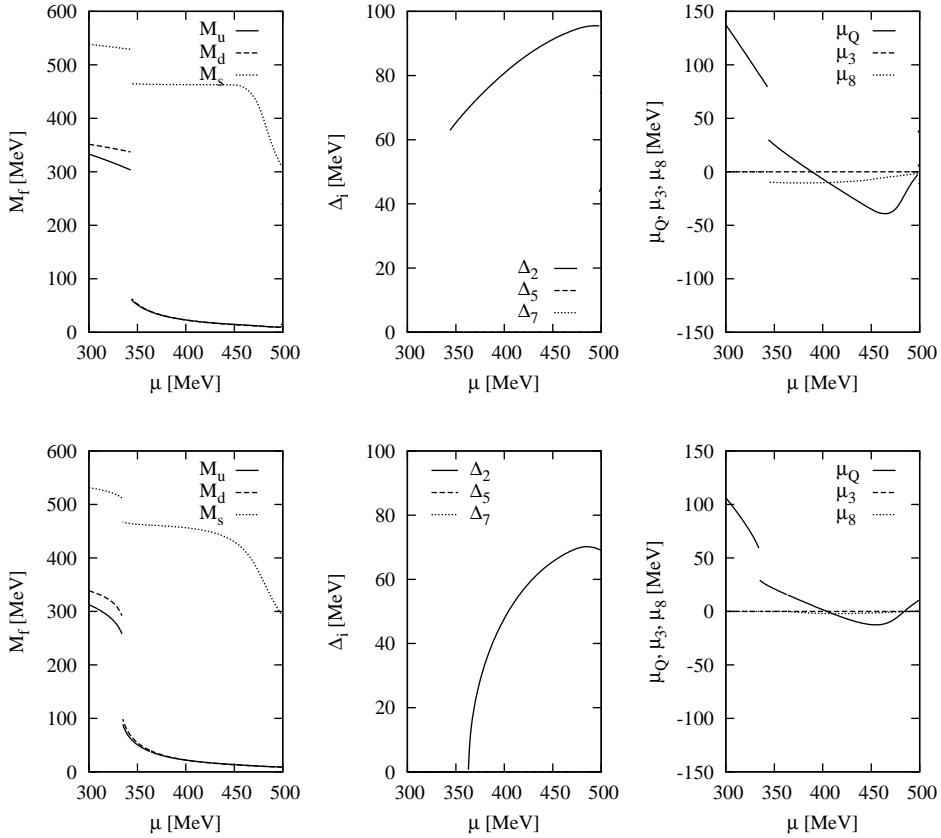


Figure 5.4: Quark masses, gap parameters, and electric and color charge chemical potentials as functions of the quark chemical potential for  $T = 0$  (upper panels) and  $T = 40$  MeV (lower panels) for  $\mu_{L_e} = 400$  MeV.

of magnitude larger than for  $\mu_{L_e} = 200$  MeV. However, the situation is qualitatively the same as for the lower neutrino chemical potential.

In the 2SC phase,  $\mu_Q$  is shifted upwards compared to  $\mu_{L_e} = 200$  MeV and is even positive for  $\mu < 389$  MeV for  $T = 0$ , and at  $T = 40$  MeV it is positive for  $\mu < 405$  MeV as well as for  $\mu > 484$  MeV. This reflects the fact that the neutrino chemical potential alone is large enough to generate an electron chemical potential  $\mu_e = \mu_{L_e} - \mu_Q$  which supplies enough electrons to compensate the positive charge of the quark content.

We should note that a schematic version of the  $T$ - $\mu$  phase diagram at  $\mu_{L_e} = 200$  MeV was first presented in Ref. [64] (right panel of Fig. 4 therein), obtained in the same model with a similar parameter set. If one ignores the presence of the uSC phase, which has not been considered in [64], the results of Ref. [64] are in agreement with our findings here.

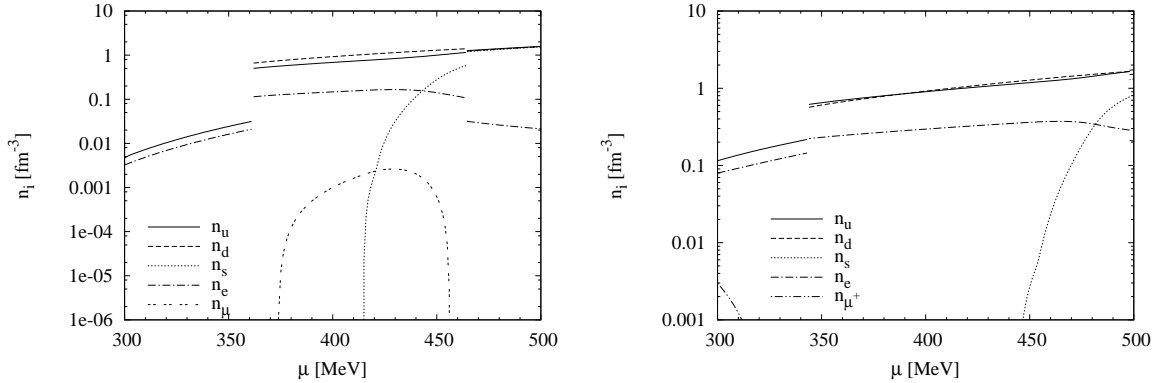


Figure 5.5: Number densities of quarks and leptons as functions of the quark chemical potential  $\mu$  at  $T = 0$  MeV for  $\mu_{L_e} = 200$  MeV (left panel) and  $\mu_{L_e} = 400$  MeV (right panel). Note: while the left panel shows the density of the muons, the right panel shows the density of the antimuons.

### 5.2.2 $T$ - $\mu_{L_e}$ phase diagrams

Next, we explore phase diagrams in the plane of temperature and neutrino chemical potential, keeping the quark chemical potential  $\mu$  fixed. The results are shown in Fig. 5.6. The upper panel corresponds to a quark chemical potential of 400 MeV which might be realized in the outer core of a protoneutron star. The lower panel shows the situation for a significantly higher quark chemical potential of 500 MeV corresponding to densities in the inner stellar core. The terms “inner stellar core” and “outer stellar core” should not be taken literally because the central densities of protoneutron stars are only poorly known. In our calculations we find densities in a range of  $\sim 3.5\rho_0$  for  $\mu = 400$  MeV and  $\sim 9\rho_0$  for  $\mu = 500$  MeV. These values are of the same order of magnitude as densities obtained in neutron star models in [79].

The phase diagram for  $\mu = 400$  MeV is dominated by the 2SC phase. In addition, there are two regions of the normal phase, one in the lower left corner of the phase diagram (low temperatures and low chemical potentials) and one for temperatures above 31 to 46 MeV (depending on the neutrino chemical potential).

Comparing this phase diagram with the one for  $\mu = 500$  MeV, we hardly find any resemblance. For this “inner core” case, the phase diagram is dominated by the (g)CFL phase, which is stable up to  $T \approx 38$  MeV at vanishing neutrino chemical potential. In temperature direction it is followed by a thin slice of the uSC phase and afterwards by the 2SC phase at  $T \approx 44$  MeV, which extends from  $T \approx 11$  MeV to  $T \approx 50$  MeV at  $\mu_{L_e} = 400$  MeV. For temperatures above  $\sim 50$  MeV, the system stays in the normal phase.

To understand the connection between the two phase diagrams, it is useful to look

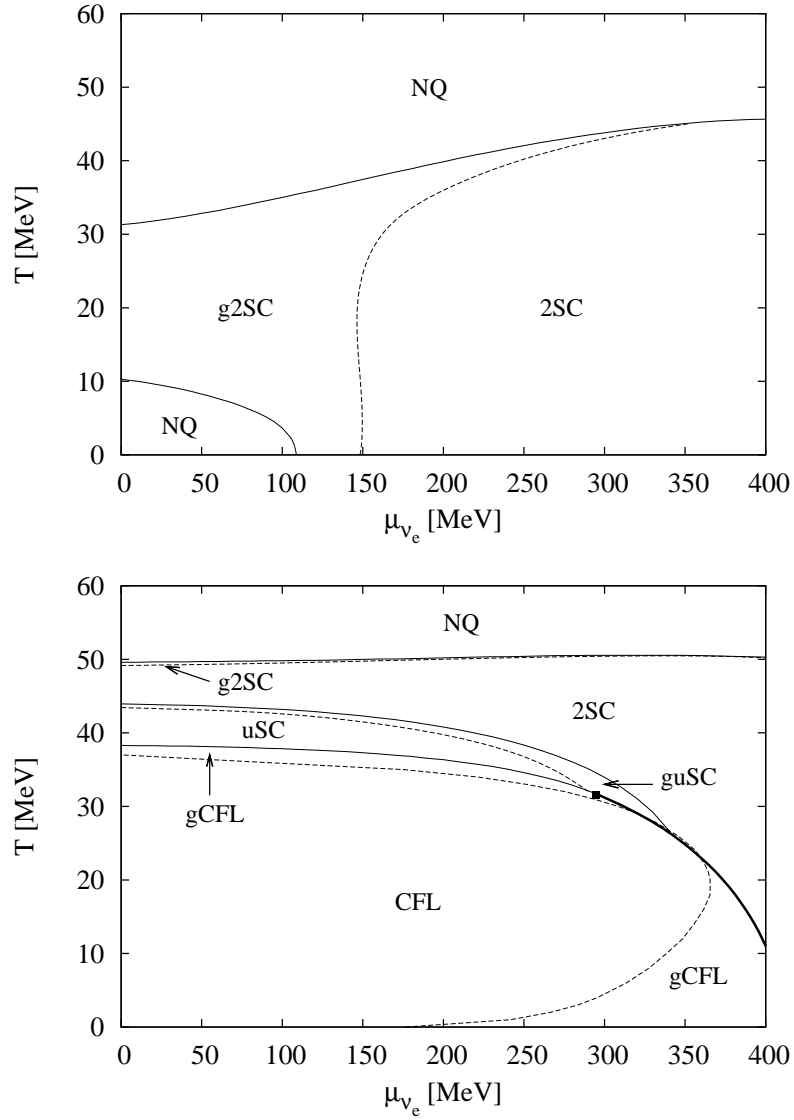


Figure 5.6: The phase diagrams of neutral quark matter in the plane of temperature and electron lepton-number chemical potential at two fixed values of the quark chemical potential:  $\mu = 400$  MeV (upper panel) and  $\mu = 500$  MeV (lower panel). The dashed lines indicate the (dis)appearance of gapless modes.

at the three-dimensional diagram presented in Fig. 5.1. The  $\mu = 500$  MeV case is the right hand side border of the 3D diagram and the  $\mu = 400$  MeV case is a parallel cut through the middle of the phase diagram. It can be seen how the (g)CFL phase becomes smaller with decreasing chemical potential  $\mu$  and then vanishes completely. In addition, one can find the NQ phase for small temperatures and small neutrino chemical potentials (cf. Fig. 4.1 as well).

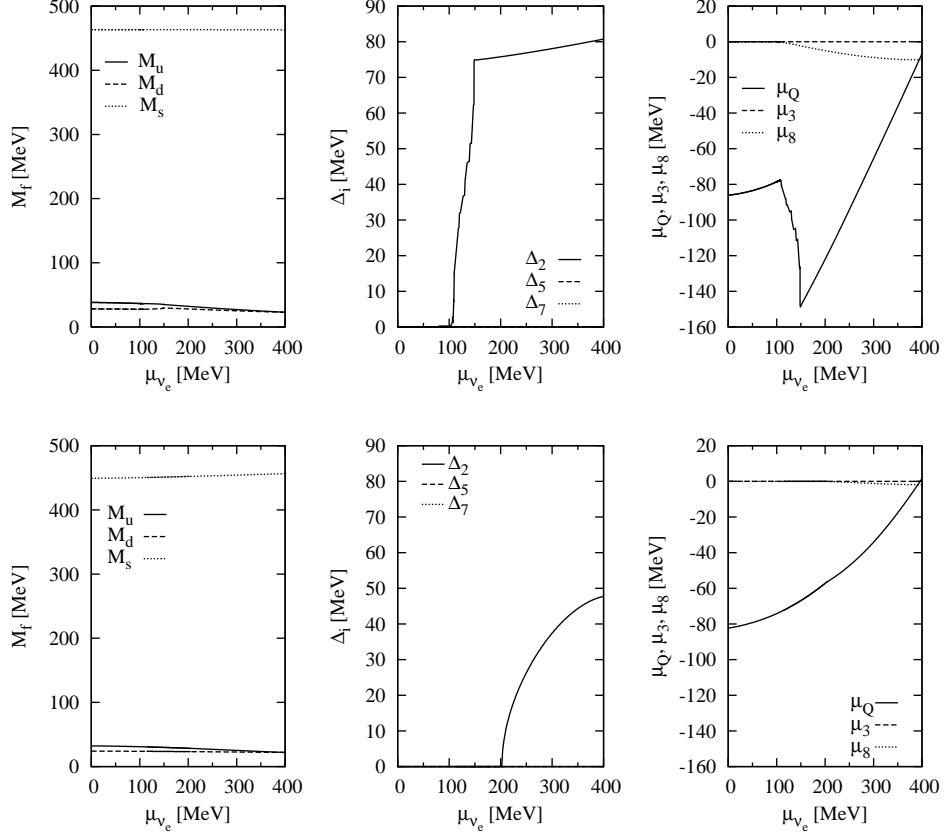


Figure 5.7: Quark masses, gap parameters, and electric and color charge chemical potentials as functions of the quark chemical potential for  $T = 0$  (upper panels) and  $T = 40$  MeV (lower panels) for  $\mu = 400$  MeV.

In Fig. 5.7 the quark masses, gap parameters, and charge chemical potentials for  $\mu = 400$  MeV are shown. The upper panels display the properties at  $T = 0$ . For small neutrino chemical potentials the system stays in the normal phase. At  $\mu_{L_e} = 109$  MeV a second order phase transition to the gapless 2SC phase takes place where the gap parameter  $\Delta_2$  rises steeply. At  $\mu_{L_e} = 148$  MeV the system reaches the regular 2SC phase. The interval of the g2SC phase is numerically very delicate as can be seen in the figure. After entering the 2SC phase,  $\Delta_2$  only grows slowly.

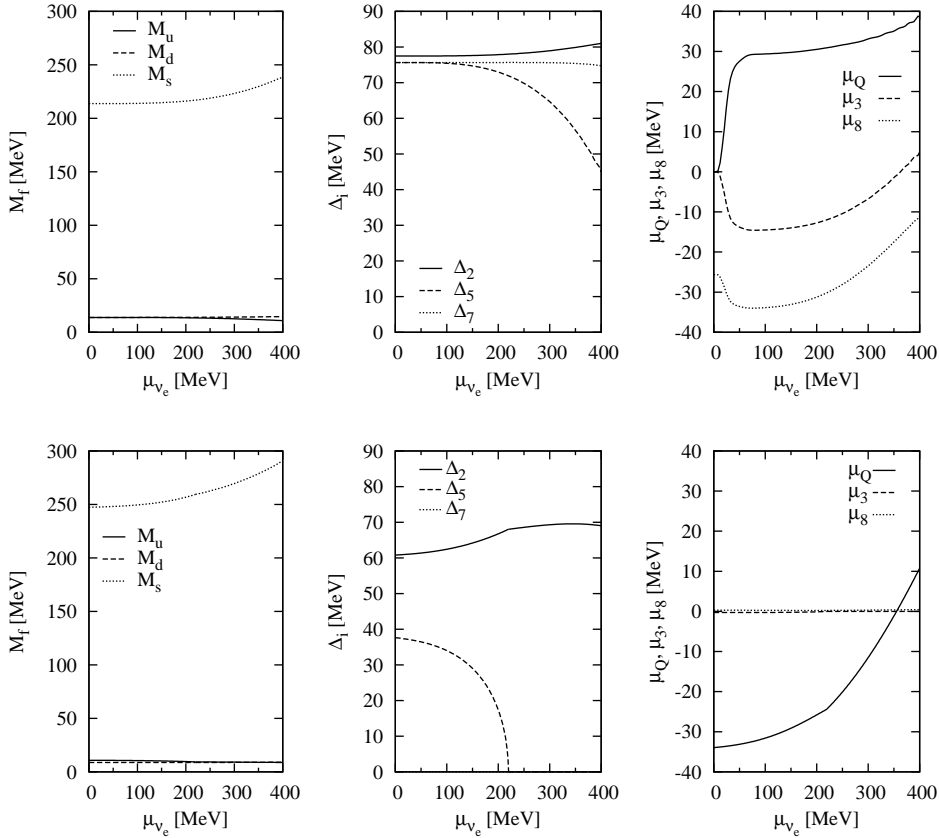


Figure 5.8: Quark masses, gap parameters, and electric and color charge chemical potentials as functions of the quark chemical potential for  $T = 0$  (upper panels) and  $T = 40$  MeV (lower panels) for  $\mu = 500$  MeV.

The charge chemical potential  $\mu_Q$  (right panel) has an interesting shape: starting the discussion at large neutrino chemical potentials,  $\mu_Q$  decreases (to larger negative values) with decreasing  $\mu_{L_e}$ , which is expected when thinking of the electron chemical potential  $\mu_e = \mu_{L_e} - \mu_Q$ . However, at  $\mu_{L_e} = 148$  MeV, when the system enters the g2SC phase, the absolute value of the electric charge chemical potential decreases as the neutrino chemical potential is decreased. In that region, electric neutrality is increasingly achieved by an excess of down quarks over up quarks and to a minor extent by electrons (see left panels of Figs. 5.9 and 5.10).

The lower panel of Fig. 5.7 displays the properties at  $\mu = 400$  MeV and  $T = 40$  MeV. For small chemical potentials the system stays in the normal phase and enters the 2SC phase at  $\mu_{L_e} = 200$  MeV, signaled by the non-vanishing and growing  $\Delta_2$ . Starting at large neutrino chemical potentials again, the electric charge chemical potential  $\mu_Q$  decreases (increasing absolute value of a negative charge chemical potential) with

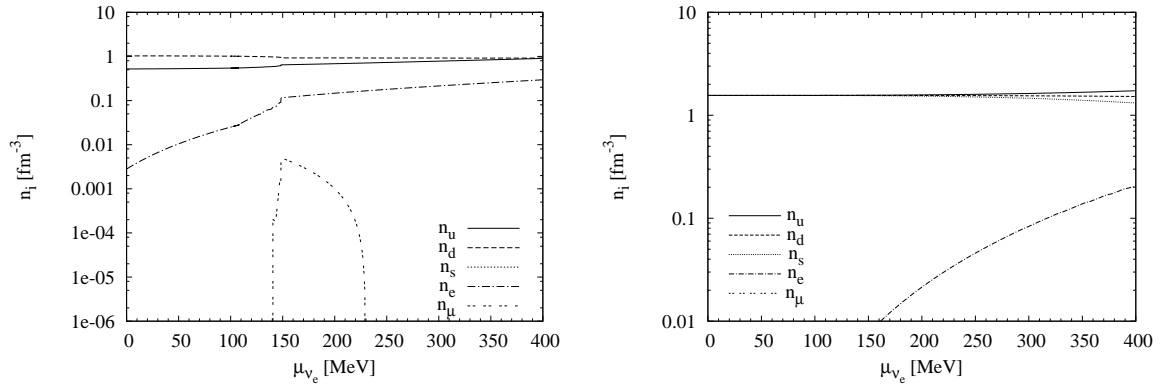


Figure 5.9: Number densities of quarks and leptons as functions of the quark chemical potential  $\mu$  at  $T = 0$  MeV for  $\mu = 400$  MeV (left panel) and  $\mu = 500$  MeV (right panel).

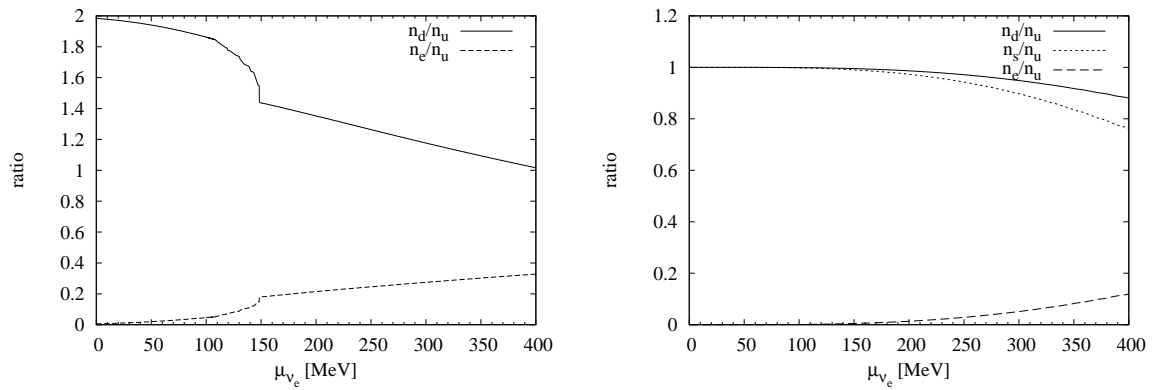


Figure 5.10: Ratios of number densities at  $T = 0$  MeV for  $\mu = 400$  MeV (left panel) and  $\mu = 500$  MeV (right panel).

decreasing neutrino chemical potential, as expected from the previous discussion.

The quark masses, gap parameters, and charge chemical potentials for  $\mu = 500$  MeV are presented in Fig. 5.8. For  $T = 0$  the system stays in the (g)CFL phase over the whole range of neutrino chemical potentials. Looking at the gap parameters, it is striking that  $\Delta_5$  is decreasing while  $\Delta_7$  stays nearly constant and  $\Delta_2$  is rising. This behavior suggests a transition to the dSC phase for larger neutrino chemical potentials.

The right panel of Fig. 5.9 illustrates how the quark densities drift apart for larger chemical potentials where electrons are present. The same is visible in the right panel of Fig. 5.10 where the ratios of the number densities of the quark species and the ratio of electron density versus up quark density are displayed. In the last figure it can be clearly seen that the density of the up quarks exceeds the densities of down and strange quarks with increasing neutrino chemical potential.

Before concluding this section, we mention that a similar phase diagram was presented in [64] (left panel of Fig. 4 therein) for  $\mu = 460$  MeV. Therefore, we cannot directly compare it to our results. Qualitatively, however, it resembles our  $\mu = 500$  MeV case and it is compatible with our three-dimensional phase diagram.

### 5.2.3 Lepton fraction

In our calculations we used the neutrino chemical potential  $\mu_{L_e}$  as a free parameter. It is now natural to ask to which lepton fraction  $Y_{L_e}$  these chemical potentials lead. The lepton fractions are shown in Fig. 5.11 for  $\mu_{L_e} = 200$  (thick lines) and 400 MeV (thin lines), each for  $T = 0, 20,$  and 40 MeV as functions of the quark chemical potential  $\mu$ . The thin horizontal line marks  $Y_{L_e} = 0.4$ , i.e., the value expected at the center of a protoneutron star right after its creation.

To achieve a lepton fraction of 0.4, a lepton-number chemical potential in the range somewhere between 200 and 400 MeV is necessary for  $\mu \lesssim 480$  MeV. For higher chemical potentials, which are probably achieved in the center of a protoneutron star, even larger lepton-number chemical potentials are required. With increasing quark chemical potential  $\mu$ , a larger  $\mu_{L_e}$  is required.

It is difficult to achieve a large lepton fraction in the CFL phase. For  $\mu_{L_e} = 200$  MeV the lepton fractions in the CFL phase are smaller than 0.05. For  $\mu_{L_e} = 400$  MeV a lepton fraction of 0.23 is achieved in the gapless CFL phase.

We deduce that it is unlikely to find a CFL phase in the early stages of the protoneutron star evolution where the lepton fraction should equal 0.4.

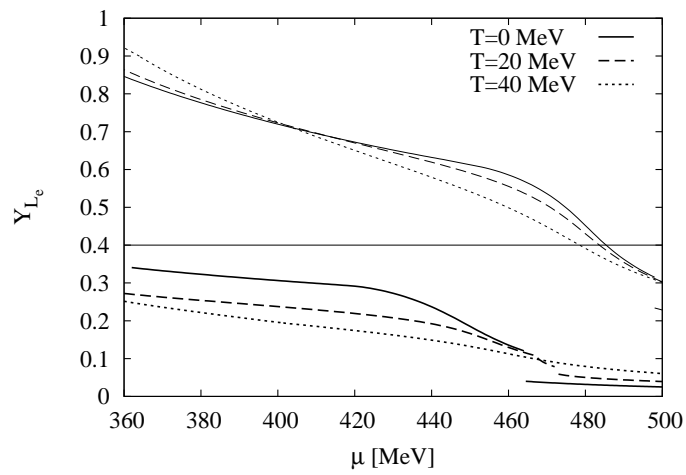


Figure 5.11: Dependence of the electron lepton fraction  $Y_{L_e}$  on the quark chemical potential for  $\mu_{L_e} = 200$  MeV (thick lines) and  $\mu_{L_e} = 400$  MeV (thin lines) at three fixed temperatures,  $T = 0$  MeV (solid lines),  $T = 20$  MeV (dashed lines), and  $T = 40$  MeV (dotted lines).



## 6 Pseudoscalar bosons in the color-flavor locked phase

In the previous chapters, we have computed phase diagrams of dense, locally neutral quark matter under different conditions, finding several kinds of color-superconducting phases. In the remainder of this thesis, we will concentrate on the color-flavor locked phase which is the ground state of matter at highest densities. Recent Dyson-Schwinger studies actually indicate that the CFL phase might be the preferred phase all the way down to the hadronic phase [80].

In the CFL phase, the original  $SU(3)_{\text{color}} \times SU(3)_L \times SU(3)_R \times U(1)_V$  symmetry of three-flavor QCD in the chiral limit is broken down to  $SU(3)_{\text{color}+V} \times Z_2$  by the diquark condensates. The spontaneous breaking of baryon number symmetry leads to the emergence of one scalar Goldstone boson, while the spontaneous breaking of chiral symmetry results in the emergence of eight pseudoscalar Goldstone bosons. These Goldstone bosons are massless in the chiral limit. For nonzero quark masses, the pseudoscalar Goldstone bosons acquire masses. However, the scalar Goldstone boson related to baryon number remains massless because baryon number is an exact symmetry even for massive quarks. This Goldstone boson will not be discussed in this thesis. A ninth pseudoscalar Goldstone boson appears due to the spontaneous breaking of  $U(1)_A$  symmetry, which is a symmetry of QCD at high density [81, 82].

For energies much smaller than the superconducting gap, the Goldstone bosons can be described by the so-called low-energy effective theory (LEET) [83]. Using this theory in the weak-coupling limit, meson masses and decay constants have been studied [84, 63, 62, 85]. It was shown that the stress imposed by the strange quark mass may lead to kaon condensation [63, 62].

At moderate densities, where the weak-coupling assumption is not justified, kaon condensation for non-zero strange quark mass has been analyzed in the NJL model [15, 16, 17]. In these studies the Goldstone bosons have not been constructed explicitly. So far, an explicit construction of the Goldstone bosons has only been carried out in the chiral limit [18, 19].

In the following, we will construct the Goldstone bosons explicitly by solving the Bethe-Salpeter equation for quark-quark scattering in random phase approximation. In the CFL phase, the Goldstone bosons are in fact superpositions of diquark and di-hole states, rather than quark-antiquark states as in the vacuum. Since they have the same quantum numbers as the pseudoscalar Goldstone bosons in vacuum, we will use the names of the vacuum meson states also for the Goldstone bosons in the CFL

phase as no confusion is possible.

In the present and the following chapter, we will calculate meson masses and decay constants and compare our results with those derived in the weak-coupling limit of the LEET. The leading order results of the LEET are universal in the sense that they should hold in the weak-coupling limit of any model exhibiting the same symmetries. Therefore, we can on the one hand check our results for very small couplings, and on the other hand see whether one should expect large deviations from the weak-coupling results if the diquark coupling is increased.

For equal quark masses, the nine pseudoscalar Goldstone bosons form an octet and a singlet. The bosons of the octet, which arise due to spontaneous chiral symmetry breaking, are still connected by the unbroken  $SU(3)_{c+V}$  symmetry, and are therefore degenerate. In contrast, there is no residual symmetry relating the Goldstone boson of the axial  $U(1)_A$  breaking to the octet.

## 6.1 Summary of effective theory results

The aim of formulating an effective theory for the low-energy degrees of freedom is to express the respective quantities in terms of only a few parameters. In the CFL phase, the low-energy effective theory (LEET) describes the Goldstone bosons for energies much smaller than the superconducting gap. The Lagrangian of the LEET is obtained by writing down the most general Lagrangian compatible with the symmetries of the CFL phase in terms of the light degrees of freedom [83].

Since we will compare our model results with those derived in the LEET, we briefly summarize the latter:

In [63, 84, 62] the pion and kaon masses

$$\begin{aligned} m_{\pi^\pm}^2 &= \frac{4A}{f_\pi^2}(m_u + m_d)m_s, \\ m_{K^\pm}^2 &= \frac{4A}{f_\pi^2}(m_u + m_s)m_d, \\ m_{K^0, \bar{K}^0}^2 &= \frac{4A}{f_\pi^2}(m_d + m_s)m_u \end{aligned} \tag{6.1}$$

have been calculated. These formulas imply an inverse mass ordering [84] compared to the vacuum, with the kaons being lighter than the pions. For degenerate up and down quarks with mass  $m_q$ , the pion mass is proportional to  $2m_q m_s$ , while the kaon mass is proportional to  $(m_q m_s + m_q^2)$ .

For later comparison, we also list the result for equal quark masses  $m_q$ , where pions (including the  $\pi^0$ ), kaons and the  $\eta$  meson are degenerate and have the mass

$$m_{\text{octet}}^2 = \frac{8A}{f_\pi^2} m_q^2. \tag{6.2}$$

The meson chemical potentials

$$\begin{aligned}
 \mu_{\pi^\pm} &= \mp \frac{m_d^2 - m_u^2}{2\mu}, \\
 \mu_{K^\pm} &= \mp \frac{m_s^2 - m_u^2}{2\mu}, \\
 \mu_{K^0, \bar{K}^0} &= \mp \frac{m_s^2 - m_d^2}{2\mu}
 \end{aligned} \tag{6.3}$$

have also been calculated in [63, 84, 62]. In the presence of a charge chemical potential  $\mu_Q$ , this has to be added to the meson chemical potentials according to the charge content of the mesons.

The meson chemical potentials presented in Eq. (6.3) arise due to mass differences of the quarks and can be interpreted as the differences of the Fermi momenta of the participating quarks:

$$p_F = \sqrt{\mu^2 - m_i^2} \approx \mu - \frac{m_i^2}{2\mu}. \tag{6.4}$$

In the hidden-flavor sector ( $\pi^0$ ,  $\eta$ , and  $\eta'$ ), the situation is more complicated. For unequal quark masses the three states are mixed. For simplicity, we will directly apply  $m_u = m_d \equiv m_q$ , which we will use throughout all our calculations. For equal up and down quark masses the  $\pi^0$  decouples from the other two hidden-flavor mesons and is degenerate with the charged pions. To obtain the mass eigenstates  $\eta$  and  $\eta'$ , we have to diagonalize the mass matrix

$$\hat{M}^2 = \begin{pmatrix} m_{\eta_0}^2 & m_{mix}^2 \\ m_{mix}^2 & m_{\eta_8}^2 \end{pmatrix}, \tag{6.5}$$

where the masses of the symmetry eigenstates are

$$m_{\eta_0}^2 = \frac{8A}{3f_{\eta'}^2} m_q (2m_s + m_q), \quad m_{\eta_8}^2 = \frac{8A}{3f_\pi^2} m_q (m_s + 2m_q), \tag{6.6}$$

and

$$m_{mix}^2 = \frac{8\sqrt{2}A}{3f_{\eta'} f_\pi} m_q (m_s - m_q) \tag{6.7}$$

describes the mixing of the states [85]. For the mass eigenvalues of the physical states we obtain

$$\begin{aligned}
 m_\eta^2 &= \frac{4A}{3f_{\eta'}^2 f_\pi^2} \left( f_{\eta'}^2 m_q (2m_q + m_s) + f_\pi^2 m_q (m_q + 2m_s) \right. \\
 &\quad \left. + m_q \sqrt{-36f_{\eta'}^2 f_\pi^2 m_q m_s + (f_{\eta'}^2 (2m_q + m_s) + f_\pi^2 (m_q + 2m_s))^2} \right)
 \end{aligned} \tag{6.8}$$

and

$$m_{\eta'}^2 = \frac{4A}{3f_{\eta'}^2 f_{\pi}^2} \left( f_{\eta'}^2 m_q (2m_q + m_s) + f_{\pi}^2 m_q (m_q + 2m_s) - m_q \sqrt{-36f_{\eta'}^2 f_{\pi}^2 m_q m_s + (f_{\eta'}^2 (2m_q + m_s) + f_{\pi}^2 (m_q + 2m_s))^2} \right). \quad (6.9)$$

Taking the equal mass limit again, the  $\eta$  belongs to the octet, Eq. (6.2), and the  $\eta'$  mass simplifies to

$$m_{\eta'}^2 = \frac{8A}{f_{\eta'}^2} m_q^2. \quad (6.10)$$

The formulas for the masses still contain the low-energy constants  $A$ ,  $f_{\pi}$ , and  $f_{\eta'}$ . Due to asymptotic freedom, QCD is a weakly coupled theory at small distances, i. e., high densities. This allows the calculation of the parameters in the weak-coupling limit by using high-density effective theory (HDET). Otherwise the parameters would have to be determined by experiment which is not feasible at such high densities. The decay constants are given by [84]

$$f_{\pi}^2 = \frac{21 - 8 \ln 2}{18} \frac{\mu^2}{2\pi^2}, \quad (6.11)$$

$$f_{\eta'}^2 = \frac{3}{4} \left( \frac{\mu^2}{2\pi^2} \right). \quad (6.12)$$

These leading order results do not depend on the gap parameter  $\Delta$  and are independent of the specific form of the interaction. The factor  $A$  is determined as [84]

$$A = \frac{3\Delta^2}{4\pi^2}, \quad (6.13)$$

with the gap parameter  $\Delta$ .

## 6.2 Nambu–Jona-Lasinio model

### 6.2.1 Lagrangian

As in the first part of this thesis, we will conduct our studies in the Nambu–Jona-Lasinio model. For simplicity, however, we will neglect the quark-antiquark interactions  $\mathcal{L}_{\bar{q}q}$  (including the 't Hooft term), Eq. (3.2). The Lagrangian is then given by

$$\mathcal{L} = \bar{q}(i\partial - \hat{m})q + \mathcal{L}_{qq} \quad (6.14)$$

with  $q$  again describing a quark field with three flavor and three color degrees of freedom. The mass matrix contains the bare quark masses,  $\hat{m} = \text{diag}_f(m_u, m_d, m_s)$ .

Since we neglect the quark-antiquark interactions, no additional terms appear which could contribute to constituent quark masses.

$$\mathcal{L}_{qq} = H \sum_{A,A'=2,5,7} [(\bar{q}i\gamma_5\tau_A\lambda_{A'}C\bar{q}^T)(q^TCi\gamma_5\tau_A\lambda_{A'}q) + (\bar{q}\tau_A\lambda_{A'}C\bar{q}^T)(q^TC\tau_A\lambda_{A'}q)] \quad (6.15)$$

describes the  $SU(3)_{\text{color}} \times SU(3)_L \times SU(3)_R \times U(1)_V \times U(1)_A$  symmetric diquark interaction already defined in Eq. (3.3). The first term of  $\mathcal{L}_{qq}$  corresponds to the scalar quark-quark interaction in the flavor and color antitriplet channel. This interaction gives rise to the diquark condensates  $s_{AA} = \langle q^TC\gamma_5\tau_A\lambda_A \rangle$  (cf. Eq. (3.9)). The second term is the corresponding pseudoscalar interaction which is required by chiral symmetry. It is essential for the following study of the pseudoscalar mesonic excitations.

Using Nambu-Gorkov bispinors, Eq. (6.15) can be rewritten as

$$\mathcal{L}_{qq} = 4H \sum_{A,A'=2,5,7} \left\{ (\bar{\Psi}\Gamma_{AA'}^{s\uparrow}\Psi)(\bar{\Psi}\Gamma_{AA'}^{s\downarrow}\Psi) + (\bar{\Psi}\Gamma_{AA'}^{p\uparrow}\Psi)(\bar{\Psi}\Gamma_{AA'}^{p\downarrow}\Psi) \right\}, \quad (6.16)$$

with 18 scalar operators

$$\Gamma_{AA'}^{s\uparrow} = \begin{pmatrix} 0 & i\gamma_5\tau_A\lambda_{A'} \\ 0 & 0 \end{pmatrix}, \quad \Gamma_{AA'}^{s\downarrow} = \begin{pmatrix} 0 & 0 \\ i\gamma_5\tau_A\lambda_{A'} & 0 \end{pmatrix} \quad (6.17)$$

and 18 pseudoscalar operators

$$\Gamma_{AA'}^{p\uparrow} = \begin{pmatrix} 0 & \tau_A\lambda_{A'} \\ 0 & 0 \end{pmatrix}, \quad \Gamma_{AA'}^{p\downarrow} = \begin{pmatrix} 0 & 0 \\ \tau_A\lambda_{A'} & 0 \end{pmatrix}. \quad (6.18)$$

For later convenience, we define

$$\bar{\Gamma}_i = \gamma^0\Gamma_i^\dagger\gamma^0. \quad (6.19)$$

Vertices describing the coupling of an external source to a bare quark are generalized to Nambu-Gorkov space in the following way:

$$\hat{\Gamma} \rightarrow (\hat{\Gamma})_{NG} \equiv \begin{pmatrix} \hat{\Gamma} & 0 \\ 0 & -C\hat{\Gamma}^TC \end{pmatrix}. \quad (6.20)$$

This definition guarantees that quark-antiquark bilinears remain unchanged:

$$\bar{\Psi}(\hat{\Gamma})_{NG}\Psi = \bar{q}\hat{\Gamma}q. \quad (6.21)$$

## 6.2.2 Ground state

Before we can construct the mesonic excitations, we have to determine the CFL ground state. Just like in the previous chapters, we only want to consider neutral matter here.

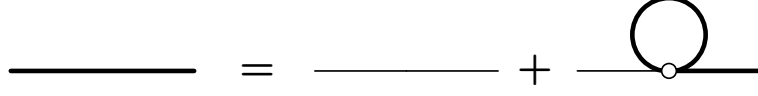


Figure 6.1: Dyson equation for the dressed Nambu-Gorkov propagator (thick line). The thin line corresponds to the bare propagator.

It would be possible to calculate the gap parameters and the chemical potentials by applying the methods presented in Chapter 3. However, we found that this procedure is numerically not accurate enough for the subsequent calculation of the properties of the mesons, which turn out to be very sensitive to the values of the gap parameters and chemical potentials. Therefore, we use the Dyson equation (see Fig. 6.1) to calculate these quantities. Both procedures are formally equivalent and in principle yield the same results except for numerical differences.

The Dyson equation reads

$$S(p) = S_0(p) + S_0(p)\hat{\Sigma}S(p), \quad (6.22)$$

with the dressed quark propagator  $S(p)$ , the bare quark propagator  $S_0(p)$  and the self-energy  $\hat{\Sigma}$ . Solving for the self-energy, leads to

$$\hat{\Sigma} = S_0^{-1}(p) - S^{-1}(p), \quad (6.23)$$

where the inverse bare propagator is given by

$$S_0^{-1} = \begin{pmatrix} \not{p} + \hat{\mu}\gamma^0 - \hat{m} & 0 \\ 0 & \not{p} - \hat{\mu}\gamma^0 - \hat{m} \end{pmatrix} \quad (6.24)$$

and the inverse dressed propagator is defined by

$$S^{-1} = \begin{pmatrix} \not{p} + \hat{\mu}\gamma^0 - \hat{m} & \sum_{A=2,5,7} \Delta_A \gamma_5 \tau_A \lambda_A \\ -\sum_{A=2,5,7} \Delta_A^* \gamma_5 \tau_A \lambda_A & \not{p} - \hat{\mu}\gamma^0 - \hat{m} \end{pmatrix}. \quad (6.25)$$

The only difference between this inverse propagator and the one used in the previous chapters (cf. Eq. (3.25)) is that Eq. (6.25) only contains the bare quark masses instead of the constituent ones. Inserting the inverse propagators into Eq. (6.23) yields

$$\hat{\Sigma} = \begin{pmatrix} 0 & -\sum_{A=2,5,7} \Delta_A \gamma_5 \tau_A \lambda_A \\ \sum_{A=2,5,7} \Delta_A^* \gamma_5 \tau_A \lambda_A & 0 \end{pmatrix} \quad (6.26)$$

for the self energy. On the other hand,  $\hat{\Sigma}$  can be calculated by directly evaluating the quark loop in Fig. 6.1,

$$\hat{\Sigma} = 4iH \Gamma_i \int \frac{d^4 p}{(2\pi)^4} \frac{1}{2} \text{Tr} [\bar{\Gamma}_i S(p)] \quad (6.27)$$

with the operators  $\Gamma_i$  defined in Eqs. (6.17) and (6.18). Comparing the two expressions for  $\hat{\Sigma}$ , we can read off the gap equations

$$\Delta_A = 4H \int \frac{d^4 p}{(2\pi)^4} \frac{1}{2} \text{Tr} \left[ \Gamma_{AA}^{s\downarrow} S(p) \right]. \quad (6.28)$$

Note that the same expression is obtained by carrying out  $\frac{\partial \Omega}{\partial \Delta_A^*} = 0$ . The equality of Eqs. (6.26) and (6.27) further implies that contributions of scalar vertices with  $A \neq A'$  and all contributions of the pseudoscalar vertices have to vanish.

Diagonalizing  $S$  by a unitary transformation  $U$  as described in Appendix B.1, and performing a cyclic permutation under the trace leads to

$$\Delta_A = 4H \int \frac{d^4 p}{(2\pi)^4} \frac{1}{2} \text{Tr} \left[ \underbrace{U^\dagger \gamma_0 \Gamma_{AA}^{s\downarrow} U}_{:=\tilde{\Gamma}} S_{\text{diag}}(p) \right]. \quad (6.29)$$

$\tilde{\Gamma}$  describes the vertex emerging when the transformation matrices act on the original vertex and

$$S_{\text{diag}}(p) = \begin{pmatrix} \frac{1}{p_0 - \varepsilon_1(\vec{p})} & & \\ & \ddots & \\ & & \frac{1}{p_0 - \varepsilon_{72}(\vec{p})} \end{pmatrix}. \quad (6.30)$$

Next, we apply the Matsubara formalism and replace the four-momentum by

$$p \rightarrow \begin{pmatrix} i\omega_m \\ \vec{p} \end{pmatrix}, \quad (6.31)$$

with the fermionic Matsubara frequencies  $i\omega_n = (2n + 1)\pi T$ , and the integral over four-momentum by

$$i \int \frac{d^4 p}{(2\pi)^4} \longrightarrow -T \sum_n \int \frac{d^3 p}{(2\pi)^3}. \quad (6.32)$$

The gap equations then become

$$\Delta_A = -2iHT \int \frac{d^3 p}{(2\pi)^3} \sum_n \sum_{k=1}^{72} (\tilde{\Gamma})_{kk} \frac{1}{i\omega_n - \varepsilon_k(\vec{p})}. \quad (6.33)$$

Using the residue theorem allows us to transform the sum over  $n$  into a circular integral around the poles on the imaginary axis:

$$\Delta_A = 2iH \int \frac{d^3 p}{(2\pi)^3} \left( -\frac{i}{2\pi} \right) \oint dz \sum_{k=1}^{72} (\tilde{\Gamma})_{kk} \frac{1}{z - \varepsilon_k(\vec{p})} \left( \exp\left(\frac{z}{T}\right) + 1 \right)^{-1}. \quad (6.34)$$

Bending the contour around the poles on the real axis and applying the residue theorem again leads to

$$\Delta_A = -i \frac{H}{\pi^2} \int dp p^2 \sum_{k=1}^{72} (\tilde{\Gamma})_{kk} \left( \exp \left( \frac{\varepsilon_k(\vec{p})}{T} \right) + 1 \right)^{-1}. \quad (6.35)$$

This momentum integral can be calculated with a three-momentum cutoff  $\Lambda$ , as in the previous chapters. In the limit of zero temperature, we obtain

$$\Delta_A = -i \frac{H}{\pi^2} \int dp p^2 \sum_{k=1}^{72} (\tilde{\Gamma})_{kk} \theta(-\varepsilon_k(\vec{p})). \quad (6.36)$$

Using the fact that each eigenvalue  $\varepsilon_i(\vec{p})$  is twofold degenerate, and that for each positive eigenvalue there exists a negative one with the same absolute value, the number of summands can be reduced to 18:

$$\Delta_A = -i \frac{2H}{\pi^2} \int dp p^2 \sum_{k=1}^{18} (\tilde{\Gamma})_{kk} \theta(-\varepsilon_k(\vec{p})). \quad (6.37)$$

We will calculate the color neutrality conditions in a similar manner as the gap equations by setting the derivative of  $\Omega$  with respect to  $\mu_a$  to zero,

$$n_a = -\frac{\partial \Omega}{\partial \mu_a} = -i \int \frac{d^4 p}{(2\pi)^4} \frac{1}{2} \text{Tr} [\Gamma_a^0 S(p)] \stackrel{!}{=} 0 \quad (6.38)$$

with the thermodynamic potential

$$\Omega = -T \sum_n \int \frac{d^3 p}{(2\pi)^3} \frac{1}{2} \text{Tr} \ln \left( \frac{1}{T} S^{-1}(i\omega_n, \vec{p}) \right) + \frac{1}{4H} \sum_{A=2,5,7} |\Delta_A|^2, \quad (6.39)$$

and

$$\Gamma_a^0 = \frac{\partial S^{-1}}{\partial \mu_a} = \begin{pmatrix} \gamma^0 \lambda_a & 0 \\ 0 & -\gamma^0 \lambda_a^T \end{pmatrix}. \quad (6.40)$$

With this assignment it is possible to check all densities  $n_a$  ( $a = 1, \dots, 8$ ) which is, however, not necessary in the CFL phase [86]. Eq. (6.38) can be evaluated analogously to the gap equation, Eq. (6.28), and finally yields

$$n_a = \frac{1}{\pi^2} \int dp p^2 \sum_{k=1}^{18} (\tilde{\Gamma}_a^0)_{kk} \left( \exp \left( \frac{\varepsilon_k}{T} \right) + 1 \right)^{-1} \quad (6.41)$$

with the zero-temperature limit

$$n_a = \frac{1}{\pi^2} \int dp p^2 \sum_{k=1}^{18} (\tilde{\Gamma}_a^0)_{kk} \theta(-\varepsilon_k(\vec{p})). \quad (6.42)$$



## 6.3 Mesonic excitations

### 6.3.1 Axial transformations

In the chiral limit,  $m_u = m_d = m_s = 0$ , the Lagrangian (6.14) is invariant under  $SU(3)_{\text{color}} \times SU(3)_V \times SU(3)_A \times U(1)_V \times U(1)_A$  transformations. In the CFL phase, this symmetry is spontaneously broken down to  $SU(3)_{\text{color}+V} \times Z_2 \times Z_2$  by the condensates  $s_{AA}$ , Eq. (3.9). Axial flavor transformations

$$q \rightarrow q' = \exp(i\theta_a \gamma_5 t_a) q \quad (6.43)$$

then connect a set of degenerate ground states of the CFL phase. The generators are  $t_a = \frac{\tau_a}{2}$  ( $a = 1, \dots, 8$ ) and  $t_0 = \frac{\tau_0}{4}$ <sup>1</sup>, where the  $\tau_a$  again denote the Gell-Mann matrices in flavor space. These transformations can be parametrized by nine pseudoscalar Goldstone bosons. In order to identify which Nambu-Gorkov operators  $\Gamma_i$  correspond to which Goldstone mode, we apply the transformation (6.43) to the condensates  $s_{AA}$  which are proportional to  $\langle \bar{\Psi} \Gamma_i \Psi \rangle$ , with  $\Gamma_i = \Gamma_{AA}^{s\uparrow}, \Gamma_{AA}^{s\downarrow}$ . The transformation of the fields can be translated into a transformation of the vertices via

$$\langle \bar{\Psi} \Gamma_i \Psi \rangle \rightarrow \langle \bar{\Psi}' \Gamma_i \Psi' \rangle \equiv \langle \bar{\Psi} \Gamma'_i \Psi \rangle. \quad (6.44)$$

For infinitesimal transformations, these are

$$\Gamma'_i = (\mathbb{1} + i\theta_a \gamma_5 t_a)_{\text{NG}} \Gamma_i (\mathbb{1} + i\theta_a \gamma_5 t_a)_{\text{NG}} \approx \Gamma_i + i\theta_a \delta\Gamma_{i,a} \quad (6.45)$$

with

$$\delta\Gamma_i = \{(\gamma_5 t_a)_{\text{NG}}, \Gamma_i\}, \quad (6.46)$$

where  $\{A, B\}$  denotes the anticommutator. The vertices  $\delta\Gamma_{i,a}$  couple the Goldstone bosons to the quarks [87, 88].

In order to illustrate the results, we perform the transformation for two generators  $t_a$  as an example. Explicit calculation of Eq. (6.46) for  $t_a = t_1 = \tau_1/2$  yields

$$\begin{aligned} \delta\Gamma_{22,1}^{s\uparrow} &= 0, & \delta\Gamma_{22,1}^{s\downarrow} &= 0, \\ \delta\Gamma_{55,1}^{s\uparrow} &= i\Gamma_{75}^{p\uparrow}, & \delta\Gamma_{55,1}^{s\downarrow} &= i\Gamma_{75}^{p\downarrow}, \\ \delta\Gamma_{77,1}^{s\uparrow} &= i\Gamma_{57}^{p\uparrow}, & \delta\Gamma_{77,1}^{s\downarrow} &= i\Gamma_{57}^{p\downarrow}. \end{aligned} \quad (6.47)$$

For  $t_a = t_2 = \tau_2/2$  we obtain

$$\begin{aligned} \delta\Gamma_{22,2}^{s\uparrow} &= 0, & \delta\Gamma_{22,2}^{s\downarrow} &= 0, \\ \delta\Gamma_{55,2}^{s\uparrow} &= -\Gamma_{75}^{p\uparrow}, & \delta\Gamma_{55,2}^{s\downarrow} &= \Gamma_{75}^{p\downarrow}, \\ \delta\Gamma_{77,2}^{s\uparrow} &= \Gamma_{57}^{p\uparrow}, & \delta\Gamma_{77,2}^{s\downarrow} &= -\Gamma_{57}^{p\downarrow}. \end{aligned} \quad (6.48)$$

<sup>1</sup>The normalization with the factor  $\frac{1}{4}$  for  $t_0$  is common, but not necessary.

meson	$t_j$	$\Gamma_j$
$\pi^+$	$\frac{1}{2\sqrt{2}}(\tau_1 + i\tau_2)$	$\Gamma_{57}^{p\uparrow}, \Gamma_{75}^{p\downarrow}$
$\pi^-$	$\frac{1}{2\sqrt{2}}(\tau_1 - i\tau_2)$	$\Gamma_{75}^{p\uparrow}, \Gamma_{57}^{p\downarrow}$
$K^+$	$\frac{1}{2\sqrt{2}}(\tau_4 + i\tau_5)$	$\Gamma_{27}^{p\uparrow}, \Gamma_{72}^{p\downarrow}$
$K^-$	$\frac{1}{2\sqrt{2}}(\tau_4 - i\tau_5)$	$\Gamma_{72}^{p\uparrow}, \Gamma_{27}^{p\downarrow}$
$K^0$	$\frac{1}{2\sqrt{2}}(\tau_6 + i\tau_7)$	$\Gamma_{25}^{p\uparrow}, \Gamma_{52}^{p\downarrow}$
$\bar{K}^0$	$\frac{1}{2\sqrt{2}}(\tau_6 - i\tau_7)$	$\Gamma_{52}^{p\uparrow}, \Gamma_{25}^{p\downarrow}$
$\pi^0$	$\frac{\tau_3}{2}$	$\Gamma_{55}^{p\uparrow}, \Gamma_{77}^{p\uparrow}, \Gamma_{55}^{p\downarrow}, \Gamma_{77}^{p\downarrow}$
$\eta_8$	$\frac{\tau_8}{2}$	$\left\{ \begin{array}{l} \Gamma_{22}^{p\uparrow}, \Gamma_{55}^{p\uparrow}, \Gamma_{77}^{p\uparrow}, \\ \Gamma_{22}^{p\downarrow}, \Gamma_{55}^{p\downarrow}, \Gamma_{77}^{p\downarrow} \end{array} \right\}$
$\eta_0$	$\frac{\tau_0}{4}$	

Table 6.1: Pseudoscalar Goldstone modes, the corresponding flavor operators  $t_j$ , and Nambu-Gorkov operators  $\Gamma_j$  contributing to the quark-meson vertex. The  $\Gamma_j$  are obtained by evaluating Eq. (6.46) for  $t_a = t_j$  and all possible  $\Gamma_i = \Gamma_{AA}^{s\uparrow}, \Gamma_{AA}^{s\downarrow}$ .

Comparing the results, it turns out that it is useful to combine different  $t_a$  and work in the so-called ‘‘particle basis’’ in which the operators are combined according to the quantum numbers of the mesons (cf. Tab. 6.1). Using these combinations, we find that each flavored meson is coupled to two Nambu-Gorkov operators only, while the hidden-flavor mesons couple to four (for  $\pi^0$ ) or six (for  $\eta_8$  and  $\eta_0$ ) operators. The results are summarized in Table 6.1.

### 6.3.2 Bethe-Salpeter equation

For the calculation of the mesonic excitations, we solve the Bethe-Salpeter equation

$$\hat{T} = \hat{K} + \hat{K} \hat{J} \hat{T}. \quad (6.49)$$

for quark-quark scattering in Nambu-Gorkov space, shown in Fig. 6.2. The scattering kernel can be extracted from the Lagrangian and expressed in terms of the vertices in Nambu-Gorkov space as

$$\hat{K} = \Gamma_i K_{ij} \bar{\Gamma}_j, \quad (6.50)$$

where  $\Gamma_i$  are the 36 operators defined in Eqs. (6.17) and (6.18) and

$$K_{ij} = 4H \delta_{ij}. \quad (6.51)$$

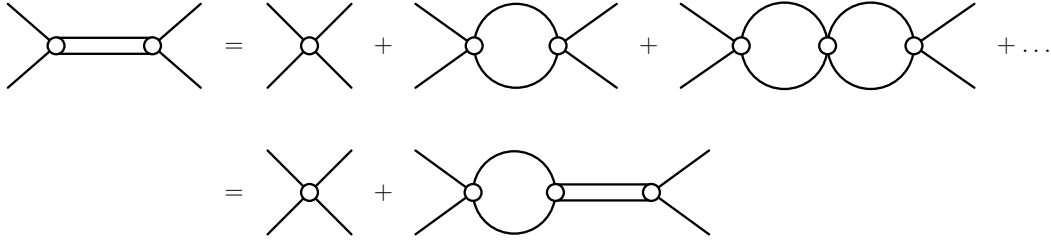


Figure 6.2: Bethe-Salpeter equation for quark-quark scattering.

It is possible to convert the operator equation for the  $T$ -matrix, Eq. (6.49), into a matrix equation by defining

$$\hat{T} = \Gamma_i T_{ij} \bar{\Gamma}_{ij} \quad (6.52)$$

and

$$\bar{\Gamma}_i \hat{J} \Gamma_j = J_{ij}. \quad (6.53)$$

Using these expressions together with Eq. (6.50), we arrive at

$$T = K + KJT. \quad (6.54)$$

This equation can be solved for  $T$ :

$$T(q) = (\mathbb{1} - KJ(q))^{-1} K. \quad (6.55)$$

Finally, inserting Eq. (6.51), we find

$$T(q) = \left( \frac{\mathbb{1}}{4H} - J(q) \right)^{-1}. \quad (6.56)$$

The main ingredient of Eq. (6.56) is the polarization function  $J$  describing the loop in Fig. 6.2

$$\begin{aligned}
 -iJ_{ij}(q) &= \bar{\Gamma}_i \begin{array}{c} k+q \\ \circlearrowleft \\ \circlearrowright \\ k \end{array} \Gamma_j \\
 J_{ij}(q) &= i \int \frac{d^4k}{(2\pi)^4} \frac{1}{2} \text{Tr} [\bar{\Gamma}_i S(k+q) \Gamma_j S(k)]. \quad (6.57)
 \end{aligned}$$

Here, a “vacuum-like” notation has been introduced for brevity. In the medium, the replacements

$$q \rightarrow \begin{pmatrix} i\omega_m \\ \vec{q} \end{pmatrix}, \quad k \rightarrow \begin{pmatrix} i\omega_n \\ \vec{k} \end{pmatrix}, \quad (6.58)$$

with bosonic and fermionic Matsubara frequencies  $i\omega_m = 2m\pi T$  and  $i\omega_n = (2n+1)\pi T$ , respectively, as well as the change of the integral according to

$$i \int \frac{d^4k}{(2\pi)^4} \rightarrow -T \sum_n \int \frac{d^3k}{(2\pi)^3} \quad (6.59)$$

have to be made (cf. Eq. (6.32)). In the numerical calculations, we will again regularize the divergent integrals with a three-momentum cutoff  $\Lambda$ . The calculation of  $J_{ij}$  is presented in Appendix C.1.

The matrices  $T$ ,  $K$ , and  $J$  are  $36 \times 36$  matrices in the space spanned by the operators defined in Eqs. (6.17) and (6.18). The matrix  $J$  is block-diagonal because scalar and pseudoscalar operators do not mix. Moreover, since  $K$  is diagonal ( $K_{ij} = 4H\delta_{ij}$ ),  $T$  is block-diagonal as well. Each of the remaining  $18 \times 18$  blocks can be decomposed further into six  $2 \times 2$  blocks and one  $6 \times 6$  block. The small blocks correspond to the flavored mesons and the  $6 \times 6$  block to the hidden-flavor mesons. The mapping of the blocks, which are characterized by the operators in Nambu-Gorkov space, to the meson states has been obtained by applying axial transformations to the diquark condensates  $s_{AA}$  in Sec. 6.3.1 and is listed in Tab. 6.1.

The  $2 \times 2$  blocks and the  $6 \times 6$  block can be diagonalized by unitary transformations,

$$J' = U^\dagger J U, \quad (6.60)$$

with the 4-momentum dependent unitary matrix  $U$  and

$$J'_{ij} = J^{(i)} \delta_{ij}. \quad (6.61)$$

With this definition at hand, we can define new operators

$$\Gamma'_j = \Gamma_i U_{ij} \quad (6.62)$$

which correspond to the diagonalized polarization matrix  $J'$ . Using these operators, we can rewrite the polarization function as

$$J^{(i)}(q) = J'_{ii}(q) = i \int \frac{d^4k}{(2\pi)^4} \frac{1}{2} \text{Tr} [\bar{\Gamma}'_i S(k+q) \Gamma'_i S(k)]. \quad (6.63)$$

In the basis of the new operators, the scattering kernel  $K$  remains diagonal and the  $T$ -matrix becomes diagonal as well. Using Eq. (6.56), we obtain one equation for each meson mode:

$$T^{(i)}(q) = \frac{1}{\frac{1}{4H} - J^{(i)}(q)}. \quad (6.64)$$

Each mode  $T^{(i)}(q)$  has poles at  $J^{(i)}(q) = 1/(4H)$ . In the vicinity of the poles, the meson modes  $i$  can be parametrized as free bosons with mass  $m_i$  in the presence of a chemical potential  $\mu_i$ :

$$T^{(i)}(q) \approx \frac{-g_i^2}{(q_0 + \mu_i)^2 - c_i^2 \vec{q}^2 - m_i^2}. \quad (6.65)$$

The coupling constant  $g_i$  describes the coupling of the boson to an external quark and  $c_i$  is the in-medium group velocity. We will always restrict ourselves to  $\vec{q} = 0$ , which leads to

$$T^{(i)}(q) \approx \frac{-g_i^2}{(q_0 + \mu_i)^2 - m_i^2}. \quad (6.66)$$

The modes  $T^{(i)}$  describe different bosonic excitations of the CFL ground state. As the polarization loops have the formal structure of quark-antiquark loops, we will call these excitations mesons and use the same names for them as in normal matter. De facto, the vertices entering the polarization loops live in Nambu-Gorkov space and describe quark-antiquark as well as diquark and anti-diquark excitations. In color-superconducting matter these modes are not independent because baryon number is not conserved. As our Lagrangian (Eq. (6.14)) does not contain quark-antiquark interactions, the mesons we are talking about are in fact superpositions of diquarks and antidiquarks (or, more important, di-holes).

The total number of states should not change when states are mixed. There are nine scalar and nine pseudoscalar diquarks and nine scalar and nine pseudoscalar antidiquarks (cf. Eqs. (6.17) and (6.18)), i. e., 36 states altogether. Mixing of these states results in 36 meson states, 18 scalars and 18 pseudoscalars. We only consider the pseudoscalar ones here. Since we have argued that there should be nine pseudoscalar Goldstone bosons in the chiral limit, we expect that the remaining nine pseudoscalars are massive.

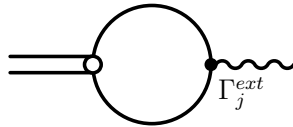


Figure 6.3: Coupling the  $T$ -matrix (double line) to an external meson source (wavy line).

The assignment of the mesons to the blocks of the  $T$ -matrix can be tested by coupling the  $T$ -matrix to an external meson source, as illustrated in Fig. 6.3. To that end, we have to evaluate the loop integral

$$I_{ij}(q) = i \int \frac{d^4k}{(2\pi)^4} \frac{1}{2} \text{Tr} [\bar{\Gamma}_i S(k+q) (\Gamma_j^{ext})_{\text{NG}} S(k)] , \quad (6.67)$$

where  $\Gamma_j^{ext}$  denotes the vertex of the external source and the meson. This vertex is given by  $\Gamma_j^{ext} = i\gamma_5 t_j$  for the pseudoscalar sources and  $\Gamma_j^{ext} = t_j$  for scalar sources, with  $t_j$  as listed in Tab. 6.1. The numerical calculation is analogous to the computation of  $J_{ij}$  because  $I$  is identical to  $J$  up to one of the vertices.

## 6.4 Masses of the Goldstone bosons

We will study the meson masses by calculating the poles of the  $T$ -matrix. Looking at the denominator of the  $T$ -matrix, Eq. (6.66), it is obvious that each mode  $T^{(i)}$  has two poles  $\omega_i^\pm$ , which for  $\vec{q} = 0$  are located at

$$q_0 = \pm m_i - \mu_i \equiv \omega_i^\pm. \quad (6.68)$$

From Eq. (6.68) we can extract the meson masses and chemical potentials as

$$m_i = \frac{1}{2}(\omega_i^+ - \omega_i^-), \quad \mu_i = -\frac{1}{2}(\omega_i^+ + \omega_i^-). \quad (6.69)$$

Comparison with Eq. (6.64) yields the following condition for  $\omega_i^\pm$ :

$$\frac{1}{4H} - J^{(i)}(\omega_i^\pm) = 0. \quad (6.70)$$

In the following we will calculate the masses of the Goldstone bosons in the CFL phase at  $T = 0$  and  $\mu = 500$  MeV. If not stated otherwise, the diquark coupling  $H\Lambda^2 = 1.4$  and the cutoff  $\Lambda = 600$  MeV are used. These values are comparable to those used for the calculation of the phase diagram in the intermediate coupling scenario in Sec. 4.1. We should add that we are in the regular CFL phase for all combinations of parameters that will be used in the remainder of this work.

### 6.4.1 Equal quark masses

We begin the study of the Goldstone boson masses with the simplified case of degenerate quark masses for up, down, and strange quarks ( $m_u = m_d = m_s \equiv m_q$ ). The effect of explicit chiral symmetry breaking can be analyzed by varying  $m_q$ . We will do this for different diquark couplings  $H$ . Since the gap parameter  $\Delta$  only depends very weakly on  $m_q$  (less than 0.1% in the range of  $m_q = 0$  to 30 MeV), we will use its value in the chiral limit to characterize the coupling strength.

Evaluation of Eq. (6.70) shows that  $\omega_i^+$  and  $\omega_i^-$  have the same absolute value for equal quark masses. Thus, Eq. (6.69) implies that the mesons do not feel a chemical potential and that the mass is directly given by the value of  $\omega_i^+$ . The vanishing chemical potentials are in agreement with the LEET predictions for equal quark masses (cf. Eq. (6.3)).

In the CFL phase, the  $SU(3)_{V+c}$  symmetry is unbroken and leaves the octet degenerate. The singlet  $\eta'$  corresponds to the symmetry eigenstate  $\eta_0$  for equal quark masses. Compared to the pseudoscalar octet, it has a slightly higher mass for  $m_q \neq 0$ .

In Fig. 6.4, the masses of the Goldstone bosons are displayed as functions of the quark mass  $m_q$  for three different diquark couplings,  $H\Lambda^2 = 0.6, 1.0,$  and  $1.4$ , corresponding to CFL gaps of 12.5 MeV, 43.2 MeV, and 79.1 MeV, respectively. The

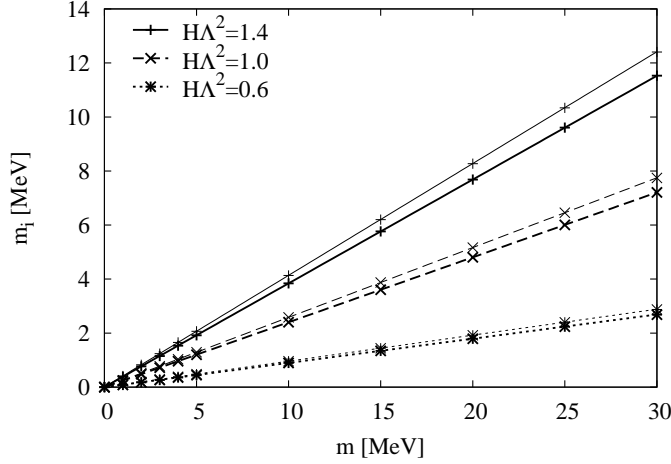


Figure 6.4: Masses of the Goldstone bosons as functions of a degenerate quark mass  $m_q$  for three different couplings. The thick lines belong to the octet and the thin ones to the singlet. Solid:  $H\Lambda^2 = 1.4$  (corresponding to  $\Delta = 79.1$  MeV), dashed:  $H\Lambda^2 = 1.0$  ( $\Delta = 43.2$  MeV), dotted:  $H\Lambda^2 = 0.6$  ( $\Delta = 12.5$  MeV). Points: numerical results, lines: linear fit.

numerical results show an almost perfect linear behavior. This is in agreement with the leading-order LEET results, Eqs. (6.2) and (6.10), which predict that the meson masses are proportional to the quark masses.

In Fig. 6.5, we compare the slopes  $a$  extracted from Fig. 6.4 for

$$m_i = a m_q, \quad (6.71)$$

with the weak-coupling predictions for this factor:

$$a_{\text{wc,octet}} = \sqrt{\frac{8A_{\text{wc}}}{f_{\pi,\text{wc}}^2}} \quad \text{and} \quad a_{\text{wc,singlet}} = \sqrt{\frac{8A_{\text{wc}}}{f_{\eta',\text{wc}}^2}}. \quad (6.72)$$

The low-energy constants  $A_{\text{wc}}$ ,  $f_{\pi,\text{wc}}^2$ , and  $f_{\eta',\text{wc}}^2$  are taken from Eqs. (6.13), (6.11), and (6.12). It can be clearly seen in Fig. 6.5 that the LEET predicts larger proportionality factors than those obtained numerically. Therefore, we get meson masses which are more than 30% smaller for  $\Delta \approx 80$  MeV compared to the weak-coupling predictions (cf. Fig. 6.5).

The slopes  $a$  of the mass functions are increasing with the coupling strength  $H$ , i.e., with increasing  $\Delta$ . This is also expected from the QCD weak-coupling limit,  $A_{\text{wc}} = \frac{3\Delta^2}{4\pi^2}$  [84] and Eq. (6.11) inserted in Eq. (6.72).

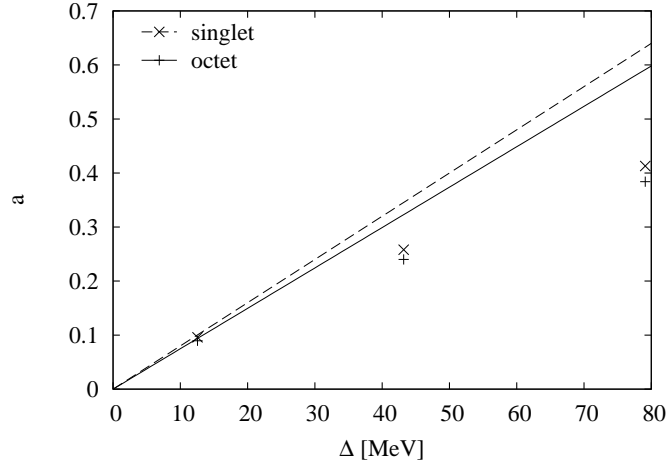


Figure 6.5: Proportionality factor  $a$  from  $m_i = a m_q$  for three different diquark couplings,  $H\Lambda^2 = 0.6, 1.0,$  and  $1.4$ , corresponding to CFL gaps of 12.5 MeV, 43.2 MeV, and 79.1 MeV, respectively. The points are the slopes extracted from Fig. 6.4. The lines are obtained by inserting the weak-coupling QCD results for  $f_\pi, f_{\eta'}$ , and  $A$ , Eqs. (6.11), (6.12), and (6.13), into Eq. (6.72).

### 6.4.2 Unequal quark masses

Now we turn to a more realistic scenario with a heavier strange quark and study the effect of unequal quark masses. The up- and down quark masses will be kept fixed and equal while the strange quark mass will be varied. We use  $m_u = m_d = 30$  MeV in order to be able to vary  $m_s$  over a wider range before kaon condensations sets in.

In Fig. 6.6, the poles  $\omega_i^\pm$  of the Goldstone modes are displayed as functions of the strange quark mass. For unequal quark masses, the flavor  $SU(3)_V$  symmetry is broken and no residual symmetry is left which connects *all* states of the pseudoscalar meson octet. The poles, which were degenerate for the octet in the case of equal quark masses, split into four branches, resulting in five branches in total. For the flavored mesons, these correspond to states with different strangeness, i. e., the pions with  $S = 0$ , the kaons with  $S = +1$ , and the antikaons with  $S = -1$ . Since we have kept  $m_u$  and  $m_d$  equal, the different isospin states of these modes, i. e.,  $\pi^\pm$  and  $\pi^0$ ,  $K^+$  and  $K^0$ , as well as  $K^-$  and  $\bar{K}^0$ , remain degenerate. The remaining two branches are the  $\eta'$ , which shows a similar behavior as the pions but with slightly larger absolute values of  $\omega^\pm$ , and the  $\eta$  with nearly constant values of  $\omega^\pm$ .

All masses and chemical potentials of the Goldstone bosons are shown in Fig. 6.7. The masses are moderately increasing with  $m_s$ . The kaons and antikaons have the same mass. We find an “inverse mass ordering” ( $m_\eta < m_K < m_\pi$ ) which was predicted in [84] and briefly discussed in Sec. 6.1. The  $\eta'$  drops out of the inverse mass ordering



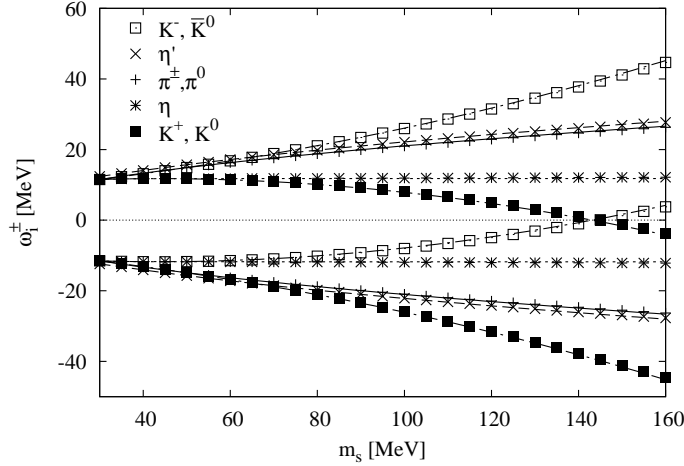


Figure 6.6: Poles  $\omega_i^\pm$  of the  $T$ -matrix at  $\vec{q} = 0$  as functions of the strange quark mass for  $m_u = m_d = 30$  MeV and  $H\Lambda^2 = 1.4$  ( $\Delta = 79.1$  MeV). The various points indicate the numerical results. The lines correspond to the LEET predictions.

scheme and is slightly heavier than the pions.

We can compare the results with those derived in the LEET. The hidden-flavor mesons,  $\pi^0$ ,  $\eta$ , and  $\eta'$  do not feel a meson chemical potential. Furthermore, the chemical potentials of the charged pions vanish for  $m_u = m_d$ , whereas the chemical potentials of the kaons have equal absolute values but opposite signs for particles and antiparticles,  $\mu_K = -\mu_{\bar{K}}$ . For the flavored mesons and the  $\pi^0$ , the masses are given by Eq. (6.1), while Eqs. (6.8) and (6.9) describe the masses of  $\eta$  and  $\eta'$ . Instead of the LEET prefactors  $\frac{4A}{f_\pi^2}$  and  $\frac{4A}{f_{\eta'}^2}$ , we use the slopes  $a_{\text{octet}}$  and  $a_{\text{singlet}}$  which we have calculated in the last section. As an example, we have the following replacement for the pions

$$m_\pi^2 = \frac{8A}{f_\pi^2} m_q m_s \rightarrow a_{\text{octet}}^2 m_q m_s. \quad (6.73)$$

To plot the masses of the  $\eta$  and the  $\eta'$ , we additionally have to use the values of  $f_\pi$  and  $f_{\eta'}$  that will be calculated in the next section. The resulting functions are indicated by the lines in Fig. 6.7. We find an almost perfect agreement between our numerical results and the LEET predictions for the masses and the chemical potentials with small deviations only for higher values of  $m_s$ . The agreement would not be good if we had used the weak-coupling results for  $A$  and  $f_\pi$  in the prefactors.

In order to understand the behavior of the  $\eta$  and  $\eta'$  masses we need to simplify the expressions (6.8) and (6.9) for the mass eigenvalues. We can use the fact that in the weak coupling formulas, Eqs. (6.11) and (6.12),  $f_\pi$  and  $f_{\eta'}$  are very similar and rewrite

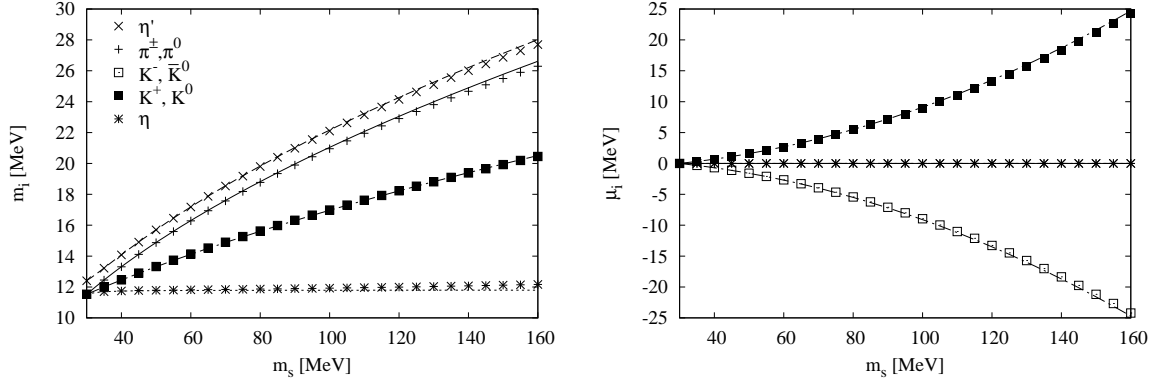


Figure 6.7: Properties of the Goldstone modes as functions of the strange quark mass for  $m_u = m_d = 30$  MeV and  $H\Lambda^2 = 1.4$  ( $\Delta = 79.1$  MeV): meson masses (left panel) and meson chemical potentials (right panel). The various points indicate the numerical results. The lines correspond to the LEET predictions. The meaning of the different point types are the same for both plots.

$f_{\eta'}$  as

$$f_{\eta'}^2 = f_\pi^2 - \delta f^2. \quad (6.74)$$

Expanding Eqs. (6.9) and (6.8) up to order  $\delta f^2$  yields

$$m_{\eta'}^2 \approx \frac{8A}{f_\pi^2} \left(1 + \frac{2}{3} \frac{\delta f^2}{f_\pi^2}\right) m_q m_s = \left(1 + \frac{2}{3} \frac{\delta f^2}{f_\pi^2}\right) m_\pi \quad (6.75)$$

and

$$m_\eta^2 \approx \frac{8A}{f_\pi^2} \left(1 + \frac{1}{3} \frac{\delta f^2}{f_\pi^2}\right) m_q^2. \quad (6.76)$$

These expressions explain why the  $\eta'$  behaves similar to the pion, while the mass of the  $\eta$  stays nearly constant for increasing  $m_s$ .

### Kaon condensation

Meson condensation sets in when the chemical potential  $\mu_i$  reaches the corresponding meson mass,

$$\mu_i(m_q, m_s^{\text{crit}}) = m_i(m_q, m_s^{\text{crit}}). \quad (6.77)$$

At the critical strange quark mass,  $\omega_i^+ = m_i - \mu_i$  vanishes. For our parameters, this happens for the kaon branch ( $K^+$  and  $K^0$ ) at  $m_s^{\text{crit}} \approx 145$  MeV (see Fig. 6.6). For higher strange quark masses, the CFL phase is no longer the correct ground state and the shown results have no physical meaning.

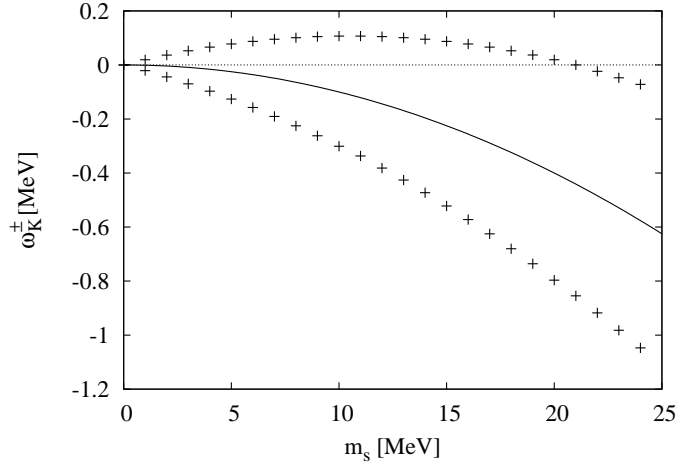


Figure 6.8: Poles of the  $T$ -matrix at  $\vec{q} = 0$  for the kaons ( $K^+$  and  $K^0$ ) as functions of the strange quark mass for  $m_u = m_d = 0$  and  $H\Lambda^2 = 1.7$  ( $\Delta = 107.9$  MeV). The crosses indicate the numerical results. The lines correspond to the predictions from Eqs. (6.68), (6.69), and (6.3).

Inserting the LEET predictions Eqs. (6.1) and (6.3) into Eq. (6.77), the critical strange quark mass is approximately given by [62]

$$m_s^{\text{crit}} \approx \left( \frac{16 \mu^2 A}{f_\pi^2} \right)^{1/3} m_q^{1/3} \quad (6.78)$$

for  $m_q \ll m_s$ . In the limit  $m_q = 0$ , this suggests that kaon condensation is favored for arbitrarily small strange quark masses. However, this contradicts an earlier NJL model study [15], where a non-zero critical strange quark mass was found even for  $m_q = 0$ . There, Goldstone boson condensation was studied without an explicit construction of the Goldstone bosons by analyzing the stability of the CFL ground state against partially rotating the scalar diquark condensates into pseudoscalar ones.

We can consider this issue now within our approach and check these results from another perspective. Since it was argued in [15] that the non-vanishing kaon mass should be a higher-order effect in the interaction, we perform the subsequent calculations with a larger coupling,  $H\Lambda^2 = 1.7$ , corresponding to  $\Delta = 107.9$  MeV.

To that end, we calculate the poles  $\omega_i^+$  and  $\omega_i^-$  of the  $T$ -matrix in the kaon channel at  $m_q = 0$  as functions of the strange quark mass and display the results in Fig. 6.8. Obviously, there is some discrepancy between our results and the LEET predictions. In order to identify its origin, we display the kaon mass  $m_K$  and the kaon chemical potential  $\mu_K$  in Fig. 6.9. The kaon chemical potential is in nice agreement with the LEET prediction, but the kaon mass is not vanishing as predicted by Eq. (6.1), but rises linearly with  $m_s$ . This explains the deviations for the poles. Since we find a

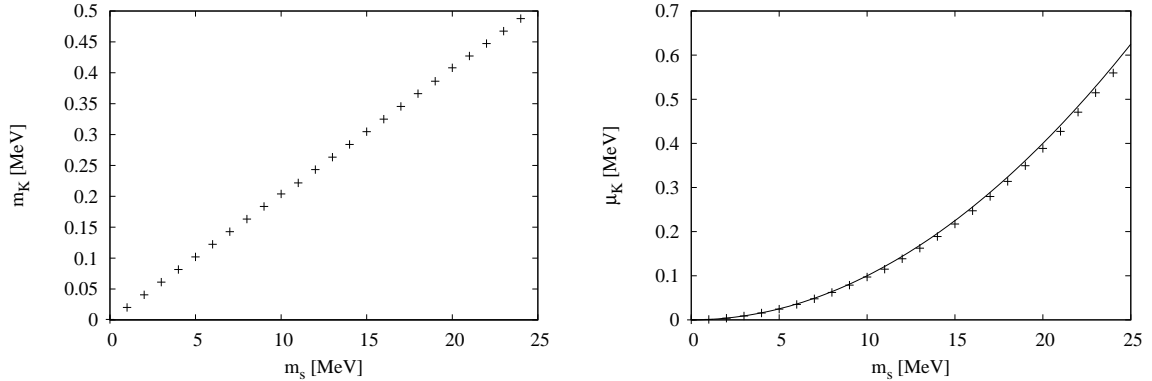


Figure 6.9: Kaon masses (left panel) and kaon chemical potentials (right panel) as functions of the strange quark mass for  $m_u = m_d = 0$  and  $H\Lambda^2 = 1.7$  ( $\Delta = 107.9$  MeV). The points indicate the numerical results and the lines correspond to the LEET predictions. Note that from Eq. (6.1),  $m_K$  is expected to vanish in the LEET approach.

non-vanishing kaon mass, the poles  $\omega_K^+$  and  $\omega_K^-$  are not degenerate (cf. Eq. (6.68)). The non-vanishing mass is in agreement with the findings of [15]. A linear fit of the kaon mass with  $m_K = a_s m_s$  yields  $a_s = 0.0203$ . Moreover, by varying the coupling strength, we find numerically that  $a_s$  depends quadratically on  $\Delta$ . This is in agreement with the interpretation that it is a higher-order correction in the interaction.

We can combine our numerical findings with the LEET result for the kaon mass, Eq. (6.1), to obtain

$$m_K = \sqrt{\frac{4A}{f_\pi^2} m_q (m_q + m_s) + a_s^2 m_s^2}. \quad (6.79)$$

Comparing  $a_s^2 \approx 0.0004$  with  $4A/f_{\pi,wc} \approx 0.12$  shows that  $a_s^2$  is three orders of magnitude smaller and therefore only visible when the leading order, Eq. (6.1), is suppressed by choosing a very small value for  $m_q$ .

In Fig. 6.10,  $m_s^{crit}$  is shown as a function of  $m_q^{1/3}$ . The points again display our numerical values. The exact LEET predictions, which are the solution of Eq. (6.77) with Eqs. (6.1) and (6.3) inserted for mass and chemical potential, are shown by the solid line, while the approximation, Eq. (6.78) is given by the dashed line. The dotted line is based on Eq. (6.79) with  $a_s = 0.0203$ . The results of our model calculations always lie above the LEET predictions. However, while the deviations are small for  $m_q \gtrsim 1$  MeV, they are essential for smaller values of  $m_q$ . In particular, we find that kaon condensation does not occur for arbitrary small values of the strange quark mass, but only for  $m_s \gtrsim 21$  MeV.

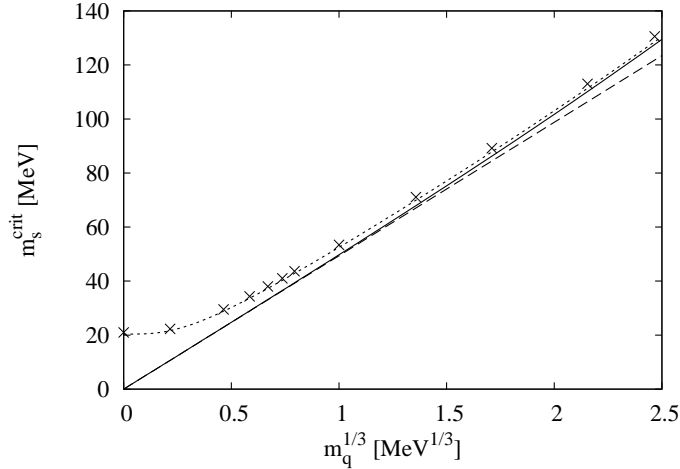


Figure 6.10: Critical strange quark mass  $m_s^{crit}$  for kaon condensation as a function of  $m_q^{1/3}$ , where  $m_q \equiv m_u = m_d$ . The crosses mark the NJL-model results, the solid line shows the LEET predictions using Eqs. (6.1) and (6.3), while the dashed line displays the approximate solution, Eq. (6.78). The dotted line is based on Eq. (6.79) with  $a_s = 0.0203$ . The NJL-model calculations have been performed with  $H\Lambda^2 = 1.7$ , corresponding to  $\Delta = 107.9$  MeV.

## 6.5 Masses of the higher-lying excitations

As already discussed, we find nine higher-lying excitations which remain massive even in the chiral limit, in addition to the nine Goldstone modes. These massive modes are obtained by the diagonalization procedure described in Sec. 6.3.2, completely analogous to the Goldstone modes.

If not stated otherwise, we use our former parameter set,  $H\Lambda^2 = 1.4$  and  $\Lambda = 600$  MeV, for the following calculation.

### 6.5.1 Equal quark masses

As before, we begin our study with the simplified case of equal quark masses,  $m_u = m_d = m_s \equiv m_q$ . In the left panel of Fig. 6.11 the masses of the two octets (Goldstone bosons and higher-lying excitations) are shown as functions of  $m_q$ . The right panel of Fig. 6.11 shows a detailed view of the higher-lying excitations. While the masses of the Goldstone bosons increase linearly with a sizeable slope, the masses of the higher-lying excitations stay nearly constant. In fact, they always stay very close to  $2\Delta$  (dotted line), i. e., the threshold for decay into two quasiparticles. We find that the mesons are only weakly bound for not too large values of  $m_q$ , reaching the decay threshold at  $m_q \approx 190$  MeV. At this point the curve ends because we cannot find solutions above

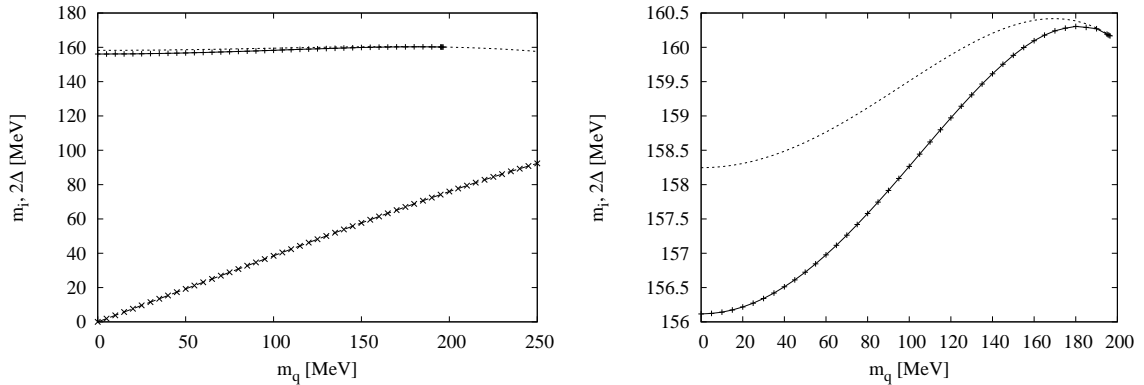


Figure 6.11: Masses of the pseudoscalar octet excitations as functions of a common quark mass  $m_q$ . Left panel: higher-lying modes in comparison with the Goldstone modes. Right panel: higher-lying modes. The dotted line indicates the decay threshold  $2\Delta$  in both plots.

threshold in our approach. For the same reason, we cannot determine the mass of the higher-lying excitation in the singlet channel, which is always above threshold. The behavior of the  $T$ -matrix below threshold seems to indicate that the mass of the singlet meson is rather close to the threshold as well. A quantitative estimate, however, is difficult to obtain because of threshold effects.

The higher-lying pseudoscalar modes in the CFL phase have also been studied in Ref. [19] in a similar NJL model in the chiral limit. In contrast to our result in Fig. 6.11, it was found that the octet states are unbound. The authors used the parameters  $H\Lambda^2 = 1.73925$  and  $\Lambda = 602.3$  MeV and have included an additional quark-antiquark interaction part in their Lagrangian. However, this term is irrelevant in the CFL phase in the chiral limit because the quark-antiquark condensates vanish. Thus, in order to make a direct comparison, we have calculated the octet mass as a function of the quark number chemical potential  $\mu$ , using the parameters of Ref. [19]. Our results are shown in Fig. 6.12. In the chosen interval,  $360 \text{ MeV} < \mu < 500 \text{ MeV}$ , the masses of the excitations vary between 189 and 223 MeV. For comparison, we also display the threshold  $2\Delta$ . As one can see, the meson masses closely follow this line, but always stay below. Thus, we find the octet modes to be bound in the entire interval, in contrast to Ref. [19]. Since the authors of Ref. [19] restricted themselves to the chiral limit from the beginning, they were able to derive a simpler equation (Eq. (33) in [19]) for the meson masses compared to our approach. To discuss the origin of the discrepancy of the results, we checked that this equation has indeed bound state solutions which agree very well with our results. However, it cannot be ruled out that several branches of solutions exist. Hence, the resonance state solutions found in [19] could be correct as well.

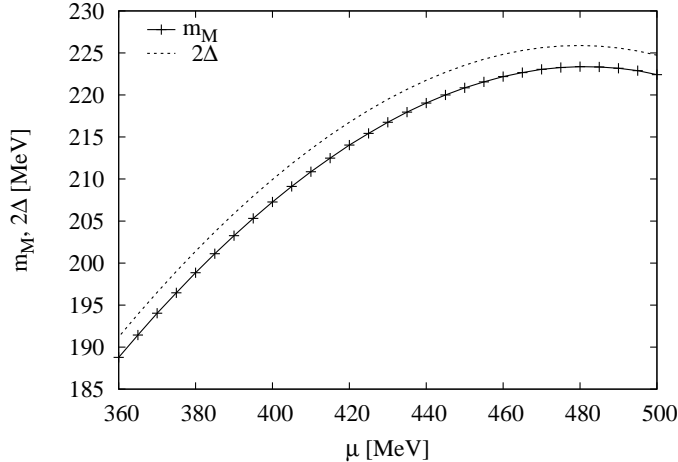


Figure 6.12: The higher-lying pseudoscalar octet mode in the chiral limit as a function of the quark chemical potential  $\mu$  (solid line with points). The parameters are  $H\Lambda^2 = 1.73925$ ,  $\Lambda = 602.3$  MeV [19]. The dotted line indicates the decay threshold  $2\Delta$ .

### 6.5.2 Unequal quark masses

Next, we study the effect of an explicit breaking of the  $SU(3)$ -flavor symmetry on the higher-lying excitations. As in the previous section, we choose  $m_u = m_d = 30$  MeV and vary the strange quark mass  $m_s$ . We will simply use the names “pions”, “kaons” etc. for the higher-lying excitations according to their flavor quantum numbers, as no confusion with the vacuum states or the Goldstone modes in the CFL phase is possible.

As in the case of equal quark masses, we only find higher-lying excitations for the octet modes. The positions of the  $\omega^+$  poles are displayed in Fig. 6.13. The poles of the pions and the  $\eta$  stay nearly constant around 155 MeV whereas the pole of the antikaons ( $K^-$  and  $\bar{K}^0$ ) grows from 156 MeV for a quark mass of 30 MeV to 177 MeV for a quark mass of 140 MeV. For the kaons ( $K^+$  and  $K^0$ ) the situation is reversed, the position of their pole moves from 156 MeV to 136 MeV.

It should be noted that the threshold for decay into two quasiparticles is no longer equal to  $2\Delta$  in the case of unequal quark masses. In fact, the fermionic excitation spectrum contains five different particle branches (two singlets, two doublets and one triplet) with different excitation gaps in this case, see e.g. Ref. [89]. Thus, the decay threshold for the different meson modes depends in a complicated way on their respective quasiparticle composition and increases with  $m_s$  in some channels, while it decreases in others. It turns out that the splitting of the various mesonic modes closely follows the splitting of the decay thresholds.

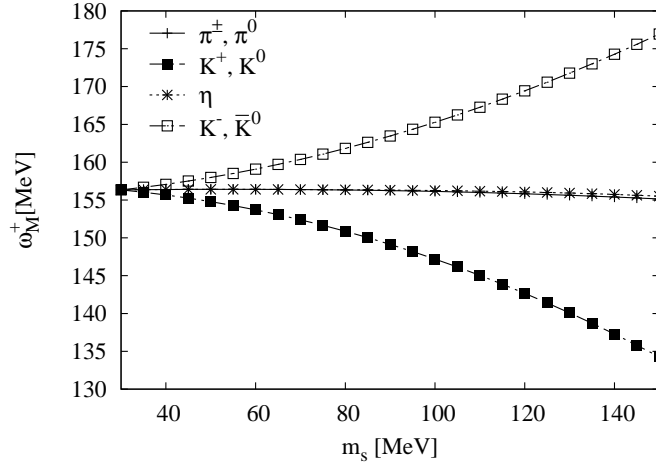


Figure 6.13: Positive poles of the  $T$ -matrix for the higher-lying modes as a function of the strange quark mass  $m_s$  for  $m_u = m_d = 30$  MeV.

In Fig. 6.13, we only show the poles  $\omega_i^+$  at positive values of  $q_0$ . In addition, each mode has another pole  $\omega_i^-$  at negative energies, which is not shown in the figure. Applying Eq. (6.69), we can calculate the mass and effective chemical potential for each meson. These are plotted in Fig. 6.14. In the upper panel the masses are shown. At first they increase slightly and then decrease with  $m_s$ . Note however, that this happens on a very small scale from 156.4 to 155.2 MeV, i. e., unlike the Goldstone bosons, they stay nearly constant. On this scale we can also see that the  $\eta$  and the pions are not degenerate. (This was already the case for the poles shown in Fig. 6.13, but hardly visible.)

In the lower part of Fig. 6.14 we show the effective meson chemical potentials. The chemical potentials vanish for the pions and the  $\eta$ , whereas they are negative for kaons and positive for antikaons, with equal absolute values. This is exactly the same result as for the Goldstone bosons. Since the effective meson chemical potentials are induced by the mass differences of different quark flavors, they should only depend on the flavor content of the meson, hence, there should be no difference in the chemical potentials of the Goldstone bosons and the higher-lying modes. Therefore, we can compare our numerical results with the LEET predictions for the Goldstone bosons, Eq. (6.3). These are indicated by the lines in the lower panel of Fig. 6.14 and nicely fit the numerical results. Since we kept  $m_u = m_d$ , there is again only an effective strangeness chemical potential, but no isospin chemical potential.



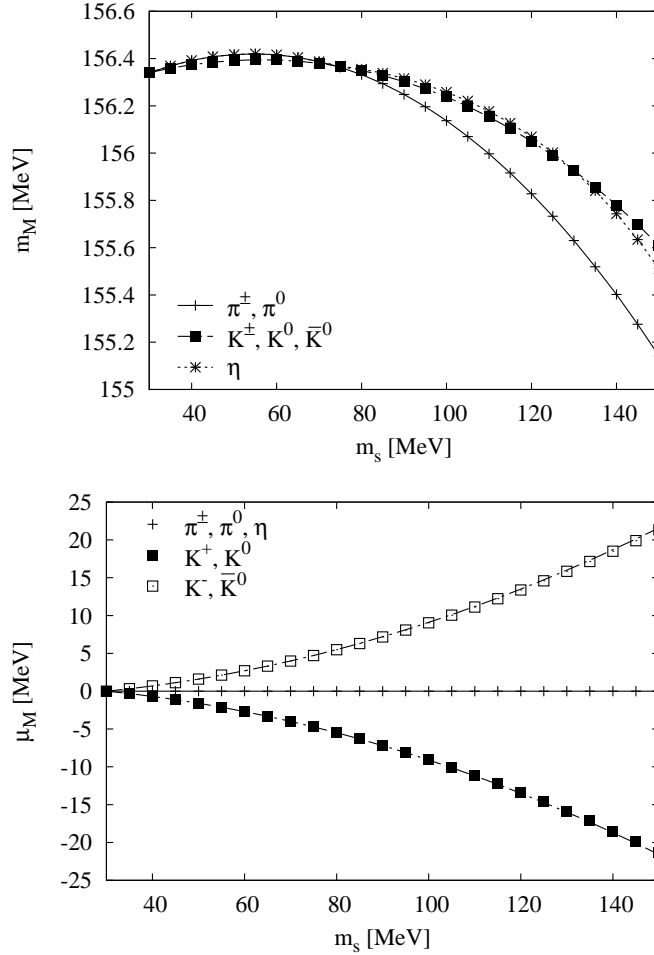


Figure 6.14: Masses (upper panel) and effective meson chemical potentials (lower panel) of the higher-lying excitations as functions of the strange quark mass  $m_s$  for  $m_u = m_d = 30$  MeV. The various points indicate the numerical calculations using Eq. (6.69). In the upper panel, these points have been connected by straight lines to guide the eye. The lines in the lower panel correspond to Eq. (6.3).



# 7 Meson decay constants

In the previous chapter we have calculated the meson masses in the CFL phase. These are very well described by the predictions of the LEET. However, we have seen that our results were not in agreement with the low-energy constants obtained in the weak coupling limit. To shed some light on this issue, the meson decay constants will be calculated in the following.

## 7.1 Derivation of the meson decay constants

In analogy to the vacuum, the pseudoscalar meson decay constants are related to the loop which couples the meson  $j$  to an external axial current  $A_{5i}^\mu = (\gamma^\mu \gamma_5 t_i)_{\text{NG}}$ ,

$$F'_{ij}{}^\mu(q) = i \int \frac{d^4k}{(2\pi)^4} \frac{1}{2} \text{Tr} [\bar{A}_{5i}^\mu S(k+q) \Gamma'_j S(k)] , \quad (7.1)$$

as depicted in Fig. 7.1, The meson decay constants are associated with the values of  $F'_{ij}{}^\mu$  at  $q_0 = m_j$  via

$$f_j q^\mu = i g_j F'_{ij}{}^\mu |_{q_0=m_j} , \quad (7.2)$$

with no summation over the index  $j$  on the right hand side, and the coupling constant  $g_j$  which has been implicitly defined in the  $T$ -matrix in Eq. (6.65). As seen in Sec. 6.3, each flavor operator  $t_i$ , defined in Tab. 6.1, couples to one specific combination  $\Gamma'_j$  of the pseudoscalar vertices. The corresponding vertices  $\Gamma_{AA'}^{p\uparrow}$  and  $\Gamma_{AA'}^{p\downarrow}$  are listed in Tab. 6.1 as well. Numerically, the combinations are obtained by diagonalization of the  $T$ -matrix, which corresponds to a diagonalization of the polarization function (cf. Eqs. (6.60) to (6.62)).

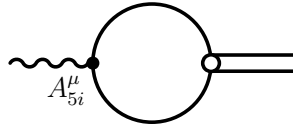


Figure 7.1: Weak decay of the pseudoscalar mesons: coupling of the  $T$ -matrix (double line) to an external axial current  $A_{5i}^\mu$  (wavy line).

In general, there are timelike and spacelike decay constants. However, since we only consider mesons with vanishing three-momenta ( $\vec{q} = 0$ ), we are restricted to the timelike decay constants. To this end, we have to evaluate the loop which describes the coupling of the meson  $i$  to the external axial current  $A_{5i}^0$  (cf. Eq. (7.1)):

$$F_{ij}^{\prime 0} = i \int \frac{d^4 k}{(2\pi)^4} \frac{1}{2} \text{Tr}[\bar{A}_{5i}^0 S(k+q) \Gamma'_j S(k)]. \quad (7.3)$$

Since we already know that each meson  $j$  couples to only one axial current, we have to solve

$$f_i q_0 = i g_i F_{ii}^0(q)|_{q_0=m_i, \vec{q}=0}, \quad (7.4)$$

for the pseudoscalar meson decay constants  $f_i$ , where there is no summation over the index  $i$  on the right hand side (cf. Eq. (7.2)).

We will calculate the meson decay constants for equal quark masses only. In this case, the octet containing the pions, the kaons and the  $\eta$  is degenerate and the  $\eta'$  can be identified with the  $\eta_0$ . For the octet, we will representatively inspect the axial current for the  $\pi^+$

$$A_{5\pi^+}^0 = \left( \frac{1}{2\sqrt{2}} (\tau_1 + i\tau_2) \gamma^0 \gamma_5 \right)_{\text{NG}}. \quad (7.5)$$

The axial current for the  $\eta_0$  is given by

$$A_{5\eta_0}^0 = \left( \frac{\tau_0}{4} \gamma^0 \gamma_5 \right)_{\text{NG}}. \quad (7.6)$$

### 7.1.1 Numerical calculation of the decay constant

The following numerical calculation of the meson decay constants is valid for equal quark masses. However, it cannot be applied in the exact chiral limit, because  $q_0 = 0$  is not tractable in this approach (cf. Eq. (7.7)). In that case, we will use  $m_q = 0.1 \text{ MeV}$  which leads to an  $m_i$  which is not exactly zero. The deviation from the exact chiral limit is found to be negligible (see Fig. 7.3). This allows us to directly solve Eq. (7.4) for  $f_i$ :

$$f_i = \frac{i g_i}{q_0} F_{ii}^0(q)|_{q_0=m_i, \vec{q}=0}. \quad (7.7)$$

First of all, we have to evaluate  $F_{ii}^0(q)|_{q_0=m_i, \vec{q}=0}$  as given in Eq. (7.3). Since the loop has practically the same structure as the polarization function, the numerical procedure is exactly the same as for the calculation of the polarization function  $J_{ij}$  presented in Appendix C.1.

Next, we need the coupling constant  $g_i$ , which is for equal quark masses implicitly defined in

$$T^{(i)}(q) \approx \frac{-g_i^2}{q_0^2 - m_i^2}. \quad (7.8)$$

Here, we have used that the meson chemical potentials vanish for equal quark masses, as discussed in the previous chapter. Equating  $T^{(i)}(q_0) = \left(\frac{1}{4H} - J^{(i)}(q_0)\right)^{-1}$  with Eq. (7.8) and solving for  $-g_i^{-2}$  yields

$$-g_i^{-2} = \frac{\frac{1}{4H} - J^{(i)}}{q_0^2 - m_i^2}. \quad (7.9)$$

Expanding the numerator around  $q_0^2 = m_i^2$ , we obtain

$$\frac{1}{4H} - J \approx - \left. \frac{dJ^{(i)}}{dq_0^2} \right|_{q_0^2=m_i^2} (q_0^2 - m_i^2). \quad (7.10)$$

Inserting Eq. (7.10) into Eq. (7.9) brings us to the final expression for  $g_i$ ,

$$g_i = \left( \left. \frac{dJ^{(i)}}{dq_0^2} \right|_{q_0^2=m_i^2} \right)^{-2}. \quad (7.11)$$

The derivative can be taken starting from Eq. C.8 in Appendix C.1 to be

$$\begin{aligned} \frac{dJ^{(i)}}{dq_0^2} &= \frac{1}{2q_0} \frac{dJ^{(i)}}{dq_0} \\ &= \frac{1}{2q_0} \frac{i}{4\pi} \oint dz \int \frac{d^3k}{(2\pi)^3} (\bar{\Gamma}'_i)_{ij} (\Gamma'_i)_{ji} \frac{1}{(z + q_0 - \varepsilon_j)^2} \frac{1}{z - \varepsilon_i} (e^{z/T} + 1)^{-1}. \end{aligned} \quad (7.12)$$

The evaluation of the expression is described in Appendix C.2.

### 7.1.2 Semianalytical derivation of the pion decay constant in the chiral limit

In order to calculate Eq. (7.4) analytically, we first have to know the analytical form of the vertex  $\Gamma'_i$ . In the chiral limit, it is possible to analytically derive the operators  $\Gamma'_i$  contributing to Goldstone boson  $i$  using chiral Ward-Takahashi identities.

#### Axial Ward-Takahashi identity

The axial Ward-Takahashi identities provide a connection between the dressed vertex and the inverse propagator. The procedure has been presented in [22].

A necessary ingredient is the dressed vertex which couples an external axial current to a quark, as shown in Fig. 7.2. A self-consistency equation for the dressed vertex is obtained by attaching an external axial current to each side of the Dyson equation, Fig. 6.1. This is shown in the first line of Fig. 7.2. The summation over the loops in

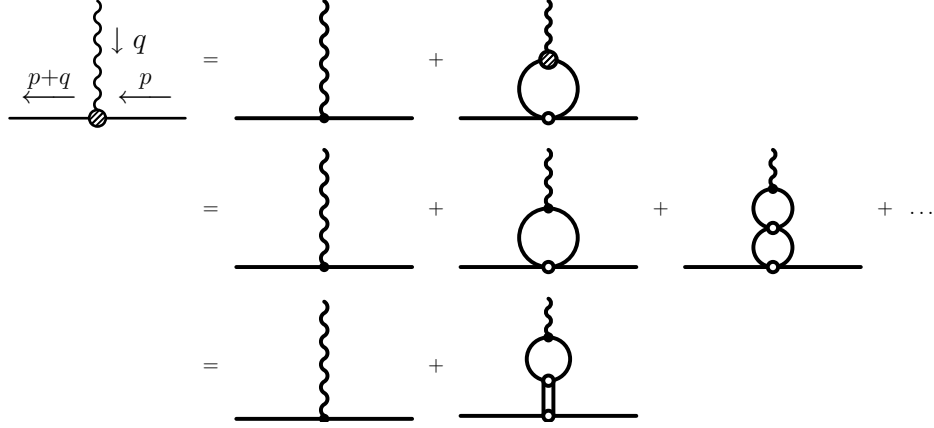


Figure 7.2: Dressed vertex of an external axial current (wavy line) coupled to a quark. The shaded circles indicate dressed vertices and the black dots bare ones. The open circles correspond to quark-quark vertices and the double line to the  $T$ -matrix, as in Fig. 6.2.

the second line can be rewritten in terms of the  $T$ -matrix, as in Fig. 6.2. The last line of Fig. 7.2 can then be expressed as

$$\Gamma_{5j}^\mu(p; q) = (\gamma^\mu \gamma_5 t_j)_{NG} + T^{(i)}(q) \bar{\Gamma}'_i(-F_{ij}^\mu), \quad (7.13)$$

with  $F_{ij}^{\prime\mu}$  as defined in Eq. (7.1). Strictly speaking, the loop in the last line of Fig. 7.2 corresponds to the time-reversed process of the Goldstone boson decay, i. e., it couples an incoming axial current to the  $T$ -matrix. However, this only results in a sign change which will be canceled later by a another minus sign for  $q_0$  in the definition of the decay constant (cf. Eq. (7.2)) due to the outgoing instead of incoming pion.

For  $\vec{q} = 0$  and  $q_0$  approaching the mass  $m_j$  of meson  $j$ , Eqs. (7.8) and (7.2) can be inserted into Eq. (7.13), which leads to [22]

$$\Gamma_{5j}^0(p; q_0 \rightarrow m_j) = i \frac{g_j f_j q_0}{q_0^2 - m_j^2} \bar{\Gamma}'_j + \text{non-singular terms}. \quad (7.14)$$

The bare vertex and corrections, which arise in Eqs. (7.8) and (7.2) for  $q_0$  approaching  $m_j$  but not being exactly equal to  $m_j$ , are summarized in the “non-singular terms”. This is useful because only the singular part of  $\Gamma_{5j}^0$  will be needed in the following calculations.

The dressed vertex function has to satisfy the axial Ward-Takahashi identity (in the chiral limit)

$$q_\mu \Gamma_{5j}^\mu(p; q) = S^{-1}(p+q) (\gamma_5 t_j)_{NG} + (\gamma_5 t_j)_{NG} S^{-1}(p). \quad (7.15)$$

The right hand side of this equation is finite, while  $q_0$  times Eq. (7.14) seems to have a singularity at  $q_0 = m_j$ . Thus, one concludes that the singularity in Eq. (7.14) must

be suppressed either by  $m_j = 0$  or by  $g_j f_j = 0$  [22]. Of the 18 pseudoscalar mesons discussed in Chap. 6, nine are massless Goldstone bosons and nine are massive. Hence, it is expected that both scenarios are realized. Combining Eqs. (7.14) and (7.15) for the massless solution  $m_j = 0$  (indicated by the superscript 0) leads to

$$i g_j f_j \Gamma_j^{\prime(0)} = S^{-1}(p) (\gamma_5 t_j)_{NG} + (\gamma_5 t_j)_{NG} S^{-1}(p). \quad (7.16)$$

The right hand side of Eq. (7.16) can be calculated using the inverse dressed propagator (6.25) with  $m = 0$  and choosing the gap parameter  $\Delta$  to be real. As a solution, one obtains [22]

$$\Gamma_j^{\prime(0)} = - \sum_{A=2,5,7} \left\{ (\Gamma_{AA}^{s\uparrow} - \Gamma_{AA}^{s\downarrow}), (\gamma_5 t_j)_{NG} \right\} \quad (7.17)$$

with

$$g_j f_j = \Delta. \quad (7.18)$$

Eq. (7.18) will turn out to be useful later on for the semianalytical derivation of the pion decay constant.

Explicit evaluation of Eq. (7.17) yields

$$\begin{aligned} \Gamma_{\pi^+}^{\prime(0)} &= \frac{-i}{\sqrt{2}} \left( \Gamma_{57}^{p\uparrow} - \Gamma_{75}^{p\downarrow} \right), & \Gamma_{\pi^-}^{\prime(0)} &= \frac{-i}{\sqrt{2}} \left( \Gamma_{75}^{p\uparrow} - \Gamma_{57}^{p\downarrow} \right), \\ \Gamma_{K^+}^{\prime(0)} &= \frac{i}{\sqrt{2}} \left( \Gamma_{27}^{p\uparrow} - \Gamma_{72}^{p\downarrow} \right), & \Gamma_{K^-}^{\prime(0)} &= \frac{i}{\sqrt{2}} \left( \Gamma_{72}^{p\uparrow} - \Gamma_{27}^{p\downarrow} \right), \\ \Gamma_{K^0}^{\prime(0)} &= \frac{-i}{\sqrt{2}} \left( \Gamma_{25}^{p\uparrow} - \Gamma_{52}^{p\downarrow} \right), & \Gamma_{\bar{K}^0}^{\prime(0)} &= \frac{-i}{\sqrt{2}} \left( \Gamma_{52}^{p\uparrow} - \Gamma_{25}^{p\downarrow} \right), \end{aligned} \quad (7.19)$$

for the flavored mesons and

$$\begin{aligned} \Gamma_{\pi^0}^{\prime(0)} &= -\frac{i}{2} \left( \Gamma_{55}^{p\uparrow} - \Gamma_{77}^{p\uparrow} - \Gamma_{55}^{p\downarrow} + \Gamma_{77}^{p\downarrow} \right), \\ \Gamma_{\eta_8}^{\prime(0)} &= -\frac{i}{2\sqrt{3}} \left( 2\Gamma_{22}^{p\uparrow} - \Gamma_{55}^{p\uparrow} - \Gamma_{77}^{p\uparrow} - 2\Gamma_{22}^{p\downarrow} + \Gamma_{55}^{p\downarrow} + \Gamma_{77}^{p\downarrow} \right), \\ \Gamma_{\eta_0}^{\prime(0)} &= -\frac{i}{\sqrt{6}} \left( \Gamma_{22}^{p\uparrow} + \Gamma_{55}^{p\uparrow} + \Gamma_{77}^{p\uparrow} - \Gamma_{22}^{p\downarrow} - \Gamma_{55}^{p\downarrow} - \Gamma_{77}^{p\downarrow} \right), \end{aligned} \quad (7.20)$$

for the hidden-flavor mesons. From this, it is obvious that particle and antiparticle modes are related to each other since, e. g.,

$$\Gamma_{\pi^-}^{\prime(0)} = \bar{\Gamma}_{\pi^+}^{\prime(0)}, \quad (7.21)$$

with  $\pi^0$ ,  $\eta_8$ , and  $\eta_0$  being their own antiparticles. These vertices agree with those of the nine Goldstone modes obtained numerically by diagonalizing the polarization function for vanishing quark mass up to an arbitrary phase.

So far, the vertices are only defined at the pole ( $q_0 = 0$ ). In general, the diagonalization procedure leads to four-momentum-dependent vertex functions through the four-momentum-dependent transformation matrix  $U_{ij}(q)$  in Eq. (6.62). It is not possible to derive these  $q$ -dependent vertices directly via the presented Ward-Takahashi identity. However, for the flavored mesons the momentum dependence can be included by introducing a mixing angle  $\varphi(q)$  [22],

$$\Gamma'_{\pi^+}(q) = -i \left( \sin \varphi(q) \Gamma_{57}^{p\uparrow} - \cos \varphi(q) \Gamma_{75}^{p\downarrow} \right), \quad (7.22)$$

illustrated here for the example of the  $\pi^+$  vertex. The overall phase has been chosen to agree with Eq. (7.19). In the chiral limit, the mixing angle  $\varphi(0) = \frac{\pi}{4}$  and  $\Gamma'_j(0) = \Gamma_j^{(0)}$  comply with Eq. (7.19).

### Pion decay constant

In [22], a semianalytical expression for the pion decay constant in the chiral limit has been derived. In the following we will briefly sketch the idea.

The first part of the derivation is valid for all nine Goldstone bosons. Since these are massless in the chiral limit, Eq. (7.4) has to be evaluated for  $m_i = 0$ . In this case, both sides of the equation have to vanish. The pion decay constant is then given by the derivative of Eq. (7.4) with respect to  $q_0$  [22]

$$f_i = -g_i \frac{d}{dq_0} \int \frac{d^4k}{(2\pi)^4} \frac{1}{2} \text{Tr}[\bar{A}_{5i}^0 S(k+q) \Gamma'_i(q) S(k)] \Big|_{q=0}. \quad (7.23)$$

By using  $g_i f_i = \Delta$  (cf. Eq. (7.18)), it is possible to eliminate the coupling constant  $g_i$  and obtain

$$f_i^2 = -\Delta \frac{d}{dq_0} \int \frac{d^4k}{(2\pi)^4} \frac{1}{2} \text{Tr}[\bar{A}_{5i}^0 S(k+q) \Gamma'_i(q) S(k)] \Big|_{q=0}. \quad (7.24)$$

We emphasize that not only the propagator, but also the vertex  $\Gamma'_i$  depends on the momentum  $q$  in Eq. (7.24). Reflecting the fact that the derivative, therefore, acts on the propagator  $S(p+q)$  and on the vertex  $\Gamma'_i(q)$ , it is useful to decompose  $f_\pi^2$  into two parts [22]

$$f_i^2 = \tilde{f}_i^2 + \delta f_i^2, \quad (7.25)$$

where  $\tilde{f}_i^2$  corresponds to the part where the derivative acts on the propagator,

$$\tilde{f}_i^2 = -\Delta \int \frac{d^4k}{(2\pi)^4} \frac{1}{2} \text{Tr} \left[ \bar{A}_{5i}^0 \frac{dS(k+q)}{dq_0} \Big|_{q=0} \Gamma'_i(0) S(k) \right], \quad (7.26)$$

and  $\delta f_i^2$  to the contribution with the derivative acting on the vertex function,

$$\delta f_i^2 = -\Delta \int \frac{d^4k}{(2\pi)^4} \frac{1}{2} \text{Tr} \left[ \bar{A}_{5i}^0 S(k) \frac{d\Gamma'_i(q)}{dq_0} \Big|_{q=0} S(k) \right]. \quad (7.27)$$



The dependence of  $\Gamma'_i$  on  $q_0$  is contained in the transformation matrix  $U$  (see Eq. (6.62)) which describes the mixing of the two relevant vertices ( $\Gamma_{57}^{p\uparrow}$  and  $\Gamma_{75}^{p\downarrow}$  for  $\pi^+$ ):

$$U = \begin{pmatrix} \cos \varphi(q) & -\sin \varphi(q) \\ \sin \varphi(q) & \cos \varphi(q) \end{pmatrix}. \quad (7.28)$$

The derivative is given by [22]

$$\left. \frac{d\Gamma'_i(q)}{dq_0} \right|_{q=0} = \left. \frac{d\varphi}{dq_0} \right|_{q=0} \left. \frac{\partial \Gamma'_i(q)}{\partial \varphi} \right|_{\varphi(q=0)=\frac{\pi}{4}} = \left. \frac{d\varphi}{dq_0} \right|_{q=0} \Gamma'_{i^\perp}, \quad (7.29)$$

where

$$\Gamma'_{i^\perp} \equiv \left. \frac{\partial \Gamma'_i(q)}{\partial \varphi} \right|_{\varphi=\frac{\pi}{4}} \quad (7.30)$$

is the vertex of the orthogonal state with the same quantum numbers as the meson  $i$ , i. e., the corresponding higher-lying mode.

Using Eq. (7.29),  $\delta f_i^2$  is

$$\delta f_i^2 = -\Delta \int \frac{d^4 k}{(2\pi)^4} \frac{1}{2} \text{Tr} [\bar{A}_{i5}^0 S(k+q) \Gamma'_{i^\perp} S(k)] \left. \frac{d\varphi}{dq_0} \right|_{q=0}. \quad (7.31)$$

Inserting the explicit structure of the vertex  $\Gamma'_{i^\perp}$  for the pion and the expression for the quark propagator in the chiral limit (see Appendix B.2),  $\tilde{f}_\pi^2$  and  $\delta f_\pi^2$  can be calculated. The resulting formulas are given in [22]. The expansions of  $\tilde{f}_\pi^2$  and  $\delta f_\pi^2$  for small values of  $\Delta$  are:

$$\tilde{f}_\pi^2 = \frac{\mu^2}{36\pi^2} \{ (21 - 8 \ln 2) - 9y^2 \ln y^2 - c_2 y^2 + \dots \}, \quad (7.32)$$

$$\delta f_\pi^2 = \frac{\mu^2}{36\pi^2} \{ -36y^2 \ln y^2 - d_2 y^2 + \dots \} \mu \left. \frac{d\varphi}{dq_0} \right|_{q=0}, \quad (7.33)$$

with the coefficients

$$c_2 = \frac{81}{4} - 18 \ln 2 - 9 \ln(x^2 - 1) + \frac{45x^2 - 27}{(x^2 - 1)^2}, \quad (7.34)$$

$$d_2 = 102 - 56 \ln 2 - 36 \ln(x^2 - 1) + \frac{36}{x^2 - 1},$$

and the abbreviations

$$x = \frac{\Lambda}{\mu} \quad \text{and} \quad y = \frac{\Delta}{\mu}. \quad (7.35)$$

The derivative of the mixing angle  $\left. \frac{d\varphi}{dq_0} \right|_{q=0}$  has to be evaluated numerically.

It can be directly read off from Eqs. (7.32) and (7.33) that the weak-coupling limit ( $\Delta \rightarrow 0$  and thus  $y \rightarrow 0$ ) of  $f_\pi^2$ , Eq. (6.11), is reproduced by the leading term in  $\tilde{f}_\pi^2$ , while  $\delta f_\pi^2$  does not contribute at this order unless  $\left. \frac{d\varphi}{dq_0} \right|_{q=0}$  diverges stronger than  $y^2 \ln y^2$ .

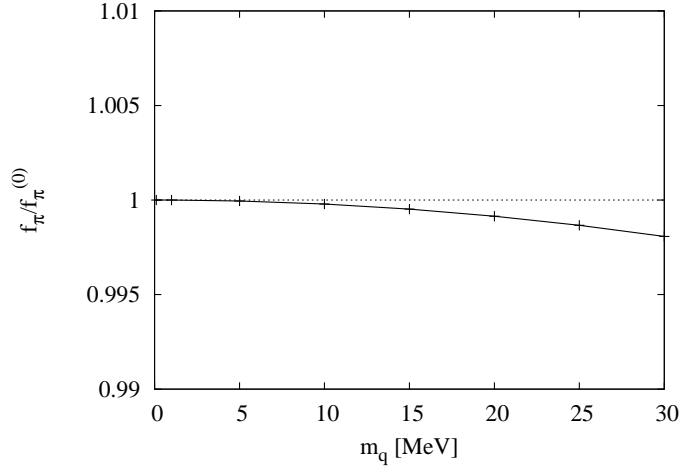


Figure 7.3:  $f_\pi$  divided by its chiral limit value  $f_\pi^{(0)}$  as a function of the quark mass  $m_q$ .

## 7.2 Decay constants in the chiral limit

In the following, we present our results again for  $T = 0$  and a fixed quark chemical potential  $\mu = 500$  MeV. If not stated otherwise, we use a diquark coupling  $H\Lambda^2 = 1.4$  and a cutoff  $\Lambda = 600$  MeV.

### 7.2.1 Goldstone bosons

We will discuss the weak decay constants of the octet and the singlet. Therefore, we take the pion as a representative of the octet and call the octet decay constant  $f_\pi$ . The  $\eta'$  forms the singlet state. We will start with an extensive discussion of the pion decay constant, since it can be compared with the semianalytical formula derived in Sec. 7.1

#### Pion decay constant

In Sec. 7.1, we have explained that we carry out our numerical calculations for the chiral limit at  $m_q = 0.1$  MeV for technical reasons. In order to prove that this is a justified assumption, we show the ratio of  $f_\pi$  and its chiral limit value as a function of the quark mass  $m_q$  in Fig. 7.3. The plot clearly shows that  $f_\pi$  depends only very weakly on the quark mass in the considered range. For  $m_q = 30$  MeV it differs by approximately 0.2% from its chiral limit value. We therefore conclude that  $m_q = 0.1$  MeV is a justified approximation for the chiral limit.

Our results for  $f_\pi$  are displayed in Fig. 7.4 as functions of the gap parameter  $\Delta$ , which is varied by changing the diquark coupling  $H$  for two different values of the cutoff,  $\Lambda =$

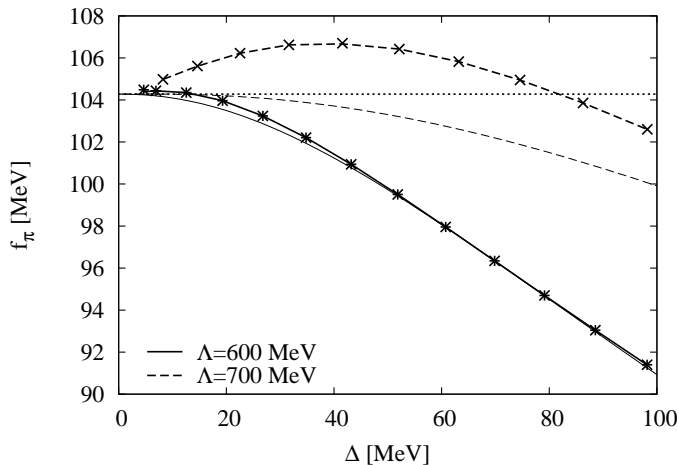


Figure 7.4: Pion decay constant  $f_\pi$  in the chiral limit as a function of the gap parameter  $\Delta$ : numerical results (points) in comparison with the semianalytical formula, Eq. (7.25), neglecting (thin lines) and including (thick lines) the momentum dependence of the vertex function ( $\delta f_\pi^2$ ). Asterisks and solid lines:  $\Lambda = 600$  MeV; crosses and dashed lines:  $\Lambda = 700$  MeV; dotted line: weak-coupling limit, Eq. (6.11).

600 MeV and  $\Lambda = 700$  MeV. The thick lines show the complete expression for  $f_\pi$ , using the exact formulas for  $\tilde{f}_\pi^2$  and  $\delta f_\pi^2$  from [22] with the numerically computed derivative  $d\varphi/dq_0$ . Our results are in perfect agreement with the semianalytical formula, as it should be.

Our results converge to the weak coupling limit of 104.3 MeV for  $\Delta \rightarrow 0$ . For larger diquark couplings we find deviations from this limit on the order of 10% for  $\Lambda = 600$  MeV and  $\Delta \approx 80$  MeV. These deviations depend rather strongly on the cutoff. Inspecting the expansions for  $\tilde{f}_\pi^2$ , Eq. (7.32), and for  $\delta f_\pi^2$ , Eq. (7.33), we see that the leading order term in  $\tilde{f}_\pi^2$  and the terms proportional to  $y^2 \ln y$  do not depend on the cutoff, while the quadratic terms of  $\tilde{f}_\pi^2$  and  $\delta f_\pi^2$  depend on the cutoff via the variable  $x$  in the prefactors. For  $\delta f_\pi^2$ , the situation is more complicated because the derivative  $d\varphi/dq_0$ , reflecting the momentum-dependence of the vertex function, depends on the cutoff as well.

To analyze the influence of the momentum-dependence of the vertex function  $\Gamma'_\pi(q)$ , the thin lines in Fig. 7.4 show the contribution of  $\tilde{f}_\pi^2$  only, i. e., neglecting  $\delta f_\pi^2$ . For  $\Lambda = 600$  MeV this is a good approximation for  $f_\pi$ , and one can only see small deviations for  $\Delta \lesssim 40$  MeV. For  $\Lambda = 700$  MeV, however, the correction term  $\delta f_\pi^2$  is not negligible for the whole range of  $\Delta$ . To explain this behavior, we display the derivative  $d\varphi/dq_0$  in Fig. 7.5. For  $\Lambda = 700$  MeV (dashed line) the factor  $\mu d\varphi/dq_0$  is never small in the shown region. This explains why it cannot be neglected for the description of the

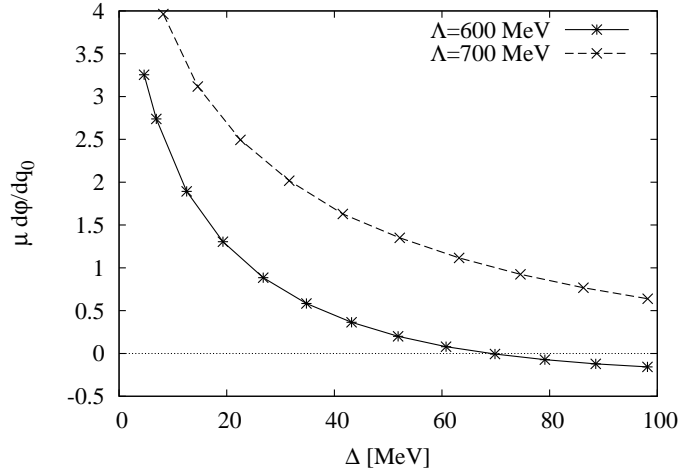


Figure 7.5: Derivative of the mixing angle  $\varphi$  as a function of the gap parameter  $\Delta$ .

numerical results. For  $\Lambda = 600$  MeV, on the other hand,  $\mu d\varphi/dq_0$  is rather small for  $\Delta \gtrsim 40$  MeV, in agreement with our previous findings.

The derivative  $d\varphi/dq_0$  seems to diverge for small values of  $\Delta$ . If it would grow stronger than  $(y^2 \ln y^2)^{-1}$ , this would lead to a leading-order contribution in  $\delta f_\pi^2$  (cf. Eq. (7.33)) and, thus, could affect the weak-coupling limit. However, we verified numerically that  $d\varphi/dq_0$  grows slower than  $(y^2 \ln y^2)^{-1}$ .

### $\eta'$ decay constant

Next, we calculate the  $\eta'$  decay constant. The results are shown in Fig. 7.6, again for the two cutoffs  $\Lambda = 600$  MeV and  $\Lambda = 700$  MeV. We see that the behavior of  $f_{\eta'}$  is very similar to that of  $f_\pi$  (cf. Fig. 7.4). The weak-coupling limit of 97.5 MeV according to Eq. (6.11) (marked by the thin horizontal line in the figure) is approached for  $\Delta \rightarrow 0$ . For higher values of the gap parameter, we find deviations again. For  $\Delta \approx 80$  MeV and  $\Lambda = 600$  MeV, for example, the numerical results are approximately 10% smaller than in the weak-coupling limit.

Of course, it would be possible to perform a similar analysis of  $f_{\eta'}$  as for  $f_\pi$  by deriving a semianalytical formula for this case as well. However, since the behavior of the two decay constants is very similar, no additional insight can be expected from such a procedure.

## 7.2.2 Higher-lying excitations

By using the chiral Ward-Takahashi identities in Sec. 7.1.2, we saw that either the mass  $m_i$  or the product  $g_i f_i$  of a meson  $i$  has to vanish in the chiral limit. Since the

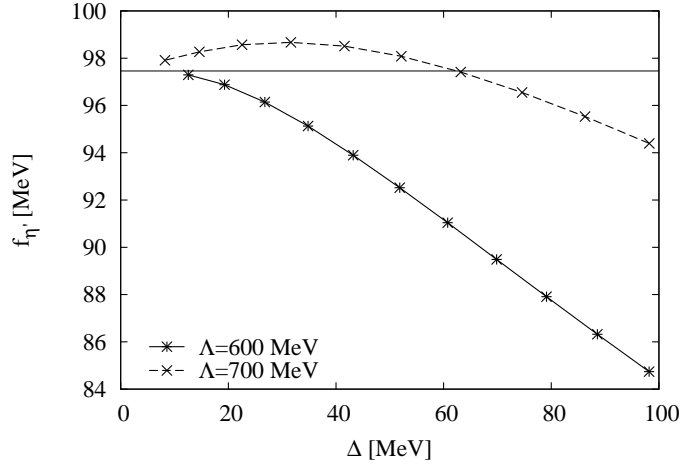


Figure 7.6:  $f_{\eta'}$  in the chiral limit as a function of the gap parameter  $\Delta$  for  $\Lambda = 600$  MeV and  $\Lambda = 700$  MeV. Thin horizontal line: weak-coupling limit. The points are connected by straight lines to guide the eye.

mass of the higher-lying excitations is non-zero, we are forced to check whether the decay constants are vanishing in the chiral limit. To this end, the decay constant of the higher-lying octet modes is shown in Fig. 7.7 as a function of the squared quark mass  $m_q^2$ .

We find that the numerical results are very well described by a linear curve, implying that  $f_\pi$  behaves like  $m_q^2$  and that it goes to zero in the chiral limit, as expected. Moreover, even for  $m_q \neq 0$ , it is several orders of magnitude smaller than the decay constant of the Goldstone bosons (cf. Fig 7.4).

### 7.3 Low-energy constant $A$

After having calculated the weak decay constants, we come back to the deviations in the slopes  $a$  of the mass functions in the Sec. 6.4. The weak-coupling predictions for  $a$ , Eq. (6.72), lead to the condition

$$\frac{a_{\text{singlet}}}{a_{\text{octet}}} = \frac{f_\pi^2}{f_{\eta'}^2}. \quad (7.36)$$

Since our results satisfy this relation with deviations below 1%, we conclude that we also have one single factor  $A$  for the singlet and the octet. We calculate  $A_{\text{NJL}}$  by solving Eq. (6.72) for the octet and obtain

$$A_{\text{NJL}} = \frac{a^2 f_\pi^2}{8}. \quad (7.37)$$

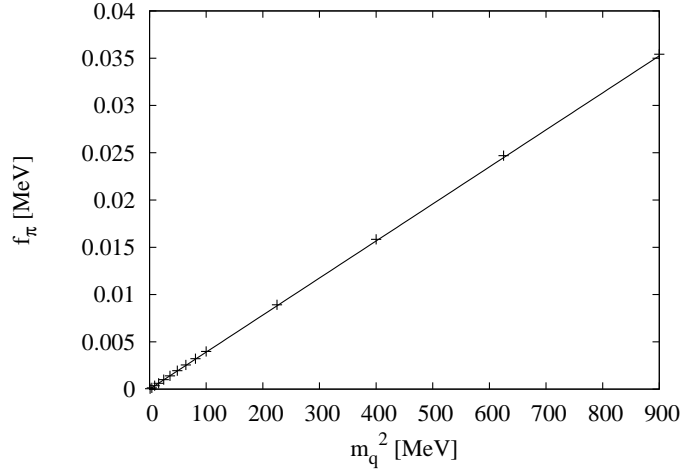


Figure 7.7: Decay constant of the higher-lying octet modes as a function of the squared quark mass  $m_q^2$ . The points indicate the numerical results. The solid line is a linear fit.

In Fig. 7.8 we display the ratio of the numerical  $A_{\text{NJL}}$  and  $A_{\text{wc}}$  as a function of the gap parameter  $\Delta$ .

The NJL values differ significantly from the weak-coupling result. While it is larger for small values of  $\Delta$ , it is approximately 60% smaller than the weak-coupling results at  $\Delta \approx 80$  MeV, resulting in the smaller Goldstone boson masses compared to the weak-coupling predictions. In [22] an analytic expression for  $A_{\text{NJL}}$  has been derived which perfectly fits the numerical results.

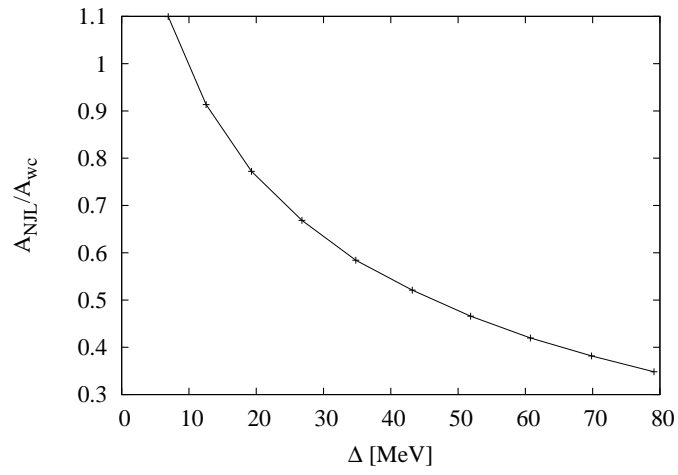


Figure 7.8: Low-energy constant  $A_{\text{NJL}}$  extracted from the numerical calculation in comparison with the weak-coupling value  $A_{\text{wc}}$ . The points are connected by straight lines to guide the eye.





## 8 Summary

In this thesis we have studied several aspects of color superconductivity in the regime of a few times nuclear matter density, which is relevant for the physics of neutron stars. To that end, a Nambu–Jona-Lasinio (NJL) model has been used. This effective model shares the symmetries of QCD and can also be employed to examine color superconductivity. For calculations at moderate densities, one has to rely on effective models since neither lattice calculations nor perturbative treatments are applicable. Recently, functional Dyson-Schwinger studies of color superconductivity have come up [90, 80]. This method, although very promising, is technically very involved and no attempts to calculate a phase diagram have been made so far.

Due to the high temperatures obtained in heavy-ion collisions, it does not seem to be possible to generate the conditions of color superconductivity experimentally. The only places where color superconductivity might occur are the cores of neutron stars. Therefore, results of calculations concerning color superconductivity should be examined for possible astrophysical consequences which are accessible by astronomical observations.

In the first part of this work, phase diagrams of locally neutral quark matter were investigated. The focus of this study were the implications of dynamically generated constituent quark masses, calculated self-consistently on the same footing as the diquark pairing. This is of special interest, because on the one hand, the actual values of the quark masses influence the competition between the different phases, and the phases themselves determine the magnitude of the masses on the other hand.

The effects of the dynamical quark masses on the phase structure were studied in Chapter 4. Since the value of the diquark coupling is only imprecisely known, we have calculated the phase diagram for two different couplings. To simulate the conditions in neutron stars, these calculations were performed for neutral quark matter in  $\beta$  equilibrium. It turned out that the interplay of the neutrality constraint and the dynamically generated quark masses produces an interesting phase structure, especially for the weaker coupling. While the color-flavor locked (CFL) phase is favored at high chemical potentials, and the phase with broken chiral symmetry and large constituent quark masses at small chemical potentials, the region of intermediate densities and low temperature is governed by unpaired quark matter with restored chiral symmetry. The masses of the up and down quarks are already quite small in this region. However, charge neutrality requires approximately twice as many down quarks in the system as up quarks. Therefore, their Fermi momenta are separated too far to allow the formation of a diquark condensate. The condensate can only be formed at

higher temperatures where the Fermi surfaces of up and down quarks are sufficiently smeared. Such a thermal enhancement of color superconductivity is an interesting feature, because without requiring neutrality, an increasing temperature only spoils the formation of a diquark condensate.

For a stronger diquark coupling, the two-flavor color superconducting (2SC) phase is preferred at intermediate chemical potentials, because the increased coupling strength can overcome the splitting of the Fermi surfaces. In addition, it results in an enlargement of the color superconducting regions to smaller chemical potentials and larger temperatures.

In the phase diagrams, we have identified regions of so-called gapless phases, where the gap in the excitation spectra of some quasiparticles vanishes. Since these phases are known to be unstable, one has to study other pairing scenarios like crystalline or mixed phases to find the true ground state.

In Chapter 5, we have extended our considerations to the case of neutrino trapping, which is relevant for the physics of protoneutron stars, i. e., the hot remnants of supernova explosions. Lepton-number conservation requires a positive lepton-number chemical potential, which provides extra electrons without inducing a large mismatch between the Fermi momenta of up and down quarks. This enables the pairing of these quarks and the formation of the 2SC phase, which suffers from the neutrality constraint if no electrons are present. For the CFL phase, however, the situation is reversed. Since it is neutral without any electrons, the lepton-number chemical potential puts a stress on the pairing. Thus, neutrino trapping leads to a shrinking of the CFL phase and a growth of the 2SC phase. These findings suggest that the CFL phase is very unlikely to appear in a protoneutron star before the deleptonization is complete.

In the second part of this thesis, we concentrated on the CFL phase. There, the quarks pair in a particularly symmetric way which results in a special symmetry-breaking pattern and in the appearance of nine pseudoscalar Goldstone bosons: eight of them due to chiral symmetry breaking, and one due to the breaking of the  $U(1)_A$  symmetry. Since all quarks participate in the pairing in the CFL phase, all fermionic quasiparticles are gapped and the Goldstone bosons are the lowest-lying excitations relevant for the thermodynamics of the system.

We have constructed the Goldstone bosons explicitly by solving the Bethe-Salpeter equation for quark-quark scattering in random phase approximation. Such an approach of explicitly constructing the Goldstone bosons in the CFL phase had previously only been performed in the chiral limit. Since we have only included quark-quark interactions, our Goldstone boson states are in fact superpositions of diquark and di-hole states.

Our main motivation to study the Goldstone bosons in the CFL phase was a comparison with results obtained in the low-energy effective theory (LEET) in the weak-coupling limit. In this way, we were able to check the weak-coupling limit of our model calculations on the one hand, and obtain informations about the range of validity of

---

the weak-coupling LEET predictions on the other hand.

In Chapter 6, the masses of the Goldstone bosons for equal and unequal quark masses were calculated. In the first case, we found an octet of Goldstone bosons and a singlet. The masses of the Goldstone bosons depend linearly on the quark mass, in agreement with the predictions of the LEET. However, the corresponding coefficients do not agree with the weak-coupling results. For larger gap parameters  $\Delta$ , we found considerably smaller meson masses than predicted by the weak-coupling-formulas.

For unequal quark masses, the meson masses and meson chemical potentials are in good agreement with the LEET as well, if our model results are used for low-energy constants instead of the weak-coupling values. We have confirmed an inverse meson mass ordering, with the kaons being lighter than the pions. For large values of the strange quark mass, the predicted kaon condensation occurs. However, we found a qualitative difference for vanishing light quark masses, where we obtained a non-zero critical strange quark mass for the onset of kaon condensation, while the LEET in leading order in the quark masses predicts a vanishing critical strange quark mass. This can be understood as a higher-order effect on the kaon mass which is only noticeable for very small light quark masses.

The weak decay constants were examined in Chapter 7. The weak-coupling limit is correctly reproduced at zeroth order in the gap parameter. This should be the case, since the leading order results of the LEET are universal in the sense that they should hold in any model exhibiting the same symmetries. However, we found deviations on the order of 10% from the weak-coupling results for gap parameters around 80 MeV.

Aside from the Goldstone bosons, there are higher-lying excitations in the CFL phase, which were studied as well. Our calculations revealed that the octet states are weakly bound, while the singlet state is unbound. Finally, the decay constants of the higher-lying modes were found to vanish in the chiral limit. This is in agreement with a prediction obtained from axial Ward-Takahashi identities.

Summing up this last part, we found qualitative agreement with the LEET predictions for masses and chemical potentials of the Goldstone bosons in the CFL phase. Quantitatively, our meson masses differ from the predictions obtained in the weak-coupling limit by more than 30% for gap parameters of 80 MeV. This reflects the fact that the weak-coupling assumption is certainly not valid in that region. While the LEET itself is still valid, the corresponding low-energy constants, which are obtained in the weak-coupling limit, are questionable.

There are several open issues in the study of the Goldstone bosons: The inclusion of quark-antiquark interactions, which could give corrections to the masses of the Goldstone bosons, is a natural next step. Furthermore, the inclusion of instanton effects is worth considering since its importance has been pointed out in [91, 92]. The ultimate goal would be to include the backreaction of the Goldstone bosons on the phase structure of superconducting quark matter, and to calculate a phase diagram in such a refined scenario. It would also be interesting to calculate the Goldstone bosons for a CFL phase with neutrino trapping, to see whether a condensation of positively

charged Goldstone bosons could reduce the stress on the CFL phase.

In addition to these extensions of the model, it would be useful to examine the field from the other direction and to work out the observable astrophysical consequences in detail. While it will certainly be difficult to prove that a specific scenario is realized, it might be possible to exclude some.

# A Conventions

Calculations are done in natural units

$$\hbar = c = k_B = 1 .$$

The metric tensor is

$$g = \text{diag}(1, -1, -1, -1) .$$

For the  $\gamma$  matrices we use the Dirac representation

$$\gamma^0 = \begin{pmatrix} 1 & 0 & 0 & 0 \\ 0 & 1 & 0 & 0 \\ 0 & 0 & -1 & 0 \\ 0 & 0 & 0 & -1 \end{pmatrix}, \quad \gamma^1 = \begin{pmatrix} 0 & 0 & 0 & 1 \\ 0 & 0 & 1 & 0 \\ 0 & -1 & 0 & 0 \\ -1 & 0 & 0 & 0 \end{pmatrix}, \quad (\text{A.1})$$

$$\gamma^2 = \begin{pmatrix} 0 & 0 & 0 & -i \\ 0 & 0 & i & 0 \\ 0 & i & 0 & 0 \\ -i & 0 & 0 & 0 \end{pmatrix}, \quad \gamma^3 = \begin{pmatrix} 0 & 0 & 1 & 0 \\ 0 & 0 & 0 & -1 \\ -1 & 0 & 0 & 0 \\ 0 & 1 & 0 & 0 \end{pmatrix}, \quad (\text{A.2})$$

$$\gamma^5 = \begin{pmatrix} 0 & 0 & 1 & 0 \\ 0 & 0 & 0 & 1 \\ 1 & 0 & 0 & 0 \\ 0 & 1 & 0 & 0 \end{pmatrix}. \quad (\text{A.3})$$

They satisfy the anticommutator relation

$$\gamma^\mu \gamma^\nu + \gamma^\nu \gamma^\mu = 2g^{\mu\nu} .$$

The  $\gamma$ -matrices are traceless and all traces over products with odd numbers of  $\gamma$ -matrices vanish [93].

We often use the Gell-Mann matrices

$$\lambda_1 = \begin{pmatrix} 0 & 1 & 0 \\ 1 & 0 & 0 \\ 0 & 0 & 0 \end{pmatrix}, \quad \lambda_2 = \begin{pmatrix} 0 & -i & 0 \\ i & 0 & 0 \\ 0 & 0 & 0 \end{pmatrix}, \quad \lambda_3 = \begin{pmatrix} 1 & 0 & 0 \\ 0 & -1 & 0 \\ 0 & 0 & 0 \end{pmatrix}, \quad (\text{A.4})$$

$$\lambda_4 = \begin{pmatrix} 0 & 0 & 1 \\ 0 & 0 & 0 \\ 1 & 0 & 0 \end{pmatrix}, \quad \lambda_5 = \begin{pmatrix} 0 & 0 & -i \\ 0 & 0 & 0 \\ i & 0 & 0 \end{pmatrix}, \quad \lambda_6 = \begin{pmatrix} 0 & 0 & 0 \\ 0 & 0 & 1 \\ 0 & 1 & 0 \end{pmatrix}, \quad (\text{A.5})$$

$$\lambda_7 = \begin{pmatrix} 0 & 0 & 0 \\ 0 & 0 & -i \\ 0 & i & 0 \end{pmatrix}, \quad \lambda_8 = \frac{1}{\sqrt{3}} \begin{pmatrix} 1 & 0 & 0 \\ 0 & 1 & 0 \\ 0 & 0 & -2 \end{pmatrix}, \quad \lambda_0 = \sqrt{\frac{2}{3}} \begin{pmatrix} 1 & 0 & 0 \\ 0 & 1 & 0 \\ 0 & 0 & 1 \end{pmatrix}. \quad (\text{A.6})$$

which are normalized to

$$\text{Tr}(\lambda_a \lambda_b) = 2\delta_{ab}. \quad (\text{A.7})$$

$T_a = \frac{\lambda_a}{2}$  with  $a = 1, \dots, 8$  are the generators of the SU(3) group.

# B Dressed quark propagator

## B.1 Diagonalization of the (inverse) dressed propagator

The dressed quark propagator  $S(p)$  is the inverse of the inverse quark propagator defined in Eq. (3.25) for the calculation of the phase diagrams and in Eq. (6.25) for the computation of the bosonic properties. Following standard methods (see, e.g., Refs. [64, 20, 94, 89]), we can split the inverse propagator in two pieces

$$S^{-1} \equiv S^{-1}(p^0, \vec{p}) = \gamma_0(p^0 - A(\vec{p})). \quad (\text{B.1})$$

$A(\vec{p})$  is a hermitian  $72 \times 72$  matrix, which does not depend on  $p^0$ . One can find a unitary matrix  $U(\vec{p})$  that diagonalizes  $A(\vec{p})$

$$A(\vec{p}) = U(\vec{p})D(\vec{p})U^\dagger(\vec{p}) \quad (\text{B.2})$$

with the diagonal matrix

$$D(\vec{p}) = \begin{pmatrix} \varepsilon_1(\vec{p}) & & \\ & \ddots & \\ & & \varepsilon_{72}(\vec{p}) \end{pmatrix} \quad (\text{B.3})$$

of the eigenvalues  $\varepsilon_1, \dots, \varepsilon_{72}$  which depend on the three-momentum  $\vec{p}$ . The computation of the eigenvalues becomes simpler by previously bringing  $A$  into a block-diagonal form by reordering lines and columns. Choosing  $\vec{p} = p\vec{e}_3$ ,  $A$  can be decomposed into twelve  $4 \times 4$  and two  $12 \times 12$  blocks. We will diagonalize these blocks numerically.

Combining Eqs. (B.1)-(B.3), the inverse propagator is given by

$$S^{-1}(p) = \gamma_0 U(\vec{p}) \begin{pmatrix} p_0 - \varepsilon_1(\vec{p}) & & \\ & \ddots & \\ & & p_0 - \varepsilon_{72}(\vec{p}) \end{pmatrix} U^\dagger(\vec{p}). \quad (\text{B.4})$$

Starting from the above equation, the inversion is trivial and we obtain

$$S = U(\vec{p}) \begin{pmatrix} \frac{1}{p_0 - \varepsilon_1(\vec{p})} & & \\ & \ddots & \\ & & \frac{1}{p_0 - \varepsilon_{72}(\vec{p})} \end{pmatrix} U^\dagger(\vec{p}) \gamma_0. \quad (\text{B.5})$$

Each eigenvalue  $\varepsilon_i$  is twofold degenerate and for each positive eigenvalue  $\varepsilon_i$  exists a negative one of the same magnitude,  $\varepsilon_j = -\varepsilon_i$ .

## B.2 Dressed propagator for equal quark masses

In the limit of an exact  $SU(3)$  symmetry, we can give a closed expression for the quark propagator. Straight forward inversion of Eq. (6.25) for  $m_u = m_d = m_s = m$  and  $\Delta_{22} = \Delta_{55} = \Delta_{77} = \Delta$  yields

$$S = \begin{pmatrix} S_{11} & S_{12} \\ S_{21} & S_{22} \end{pmatrix}, \quad (\text{B.6})$$

with

$$S_{21} = \Delta^* \frac{\not{p}_- + m}{x_-} \gamma_5 \sum_{A=2,5,7} \tau_A \lambda_A S_{11} \quad (\text{B.7})$$

and

$$S_{11} = \left[ \not{p}_+ - m - \frac{|\Delta|^2}{x_-} (\not{p}_- - m) \sum_{A,A'=2,5,7} \tau_A \tau_{A'} \lambda_A \lambda_{A'} \right]^{-1}, \quad (\text{B.8})$$

where we have introduced the notations

$$\not{p}_\pm = \not{p} \pm \mu \gamma^0, \quad x_\pm = p_\pm^2 - m^2. \quad (\text{B.9})$$

$S_{22}$  and  $S_{12}$  are obtained from  $S_{11}$  and  $S_{21}$ , respectively, under the exchange  $\mu \leftrightarrow -\mu$  and  $\Delta \leftrightarrow -\Delta^*$ .

The matrices  $S_{ij}$  are  $36 \times 36$  matrices representing the normal ( $i = j$ ) and anomalous ( $i \neq j$ ) Nambu-Gorkov components of  $S$ .  $S_{11}$  can explicitly be written as

$$S_{11} = S_- + \frac{1}{6} (T_- - S_-) \sum_{a=0}^8 \tau_a \lambda_a, \quad (\text{B.10})$$

with

$$S_\pm = \frac{x_\pm (\not{p}_\mp + m) - |\Delta|^2 (\not{p}_\pm + m)}{(p_0^2 - E_8^-)(p_0^2 - E_8^+)}, \quad (\text{B.11})$$

corresponding to the eigenvalue  $\Delta$  of the gap matrix, and

$$T_\pm = \frac{x_\pm (\not{p}_\mp + m) - 4|\Delta|^2 (\not{p}_\pm + m)}{(p_0^2 - E_1^-)(p_0^2 - E_1^+)}, \quad (\text{B.12})$$

corresponding to the eigenvalue  $2\Delta$  of the gap matrix. The octet and singlet dispersion relations for particles ( $-$ ) and antiparticles ( $+$ ) are given by

$$E_8^\mp = \sqrt{(\sqrt{p^2 + m^2} \mp \mu)^2 + |\Delta|^2} \quad (\text{B.13})$$

and

$$E_1^\mp = \sqrt{(\sqrt{p^2 + m^2} \mp \mu)^2 + 4|\Delta|^2}, \quad (\text{B.14})$$

respectively.



# C Numerical calculation of some loops

## C.1 Polarization function or similar loop

We often need to calculate the polarization function or some other loop of the structure shown in Fig. C.1. To this end, we show the calculation here.

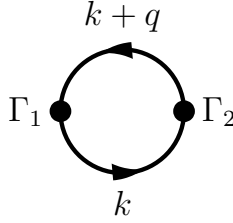


Figure C.1: Loop connecting the two vertices  $\Gamma_1$  and  $\Gamma_2$  in Nambu-Gorkov space.

The loop in Fig. C.1 is given by

$$-iJ_{\Gamma_1\Gamma_2}(q) = - \int \frac{d^4k}{(2\pi)^4} \frac{1}{2} \text{Tr}[\Gamma_1 iS(k+q)\Gamma_2 iS(k)]. \quad (\text{C.1})$$

Diagonalization of the propagators then leads to

$$-iJ_{\Gamma_1\Gamma_2}(q) = \int \frac{d^4k}{(2\pi)^4} \frac{1}{2} \text{Tr}[\Gamma_1 U(\vec{k})S_{\text{diag}}(k+q)U^\dagger(\vec{k})\gamma_0\Gamma_2 U(\vec{k})S(k)_{\text{diag}}U^\dagger(\vec{k})\gamma_0] \quad (\text{C.2})$$

$$= \int \frac{d^4k}{(2\pi)^4} \frac{1}{2} \text{Tr}[\tilde{\Gamma}_1(\vec{k})S_{\text{diag}}(k+q)\tilde{\Gamma}_2(\vec{k})S(k)_{\text{diag}}] \quad (\text{C.3})$$

with  $\tilde{\Gamma}_i(\vec{k}) = \gamma_0 U^\dagger(\vec{k})\Gamma_i U(\vec{k})$ . For the sake of readability, we will leave out the argument  $\vec{k}$  in the following and only keep in mind, that the vertices depend on the

three-momentum  $\vec{k}$ . Performing the trace then leads to

$$-iJ_{\Gamma_1\Gamma_2}(q) = \int \frac{d^4k}{(2\pi)^4} \frac{1}{2} (\tilde{\Gamma}_1)_{ij} (S_{\text{diag}}(k+q))_{jk} (\tilde{\Gamma}_2)_{kl} (S(k)_{\text{diag}})_{li} \quad (\text{C.4})$$

$$= \int \frac{d^4k}{(2\pi)^4} \frac{1}{2} (\tilde{\Gamma}_1)_{ij} (S_{\text{diag}}(k+q))_{jj} (\tilde{\Gamma}_2)_{ji} (S(k)_{\text{diag}})_{ii} \quad (\text{C.5})$$

$$= \int \frac{d^4k}{(2\pi)^4} \frac{1}{2} (\tilde{\Gamma}_1)_{ij} \frac{1}{k_0 + q_0 - \varepsilon_j(\vec{k} + \vec{q})} (\tilde{\Gamma}_2)_{ji} \frac{1}{k_0 - \varepsilon_i(\vec{k})}. \quad (\text{C.6})$$

Since  $\vec{q} = 0$ , the eigenvalues  $\varepsilon_i$  and  $\varepsilon_j$  both depend only on  $\vec{k}$ , and we will skip this argument as well in the following. Applying Matsubara formalism gives

$$-iJ_{\Gamma_1\Gamma_2}(i\omega_m) = \frac{i}{2} T \sum_n \int \frac{d^3k}{(2\pi)^3} (\tilde{\Gamma}_1)_{ij} (\tilde{\Gamma}_2)_{ji} \frac{1}{i\omega_n + i\omega_m - \varepsilon_j} \frac{1}{i\omega_n - \varepsilon_i} \quad (\text{C.7})$$

with the fermionic and bosonic Matsubara frequencies  $i\omega_n = (2n+1)\pi T$  and  $i\omega_m = 2m\pi T$ . The sum over  $n$  can be transformed into a circular integral by using the residue theorem

$$-iJ_{\Gamma_1\Gamma_2}(i\omega_m) = -\frac{1}{4\pi} \oint dz \frac{d^3k}{(2\pi)^3} (\tilde{\Gamma}_1)_{ij} (\tilde{\Gamma}_2)_{ji} \frac{1}{z + q_0 - \varepsilon_j} \frac{1}{z - \varepsilon_i} \left( \exp\left(\frac{z}{T} + 1\right) \right)^{-1}. \quad (\text{C.8})$$

For poles of first order ( $\varepsilon_j - q_0 \neq \varepsilon_i$ ) the circular integral can be evaluated by the residue theorem to

$$\begin{aligned} A &:= \frac{1}{2\pi} \oint dz (\tilde{\Gamma}_1)_{ij} (\tilde{\Gamma}_2)_{ji} \frac{1}{z + q_0 - \varepsilon_j} \frac{1}{z - \varepsilon_i} \exp\left(-\frac{z}{T} - 1\right) \\ &= -i(\tilde{\Gamma}_1)_{ij} (\tilde{\Gamma}_2)_{ji} \left\{ \frac{1}{\varepsilon_j - \varepsilon_i - q_0} \exp\left(-\frac{\varepsilon_j}{T} - 1\right) \right. \\ &\quad \left. + \frac{1}{\varepsilon_i - \varepsilon_j + q_0} \exp\left(-\frac{\varepsilon_i}{T} - 1\right) \right\}, \end{aligned} \quad (\text{C.9})$$

while the poles of second order ( $\varepsilon_j - q_0 = \varepsilon_i$ ) lead to

$$\begin{aligned} B &:= \frac{1}{2\pi} \oint dz (\tilde{\Gamma}_1)_{ij} (\tilde{\Gamma}_2)_{ji} \frac{1}{z + q_0 - \varepsilon_j} \frac{1}{z - \varepsilon_i} \exp\left(-\frac{z}{T} - 1\right) \\ &= -i(\tilde{\Gamma}_1)_{ij} (\tilde{\Gamma}_2)_{ji} \frac{1}{T} \left( \exp\left(\frac{\varepsilon_i}{T}\right) + \exp\left(-\frac{\varepsilon_i}{T}\right) + 2 \right)^{-1} \end{aligned} \quad (\text{C.10})$$

Combining these expressions

$$-iJ_{\Gamma_1\Gamma_2}(q) = -\frac{1}{2} \int \frac{d^3k}{(2\pi)^3} \{A(1 - \delta(\varepsilon_j - \varepsilon_i - q_0)) + B\delta(\varepsilon_j - \varepsilon_i - q_0)\} \quad (\text{C.11})$$

and finally using  $\vec{k} = k\vec{e}_3$ , leads to

$$-iJ_{\Gamma_1\Gamma_2}(q) = -\frac{1}{a\pi^2} \int dk k^2 \{A(1 - \delta(\varepsilon_j - \varepsilon_i - q_0)) + B\delta(\varepsilon_j - \varepsilon_i - q_0)\}. \quad (\text{C.12})$$

In the zero temperature limit,  $B$  vanishes and  $A$  simplifies to

$$\lim_{T \rightarrow 0} A = -i(\tilde{\Gamma}_1)_{ij}(\tilde{\Gamma}_2)_{ji} \frac{1}{\varepsilon_j - \varepsilon_i - q_0} (\theta(q_0 - \varepsilon_j) - \theta(-\varepsilon_i)). \quad (\text{C.13})$$

The momentum integration in Eq. (C.12) can then be carried out numerically.

## C.2 Derivative of the polarization function

For the numerical calculation of the pion decay constant in Sec. 7.1.1, we need the derivative of the polarization function as well.

Starting with the expression in Eq. (C.8), the derivative is given by

$$\frac{\partial J_{\Gamma_1\Gamma_2}(q)}{\partial q_0} = -i \frac{1}{4\pi} \oint dz \frac{d^3k}{(2\pi)^3} (\tilde{\Gamma}_1)_{ij}(\tilde{\Gamma}_2)_{ji} \frac{1}{(z + q_0 - \varepsilon_j)^2} \frac{1}{z - \varepsilon_i} \left( \exp\left(\frac{z}{T} + 1\right) \right)^{-1}. \quad (\text{C.14})$$

Depending on the values of  $q_0$ ,  $\varepsilon_i$ , and  $\varepsilon_j$  this expression has either one pole of first order and one pole of second order or one pole of third order. The first case is obtained for  $\varepsilon_j - q_0 \neq \varepsilon_i$  and can be evaluated to

$$\begin{aligned} C &:= \frac{i}{2\pi} \oint dz (\tilde{\Gamma}_1)_{ij}(\tilde{\Gamma}_2)_{ji} \frac{1}{(i\omega_n + i\omega_m - \varepsilon_j)^2} \frac{1}{i\omega_n - \varepsilon_i} \\ &= (\tilde{\Gamma}_1)_{ij}(\tilde{\Gamma}_2)_{ji} \left\{ \frac{1}{(\varepsilon_i - \varepsilon_j + q_0)^2} \left( \left( \exp\left(\frac{\varepsilon_i}{T} + 1\right) + 1 \right)^{-1} \left( \exp\left(\frac{\varepsilon_j}{T} + 1\right) + 1 \right)^{-1} \right) \right. \\ &\quad \left. - \frac{1}{T} \frac{1}{\varepsilon_j - \varepsilon_i - q_0} \left( \exp\left(\frac{\varepsilon_j}{T} + 1\right) + \exp\left(-\frac{\varepsilon_j}{T} + 1\right) + 2 \right)^{-1} \right\} \end{aligned} \quad (\text{C.15})$$

and the second case,  $\varepsilon_j - q_0 = \varepsilon_i$ , can be computed to

$$\begin{aligned} D &:= \frac{i}{2\pi} \oint dz (\tilde{\Gamma}_1)_{ij}(\tilde{\Gamma}_2)_{ji} \frac{1}{(i\omega_n + i\omega_m - \varepsilon_j)^2} \frac{1}{i\omega_n - \varepsilon_i} \\ &= \frac{1}{2T^2} \left( \exp\left(\frac{\varepsilon_i}{T} + 1\right) + \exp\left(-\frac{\varepsilon_i}{T} + 1\right) + 2 \right)^{-1} \left( 2 \left( \exp\left(-\frac{\varepsilon_i}{T} + 1\right) + 1 \right)^{-1} - 1 \right). \end{aligned} \quad (\text{C.16})$$

Putting these formulas together and using  $\vec{k} = k\vec{e}_3$  again, yields

$$\frac{\partial J_{\Gamma_1\Gamma_2}(q)}{\partial q_0} = \frac{1}{4\pi^2} \int dk k^2 (C(1 - \delta(\varepsilon_i - \varepsilon_j + q_0)) + D\delta(\varepsilon_i - \varepsilon_j + q_0)). \quad (\text{C.17})$$

In the zero temperature limit,  $D$  vanishes and  $C$  simplifies to

$$\lim_{T \rightarrow 0} C = \frac{1}{(\varepsilon_i - \varepsilon_j + q_0)^2} (\theta(-\varepsilon_i) - \theta(-\varepsilon_j)). \quad (\text{C.18})$$



# Bibliography

- [1] M. Gell-Mann, Phys. Lett. **8**, 214 (1964).
- [2] G. Zweig, CERN-TH-401.
- [3] D. J. Gross and F. Wilczek, Phys. Rev. Lett. **30**, 1343 (1973).
- [4] H. D. Politzer, Phys. Rev. Lett. **30**, 1346 (1973).
- [5] Y. Nambu, Phys. Rev. Lett. **4**, 380 (1960).
- [6] J. C. Collins and M. J. Perry, Phys. Rev. Lett. **34**, 1353 (1975).
- [7] N. Cabibbo and G. Parisi, Phys. Lett. **B59**, 67 (1975).
- [8] O. Philipsen, Eur. Phys. J. ST **152**, 29 (2007), 0708.1293.
- [9] S. B. Ruster, I. A. Shovkovy, and D. H. Rischke, Nucl. Phys. **A743**, 127 (2004), hep-ph/0405170.
- [10] K. Fukushima, C. Kouvaris, and K. Rajagopal, Phys. Rev. **D71**, 034002 (2005), hep-ph/0408322.
- [11] I. A. Shovkovy, S. B. Ruster, and D. H. Rischke, J. Phys. **G31**, S849 (2005), nucl-th/0411040.
- [12] M. G. Alford, K. Rajagopal, and F. Wilczek, Nucl. Phys. **B537**, 443 (1999), hep-ph/9804403.
- [13] I. A. Shovkovy and P. J. Ellis, Phys. Rev. **C66**, 015802 (2002), hep-ph/0204132.
- [14] M. G. Alford, M. Braby, S. Reddy, and T. Schäfer, Phys. Rev. **C75**, 055209 (2007), nucl-th/0701067.
- [15] M. Buballa, Phys. Lett. **B609**, 57 (2005), hep-ph/0410397.
- [16] M. M. Forbes, Phys. Rev. **D72**, 094032 (2005), hep-ph/0411001.
- [17] H. J. Warringa, hep-ph/0606063.
- [18] D. Ebert and K. G. Klimenko, Phys. Rev. **D75**, 045005 (2007), hep-ph/0611385.

- [19] D. Ebert, K. G. Klimenko, and V. L. Yudichev, *Eur. Phys. J.* **C53**, 65 (2008), [arXiv:0705.2666 \[hep-ph\]](#).
- [20] S. B. Rüster, V. Werth, M. Buballa, I. A. Shovkovy, and D. H. Rischke, *Phys. Rev.* **D72**, 034004 (2005), [hep-ph/0503184](#).
- [21] S. B. Rüster, V. Werth, M. Buballa, I. A. Shovkovy, and D. H. Rischke, *Phys. Rev.* **D73**, 034025 (2006), [hep-ph/0509073](#).
- [22] V. Kleinhaus, M. Buballa, D. Nickel, and M. Oertel, *Phys. Rev.* **D76**, 074024 (2007), [arXiv:0707.0632 \[hep-ph\]](#).
- [23] V. Kleinhaus and M. Buballa, [0808.3490](#).
- [24] B. C. Barrois, *Nucl. Phys.* **B129**, 390 (1977).
- [25] S. C. Frautschi (1978), presented at Workshop on Hadronic Matter at Extreme Energy Density, Erice, Italy, Oct 13-21, 1978.
- [26] D. Bailin and A. Love, *Phys. Rept.* **107**, 325 (1984).
- [27] M. G. Alford, K. Rajagopal, and F. Wilczek, *Phys. Lett.* **B422**, 247 (1998), [hep-ph/9711395](#).
- [28] R. Rapp, T. Schäfer, E. V. Shuryak, and M. Velkovsky, *Phys. Rev. Lett.* **81**, 53 (1998), [hep-ph/9711396](#).
- [29] A. L. Fetter and J. D. Walecka, *Quantum Theory of Many-Particle Systems* (Dover Publications, 2003), ISBN 0486428273.
- [30] K. Rajagopal and F. Wilczek, [hep-ph/0011333](#).
- [31] M. G. Alford, *Ann. Rev. Nucl. Part. Sci.* **51**, 131 (2001), [hep-ph/0102047](#).
- [32] D. H. Rischke, *Prog. Part. Nucl. Phys.* **52**, 197 (2004), [nucl-th/0305030](#).
- [33] M. Buballa, *Phys. Rept.* **407**, 205 (2005), [hep-ph/0402234](#).
- [34] I. A. Shovkovy, *Found. Phys.* **35**, 1309 (2005), [nucl-th/0410091](#).
- [35] M. G. Alford, A. Schmitt, K. Rajagopal, and T. Schäfer, *Rev. Mod. Phys.* **80**, 1455 (2008), [0709.4635](#).
- [36] J. Bardeen, L. N. Cooper, and J. R. Schrieffer, *Phys. Rev.* **106**, 162 (1957).
- [37] J. Goldstone, A. Salam, and S. Weinberg, *Phys. Rev.* **127**, 965 (1962).
- [38] P. W. Anderson, *Phys. Rev.* **130**, 439 (1963).

- [39] P. W. Higgs, Phys. Rev. Lett. **13**, 508 (1964).
- [40] N. Iwamoto, Phys. Rev. Lett. **44**, 1637 (1980).
- [41] R. D. Pisarski and D. H. Rischke, nucl-th/9907094.
- [42] I. A. Shovkovy and L. C. R. Wijewardhana, Phys. Lett. **B470**, 189 (1999), hep-ph/9910225.
- [43] T. Schäfer, Nucl. Phys. **B575**, 269 (2000), hep-ph/9909574.
- [44] D. Bailin and A. Love, Nucl. Phys. **B190**, 751 (1981).
- [45] A. Schmitt, nucl-th/0405076.
- [46] M. Alford and K. Rajagopal, JHEP **06**, 031 (2002), hep-ph/0204001.
- [47] I. Shovkovy and M. Huang, Phys. Lett. **B564**, 205 (2003), hep-ph/0302142.
- [48] M. Huang and I. Shovkovy, Nucl. Phys. **A729**, 835 (2003), hep-ph/0307273.
- [49] M. Alford, C. Kouvaris, and K. Rajagopal, Phys. Rev. Lett. **92**, 222001 (2004), hep-ph/0311286.
- [50] M. Alford, C. Kouvaris, and K. Rajagopal, Phys. Rev. **D71**, 054009 (2005), hep-ph/0406137.
- [51] M. Alford, P. Jotwani, C. Kouvaris, J. Kundu, and K. Rajagopal, Phys. Rev. **D71**, 114011 (2005), astro-ph/0411560.
- [52] M. Huang and I. A. Shovkovy, Phys. Rev. **D70**, 051501 (2004), hep-ph/0407049.
- [53] R. Casalbuoni, R. Gatto, M. Mannarelli, G. Nardulli, and M. Ruggieri, Phys. Lett. **B605**, 362 (2005), hep-ph/0410401.
- [54] M. Alford and Q.-h. Wang, J. Phys. **G31**, 719 (2005), hep-ph/0501078.
- [55] K. Iida, T. Matsuura, M. Tachibana, and T. Hatsuda, Phys. Rev. Lett. **93**, 132001 (2004), hep-ph/0312363.
- [56] F. Neumann, M. Buballa, and M. Oertel, Nucl. Phys. **A714**, 481 (2003), hep-ph/0210078.
- [57] I. Shovkovy, M. Hanauske, and M. Huang, Phys. Rev. **D67**, 103004 (2003), hep-ph/0303027.
- [58] S. Reddy and G. Rupak, Phys. Rev. **C71**, 025201 (2005), nucl-th/0405054.

- [59] A. I. Larkin and Y. N. Ovchinnikov, Zh. Eksp. Teor. Fiz. **47**, 1136 (1964).
- [60] P. Fulde and R. A. Ferrell, Phys. Rev. **135**, A550 (1964).
- [61] M. G. Alford, J. A. Bowers, and K. Rajagopal, Phys. Rev. **D63**, 074016 (2001), [hep-ph/0008208](#).
- [62] P. F. Bedaque and T. Schäfer, Nucl. Phys. **A697**, 802 (2002), [hep-ph/0105150](#).
- [63] D. B. Kaplan and S. Reddy, Phys. Rev. D **65**, 054042 (2002).
- [64] A. W. Steiner, S. Reddy, and M. Prakash, Phys. Rev. **D66**, 094007 (2002), [hep-ph/0205201](#).
- [65] H. Abuki, M. Kitazawa, and T. Kunihiro, Phys. Lett. **B615**, 102 (2005), [hep-ph/0412382](#).
- [66] Y. Nambu and G. Jona-Lasinio, Phys. Rev. **122**, 345 (1961).
- [67] Y. Nambu and G. Jona-Lasinio, Phys. Rev. **124**, 246 (1961).
- [68] U. Vogl and W. Weise, Prog. Part. Nucl. Phys. **27**, 195 (1991).
- [69] S. P. Klevansky, Rev. Mod. Phys. **64**, 649 (1992).
- [70] P. Rehberg, S. P. Klevansky, and J. Hüfner, Phys. Rev. **C53**, 410 (1996), [hep-ph/9506436](#).
- [71] J. I. Kapusta, *Finite-temperature field theory* (Cambridge University Press, 1989).
- [72] W. M. Yao et al. (Particle Data Group), J. Phys. **G33**, 1 (2006).
- [73] P. Amore, M. C. Birse, J. A. McGovern, and N. R. Walet, Phys. Rev. **D65**, 074005 (2002), [hep-ph/0110267](#).
- [74] M. Asakawa and K. Yazaki, Nucl. Phys. **A504**, 668 (1989).
- [75] J. Berges and K. Rajagopal, Nucl. Phys. **B538**, 215 (1999), [hep-ph/9804233](#).
- [76] M. Buballa and M. Oertel, Nucl. Phys. **A703**, 770 (2002), [hep-ph/0109095](#).
- [77] K. Rajagopal and F. Wilczek, Phys. Rev. Lett. **86**, 3492 (2001), [hep-ph/0012039](#).
- [78] A. Burrows and J. M. Lattimer, Astrophys. J. **307**, 178 (1986).
- [79] M. Prakash et al., Phys. Rept. **280**, 1 (1997), [nucl-th/9603042](#).
- [80] D. Nickel, R. Alkofer, and J. Wambach, Phys. Rev. **D74**, 114015 (2006), [hep-ph/0609198](#).



- [81] R. Rapp, T. Schäfer, E. V. Shuryak, and M. Velkovsky, *Annals Phys.* **280**, 35 (2000), [hep-ph/9904353](#).
- [82] T. Schäfer, *Phys. Rev.* **D65**, 094033 (2002), [hep-ph/0201189](#).
- [83] R. Casalbuoni and R. Gatto, *Phys. Lett.* **B464**, 111 (1999), [hep-ph/9908227](#).
- [84] D. T. Son and M. A. Stephanov, *Phys. Rev.* **D61**, 074012 (2000), [hep-ph/9910491](#).
- [85] T. Schäfer, *Phys. Rev.* **D65**, 074006 (2002), [hep-ph/0109052](#).
- [86] M. Buballa and I. A. Shovkovy, *Phys. Rev.* **D72**, 097501 (2005), [hep-ph/0508197](#).
- [87] M. Rho, A. Wirzba, and I. Zahed, *Phys. Lett.* **B473**, 126 (2000), [hep-ph/9910550](#).
- [88] M. Rho, E. V. Shuryak, A. Wirzba, and I. Zahed, *Nucl. Phys.* **A676**, 273 (2000), [hep-ph/0001104](#).
- [89] H. Abuki and T. Kunihiro, *Nucl. Phys.* **A768**, 118 (2006), [hep-ph/0509172](#).
- [90] D. Nickel, J. Wambach, and R. Alkofer, *Phys. Rev.* **D73**, 114028 (2006), [hep-ph/0603163](#).
- [91] C. Manuel and M. H. G. Tytgat, *Phys. Lett.* **B479**, 190 (2000), [hep-ph/0001095](#).
- [92] N. Yamamoto, M. Tachibana, T. Hatsuda, and G. Baym, *Phys. Rev.* **D76**, 074001 (2007), [0704.2654](#).
- [93] J. D. Bjorken and S. D. Drell, *Relativistische Quantenmechanik* (BI Wissenschaftsverlag, 1992).
- [94] D. Blaschke, S. Fredriksson, H. Grigorian, A. M. Oztas, and F. Sandin, *Phys. Rev.* **D72**, 065020 (2005), [hep-ph/0503194](#).

## *Bibliography*

---

# Danksagung

Zum Gelingen dieser Arbeit habe viele Personen beigetragen. Dafür möchte ich mich an dieser Stelle herzlich bedanken.

An erster Stelle danke ich Prof. J. Wambach für die Gelegenheit diese Arbeit anzufertigen und für die Möglichkeit mehrere Workshops und Sommerschulen zu besuchen.

Meinem Betreuer Dr. Michael Buballa danke ich für die Zusammenarbeit in den zurückliegenden Jahren, für sein Interesse an meiner Arbeit und seine Unterstützung während dieser Zeit.

Allen Mitgliedern der Theoriegruppen des Instituts für Kernphysik danke ich für die sehr angenehme Arbeitsatmosphäre und zahlreiche hilfreiche Gespräche. Ein besonderer Dank geht dabei an die „Kaffeerunde“ in Zimmer 411: Heiko Hergert, Markus Hild, Felix Schmitt und Mathias Wagner, denen ich außerdem ganz herzlich für das Korrekturlesen dieser Arbeit danke. Dieser Dank geht ebenfalls an Thomas Roth.

Meinen Zimmerkollegen Mathias Wagner und Markus Hild danke ich darüber hinaus für die tolle Atmosphäre in unserem Zimmer und die Unterstützung bei allen Computerbelangen. Schließlich danke ich Mathias Wagner noch für die Unterstützung und Freundschaft in den neun Jahre, die wir nun zusammen studiert und gearbeitet haben.

Meinen Eltern und meinem Bruder danke ich für die andauernde Unterstützung während meines gesamten Studiums. Ganz besonders dankbar bin ich meiner Mutter auch dafür, dass sie in den letzten Wochen und Monaten recht häufig auf ihre Enkelin aufgepasst hat und mir so erst die Fertigstellung dieser Arbeit ermöglicht hat.

Meinem Mann danke ich für sein Verständnis besonders während der Schlussphase dieser Arbeit. Zu guter Letzt danke ich meiner Tochter Lena dafür, dass sie ein so liebes Kind ist und mich in jeder Situation zum Lachen bringt.



# Lebenslauf

**Name:** Verena Kleinhaus geb. Werth  
**Geburtsdatum:** 20. April 1980  
**Geburtsort:** Rüsselsheim  
**Staatsangehörigkeit:** deutsch  
**Familienstand:** verheiratet, 1 Kind

## Bildungsweg

08/1986 - 07/1990 Besuch der Grundschule Nauheim  
08/1990 - 06/1999 Besuch der Immanuel-Kant-Schule, Rüsselsheim  
(Gymnasium)  
06/1999 Abitur, Gesamtnote: 1.0  
  
10/1999 - 11/2004 Studium der Physik an der TU Darmstadt  
10/2001 Vordiplom Physik, Gesamtnote: gut  
09/2003 - 09/2004 Anfertigung der Diplomarbeit „*Farbsupraleitung in Neutronen- und Protoneutronensternen*“  
11/2004 Diplom, Gesamtnote: sehr gut  
  
seit 12/2004 Promotionsstudium an der TU Darmstadt und Anfertigung der Dissertation  
seit 12/2004 Wissenschaftliche Mitarbeiterin am Institut für Kernphysik

